AD-A043 368 NAVAL RESEARCH LAB WASHINGTON D C F/G 20/11
ORGANIZATIONAL SCHEME FOR CORROSION-FATIGUE CRACK PROPAGATION D--ETC(U)
JUL 77 J M KRAFFT, W H CULLEN

UNCLASSIFIED NRL-MR-3505 NL

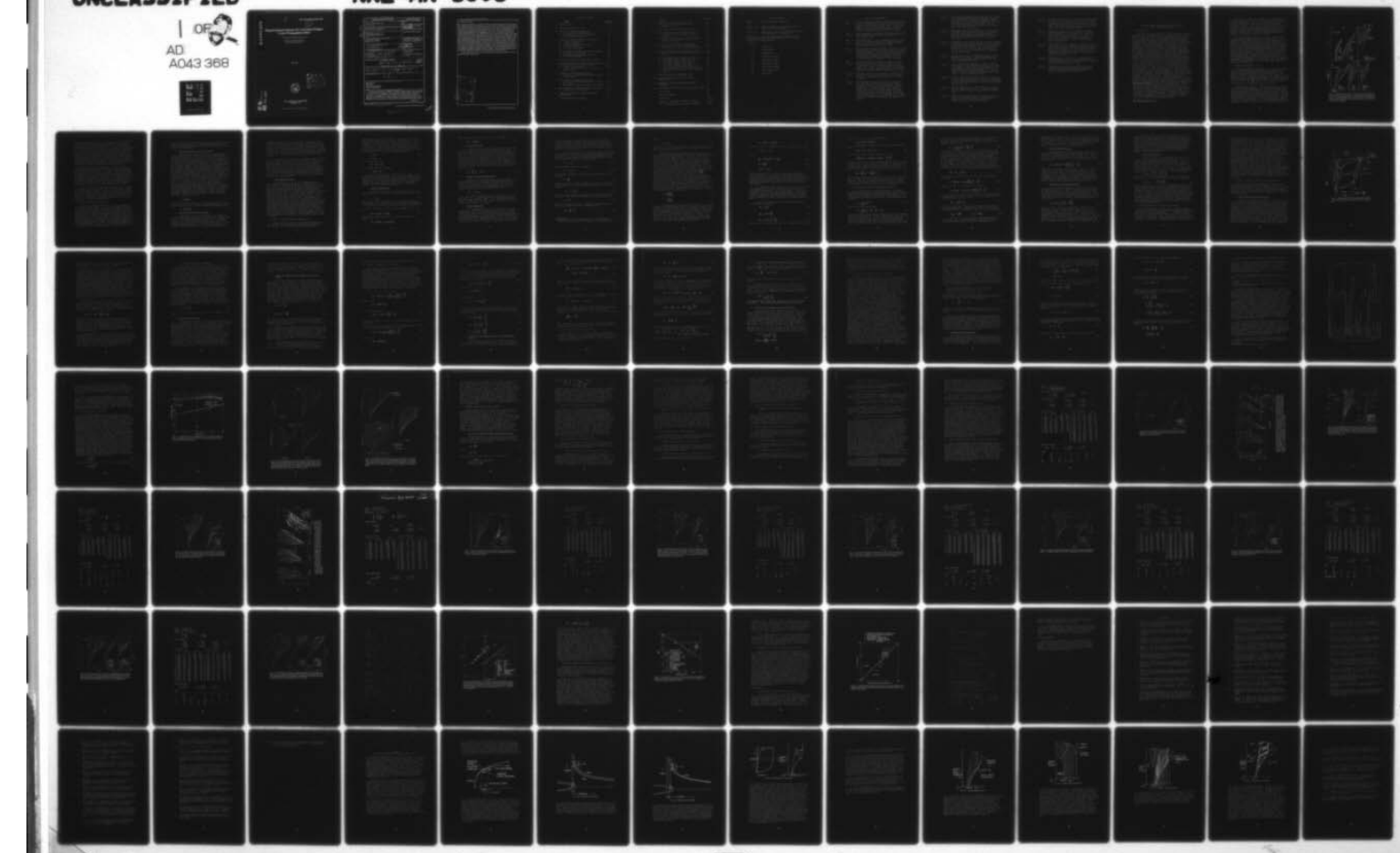

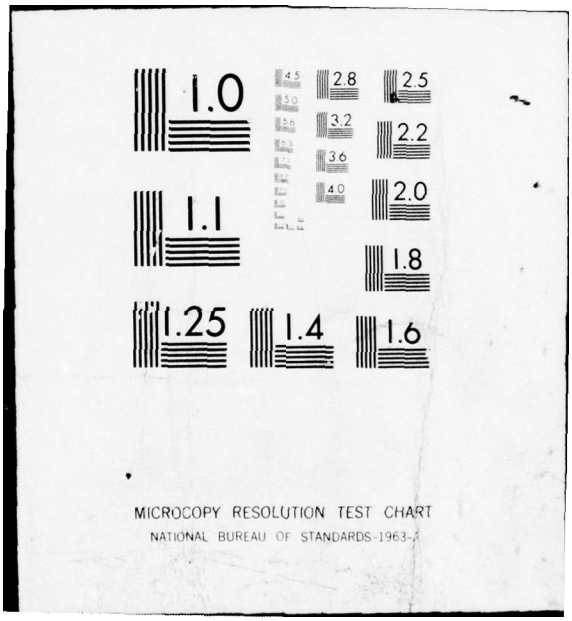
1.0
1.1
1.25
1.4
1.6
1.8
2.0
2.2
2.5
2.8
3.2
3.6
4.0
4.5
5.0
5.6
6.3
MICROCOPY RESOLUTION TEST CHART
NATIONAL BUREAU OF STANDARDS-1963-A

AD A043368

NRL Memorandum Report 3505

Organizational Scheme for Corrosion-Fatigue Crack Propagation Data

J. M. KRAFFT and W. H. CULLEN, JR.

Mechanics of Materials Branch
Ocean Technology Division

July 1977

DDC
RECEIVED
AUG 29 1977
A

AD No.
DDC FILE COPY

NAVAL RESEARCH LABORATORY
Washington, D.C.

Approved for public release; distribution unlimited.

SECURITY CLASSIFICATION OF THIS PAGE (When Data Entered)

REPORT DOCUMENTATION PAGE

READ INSTRUCTIONS BEFORE COMPLETING FORM

1. REPORT NUMBER: NRL Memorandum Report 3505	2. GOVT ACCESSION NO.
3. RECIPIENT'S CATALOG NUMBER	
4. TITLE (and Subtitle): ORGANIZATIONAL SCHEME FOR CORROSION-FATIGUE CRACK PROPAGATION DATA	5. TYPE OF REPORT & PERIOD COVERED: Interim report on a continuing NRL problem
	6. PERFORMING ORG. REPORT NUMBER
7. AUTHOR(s): J.M. Krafft and W.H. Cullen, Jr.	8. CONTRACT OR GRANT NUMBER(s)
9. PERFORMING ORGANIZATION NAME AND ADDRESS: Naval Research Laboratory, Washington, D.C. 20375	10. PROGRAM ELEMENT, PROJECT, TASK AREA & WORK UNIT NUMBERS: NRL Problems F01-03 and F01-24, RR-023-03-45 WR022-01-001
11. CONTROLLING OFFICE NAME AND ADDRESS	12. REPORT DATE: July 1977
	13. NUMBER OF PAGES: 99
14. MONITORING AGENCY NAME & ADDRESS (if different from Controlling Office)	15. SECURITY CLASS. (of this report): UNCLASSIFIED
	15a. DECLASSIFICATION/DOWNGRADING SCHEDULE

16. DISTRIBUTION STATEMENT (of this Report)

Approved for public release; distribution unlimited.

17. DISTRIBUTION STATEMENT (of the abstract entered in Block 20, if different from Report)

18. SUPPLEMENTARY NOTES

19. KEY WORDS (Continue on reverse side if necessary and identify by block number)

Fracture model
Plastic flow
Corrosion fatigue cracking
Fatigue crack propagation

20. ABSTRACT (Continue on reverse side if necessary and identify by block number)

A model, proposed earlier, is modified in an attempt to explain a number of curious behaviors of corrosion-fatigue crack propagation (CFCP). The behaviors include effects of load ratio R in air and salt water vs. vacuum, and effects of loading frequency at fixed R in these environments. Assumptions of the modelling are reviewed in detail in view of earlier objections to them. The ingredients of CFCP per this model: Poisson contraction, strain hardening, ligament surface attack/annihilation, and stress relaxation are developed and related to conditions of the crack-tip locale. → next page

(Continues)

251950

20. Abstract (Continued)

In the modelling, a parameter G, for growth rate factor, is developed solely as a function of the form of the ordinary or of the cyclic stress-strain curve. Previous work had developed a G_1 for the ordinary curve, to be associated with the surface attack effect as in stress-corrosion cracking, and one G_2 for the cyclic curve, to be associated with the stress relaxation effect as in fatigue crack propagation (FCP). A hybrid $G_{2/1}$ is developed, combining attributes of both, which seems to successfully describe the corrosion induced augmentation of G_2. Parametric curves of $G_{2/1}$ correspond well with stage II frequency-dependent growth in CFCP. However, alone they do not explain the frequency-wise stage II threshold shift nor the frequency-independent air-environment FCP rate. It is found that these trends can be represented by loci of constant plastic strain rate, due to crack loading and propagation, relative to the surface annihilation rate. Such loci are determined by comparing "G maps" with strain rate maps, using parametric curves of equal geometric-series spacing. Maps of this sort are used to analyze about a dozen cases of CFCP including two titanium alloys, one aluminum and three steels, with one of the steels of four different tempers. Stress-strain curves of the low strength steels are processed to remove the Lüder band effect to facilitate the modelling. The scheme for data organization involves a representation of indexes of the two kinds of parametric curves fitting the data, and the process zone size implied by the fitting. Comparison of estimated process zone size with literature data of microstructural and fractographic size measurements is encouraging. Model predication of load ratio effects on the fatigue crack growth threshold is in good correspondence with literature data.

For the reader who may wish to defer a detailed study of this report, an Appendix provides an illustrated summary of major points.

TABLE OF CONTENTS

LIST OF TABLES

Tabulations of Chemical and Mechanical Properties and Conditions of CFCP Tests for Each Alloy Are Inserted Adjacent the Figure Display:

LIST OF ILLUSTRATIONS

ORGANIZATIONAL SCHEME FOR CORROSION-FATIGUE CRACK PROPAGATION DATA

I. INTRODUCTION

This paper continues authors' pursuit of physical models by which various manifestations of subcritical crack propagation can be predicted from ordinary and cyclic stress-strain properties of the cracked material. The materials for which this now appears feasible are generally high to medium-strength wrought alloys, whose fracture instability involves ductile tearing, albeit localized, as distinct from cleavage. A central assumption of this modelling is the necessity and likely sufficiency of condition for tensile instability in the crack locale for fracture instability. The original proposal (1964) [1] stemmed from experimental correlations of the strain for simple tensile instability, as influenced by temperature and strain rate, with the plane-strain fracture toughness, K_{Ic}, as similarly influenced. Some years later [2] it was noticed that crack velocity under conditions for stress-corrosion cracking (SCC) could be related to the shape of the entire stress-strain curve. With strain near the crack tip assumed proportional to the stress intensity factor, this corresponds to an applied K less than K_{Ic}, i.e., the regime of subcritical crack propagation. Here the source of tensile instability was viewed as a surface annihilation - or corrosion-rate acting upon critical crack-tip ligaments. Since corrosion is a stable process, so correspondingly is the crack growth induced to compensate for the eroding sectional area of the ligament. In a sense, then, it became unnecessary to specify tensile instability as a failure condition. Crack growth could be perceived as a mechanism, other than rising external load, by which the load upon crack tip elements is maintained constant. Later, at the suggestion of Landes and Wei [3], the stress relaxation during the dwell time of a fatigue cycle was recognized as another source of load diminution. When related to cyclic stress-strain properties, this provided a one-parameter fit of a number of sets of fatigue crack propagation (FCP) data [4]. This was followed by two NRL studies [5,6], attempting to combine influences of ligament corrosion, as a surface effect, with its stress relaxation, as a volume effect, to explain corrosion fatigue crack propagation (CFCP).

Note: Manuscript submitted June 13, 1977.

Only partial success was enjoyed from these endeavors. One difficulty, carried over from the stress-corrosion-cracking model, was a failure to predict the correct trend in the ΔK-threshold. Whereas the model related the threshold directly to the yield strength level, the data indicates a strong inverse trend, except at very high strength levels. Another deficiency was apparent in CFCP. Here the K-threshold of rapid, environmentally-induced Stage II growth tends to increase with increased cycle duration. The model predicted no change.

These shortcomings, as well as concern with the simplistic analysis and assumptions, led to its less than enthusiastic acceptance by the technical community. In an attempt to remedy these shortcomings, this paper reports results of a careful examination of some dozen sets of corrosion fatigue crack propagation data. These exemplify each of the currently known anomolous behaviors of CFCP. In each case, we have performed mechanical stress-strain tests of the actual, or essentially identical, materials. Between these end points, fracture vs flow data sets, we have permuted what combinations of model parameters it seemed permissible to vary. The permutations involved calculation and graphing, made possible by digital computer and graphics programming. It is thought that some improvements in modelling have been developed which are worth reporting at this time.

2. ANOMALOUS BEHAVIORS IN CFCP

It may be helpful at the outset to list each characteristic of CFCP which has been addressed, citing here the data source and material taken as illustrative. Such initial summary of behaviors follows the practice of Speidel [7] and of Dawson and Pelloux [8]. Figure 1 depicts those which are treated in this paper. We follow the Paris convention [9] of displaying FCP data as a full logarithmic plot of the FCP rate $\frac{\Delta a}{\Delta N} = \dot{a}_N$, vs the opening mode stress intensity factor range ΔK_I, simply called ΔK.

Consider first effects of the load ratio R on CFCP at constant loading frequency. The base of reference, Figure 1a, is fatigue crack propagation in vacuum, for which we employ the results of Irving and Beevers [10] on a martensitic Ti-6Al-4V alloy. Generally the FCP rate is lower in vacuum than in air, particularly at low ΔK levels. Despite the indication of an environmental effect of air, the FCP rate in air is insensitive to loading frequency, atypical of that in liquid corrodents. Irving and Beevers find the threshold for onset of FCP, ΔK_{TH}, relatively insensitive to

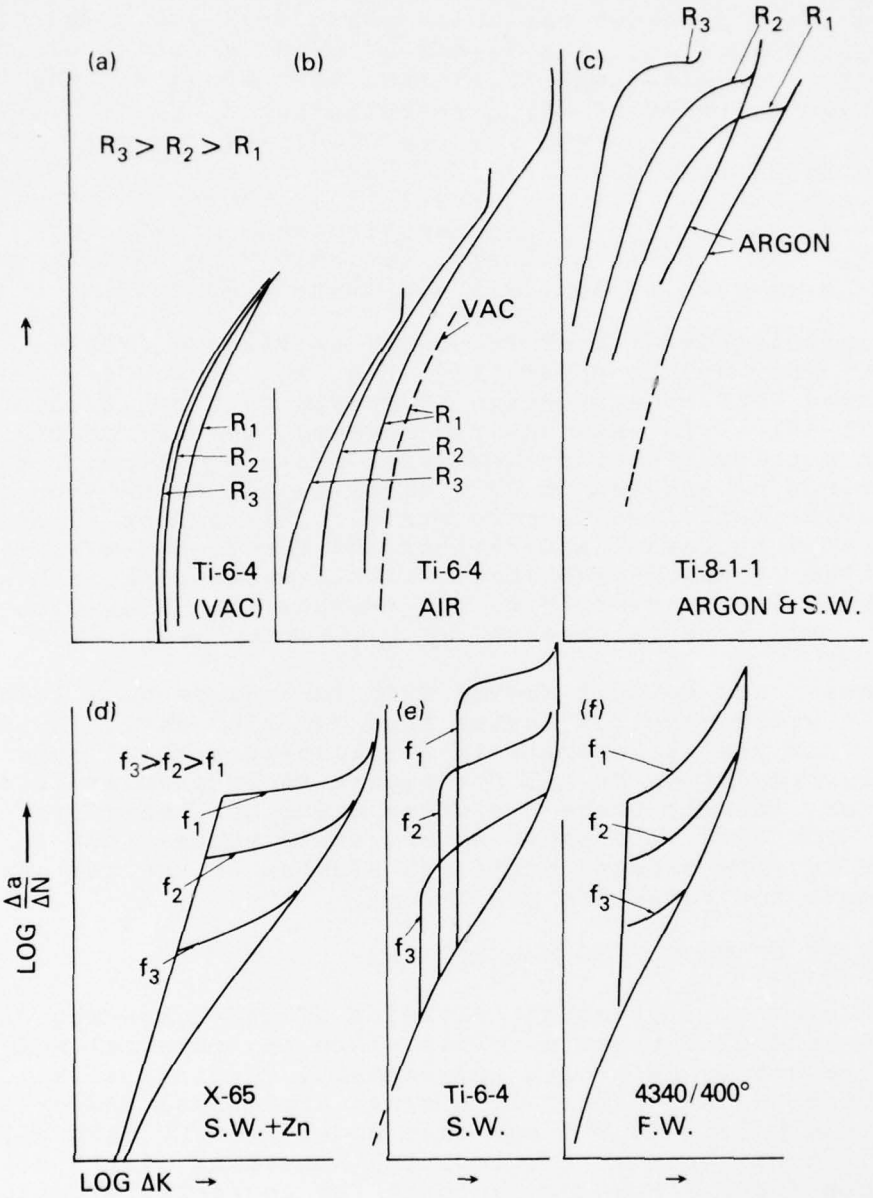

Fig. 1 — Curious effects in CFCP: of load ratio R, (a) little effect in vacuum but (b) increased growth rate and decreased ΔK-threshold in air, and (c) increased stage II level in salt water; and of loading frequency f, (d) continuously decreasing stage II onset, (e) stepwise decrease, and (f) no change.

load ratio R above about 0.3. In one case of a low alloy Q&T steel Cooke, Irving, Booth and Beevers [11] observe practically nil sensitivity for all R's. In normal air environment, however, $\Delta K_{TH}(R)$ drops off with (increasing) R to a limit of about one-third that for R = 0. The example of this, Figure 1b, is a Ti-6Al-4V used by Fitzgerald and Wei [12]. In mid-range ΔK levels, the FCP rates tend to merge again, prior to ΔK_{max} reaching the K_c instability limit. This is observed for the Ti-6Al-4V, as well as for A533 B steel (not used here) of Paris et al [13]. However, in Ti-8Al-1Mo-1V, Fig. 1c, Bucci [14] observes a strong leftward translation of argon-environment growth curves with increased R. Correspondingly, his salt water growth curve shifts even more to the left and upwards as well.

Regarding effects of frequency at fixed R, Pettit, Krupp, Ryder and Hoeppner [15], Fig. 1e, show a typically increased CFCP rate in Stage II growth with cycle duration on a Ti-6Al-4V in salt water. However, the ΔK for Stage II growth acceleration increases with cycle duration, leading to curious crossovers in CFCP rates in the transition to the normal (air) growth rate curve. This effect is clearly documented by Dawson and Pelloux [8] for Ti-6Al-6V-2Sn. In a high strength 4340 steel, little sweep-back in Stage II threshold is observed, Fig. 1d, whereas in a line-pipe steel, even more is observed by Vosikovsky [40], Fig. 1f.

Dawson and Pelloux showed CFCP for square wave loading in salt water about 3X faster than for sine wave. However Vosikovsky has one example in X65 line-pipe steel showing a CFCP retardation by 1/3 for square vs triangular loading patterns. Surely there are other anomolous behaviors of CFCP. But even with those noted, small wonder that confusion is rife amongst engineers seeking to use the available data for safe-life prediction.

3. BRIEF OF MODELLING ASSUMPTIONS

In view of aforenoted criticism of model assumptions, a word here on rationale. This, like any physical model for fracture in an active environment, requires a failure criterion in the context of a crack tip stress and/or strain field analysis. To fit any such model to CFCP data will involve a size parameter, implying something of the alloy microstructure. Further, account for corrosion effects will involve some sort of surface attack, implying aspects of corrosion chemistry. To combine all of these elements into single, workable fracture model requires major simplifications/approximations of each. Such simplifications often prove unacceptable to experts in the field involved, leading to rejection of the entire scheme. We are not astute

enough to avoid this dilemma, but ask that suspected assumptions be granted trial as working hypotheses, whose plausability would be enhanced by success of data correlations which employ them.

A. Failure Criterion/Plasticity Model

Regarding the failure criterion, we hypothesize, as Orowan years ago [16], that local tensile instability, generally conceded to be a necessary condition in the path to rupture of a tensile specimen, is also a very-nearly sufficient one for the crack tip locale. How nearly depends of course, on the effective compliance of links connecting the critical element to the interior of the cracked body. The contention that reaching the maximum load point is sufficient was based on the experimental evidence of direct correlation of the plane strain fracture toughness K_{Ic} with the plastic-flow strain for maximum load, as estimated from the strain hardening exponent n. Both K_{Ic} and n were observed to respond similarly to variations in temperature and straining rate. A size parameter is derived from a calculation of the distance from the mathematical crack tip origin at which the tensile y-strain level recedes to the value of n. With K_{Ic} and n directly proportional, a y-strain directly proportional to K (and independent of yield strength and strain hardening characteristics of the material), was seen as indicating a constant size parameter. Since microstructural size parameters should be unaffected by reduced temperature and high strain rate, the test-variables employed, this (constancy) seemed a desirable attribute. Hence, the simple elastic field analogue for crack tip strain was adopted

$$\epsilon_y = K_I/\sqrt{2\pi r}\ E \tag{1}$$

where ϵ_y is strain normal to the crack plane at distance r forward of the crack tip, and E is Young's modulus. Since $\epsilon_y = n$ when $K_I = K_{Ic}$, the size parameter was calculated as

$$d_T = K_{Ic}^2/2\pi E^2 n^2 \tag{2}$$

B. Microstructural Size Parameter

Significance of the size parameter d_T, called a process zone size, could not be assessed from evidence then at hand. The strain hardening exponent n is not always equal to the strain for tensile instability. Crack tip triaxiality, as discussed by Williams and Turner [17], can require a greater strain. More too would be needed if failure required attainment of a strain intermediate that

for maximum load and that for rupture. Larger critical strains, at given K_{Ic}, are found only closer in toward the crack tip, hence smaller d_T. Conversely, a stronger than inverse-half-power strain singularity, indicated by several analyses [18, 19, 20], would provide, for given K_{Ic}, strains reaching the increased "failure" strain at greater distances from the crack tip. Hence a judicious combination of these assumptions could provide almost any process-zone size needed.

As it turns out, the size needed well may be simply that indicated by Equation (2), as a number of investigations, to be discussed in Section 22, have shown fractographic dimple size in various alloys and/or largest-inclusion spacing in steels to correlate reasonably well with the d_T of Equation 2. Further, careful experimental work of Liu and his students [21] has invariably indicated the inverse-half-power strain singularity. We conclude from this that the simple elastic-analogue strain singularity of Eq. (1) is the better choice for these problems, which is thus employed here.

C. Environmental Attack

Finally in the list of model ingredients, the environmental influence parameter of surface attack. We would describe this broadly as any environmental activity about the crack tip d_T-element which has the effect of gradually annihilating the load-bearing capability of material at its surface. The most obvious means of removing material was thought to be dissolution, which was then proposed in Ref. [2]. Corrosion experts object to this degree of specificity, pointing out that other processes are known to influence SCC and CFCP. Thus making the cracked specimen either anodic or cathodic with respect to its neutral condition is known to accelerate the SCC, hence the CFCP rate. Added stress from pressurized voids [22], eased dislocation glide by matrix solute interaction [23], micro-hydride swelling, flaking [24] are all possible mechanisms. Unfortunately this model cannot discriminate among annihilation mechanisms. However, it does allow quantification of the effect of such mechanisms in terms of the effective total depth of surface annihilation and, if normalized with respect to cycle duration, of its rate of attack.

4. SOURCES OF LIMITED TENSILE INSTABILITY

Assuming that the condition of constant-load maintenance could closely approach a sufficient condition for crack growth, the following, previously published,

derivation is repeated here [25]. The analysis pertains to any unrestrained tensile specimen, such as those of size d_T thought to regulate the rate of crack propagation. The question is: what amount of straining; hence strain hardening; hence, in the context of the crack tip strain field at constant K, crack extension, is required to maintain a constant load, hence stability, in a given ligament? Such load P supported over area A defines a stress

$$\bar{\sigma} = P/A \tag{3}$$

or

$$P = \bar{\sigma}A$$

Differentiating then

$$dP = \bar{\sigma}\, dA + A\, d\bar{\sigma} \tag{4}$$

At constant load dP = 0 whence

$$-\bar{\sigma}\, dA = A\, d\bar{\sigma} \tag{5}$$

The total differentials of area A and of stress $\bar{\sigma}$ can be separated into constituent partials. The familiar ones are Poisson contraction and strain hardening respectively, ingredients of the ordinary mechanical tensile instability phenomenon. Less familiar partials are the d_T-ligament surface corrosion/annihilation, and stress relaxation. Consider now each influence in detail.

A. Poisson Contraction

Lateral contraction, hence areal diminution, due to elongation of a ligament is characterized by the Poisson ratio

$$\nu = -\bar{\epsilon}_d/\bar{\epsilon}_\ell \tag{6}$$

where $\bar{\epsilon}_d$ is diametral strain, $\bar{\epsilon}_\ell$ is longitudinal strain of the ligament. For simplicity, the subscript ℓ, designating a longitudinal property, is deleted in further development.

For a ligament of radius r_T, (or diameter d_T) $A = \pi r_T^2$ or,

$$dA = 2\pi r_T\, dr_T = 2\pi r_T^2\, d\bar{\epsilon}_d \tag{7}$$

Hence, the area partial due to Poisson contraction is defined as

$$\partial A_\nu = 2\pi r_T^2\, d\bar{\epsilon}_d = -\nu\pi\, d_T^2\, d\bar{\epsilon}/2 \tag{8}$$

which for plastic flow $\bar{\epsilon}_p$, where $\nu = 0.5$ becomes

$$\partial A_\nu = -\frac{\pi}{2} d_T^2 \, d\bar{\epsilon}_p \tag{9}$$

B. Strain Hardening

It appears from these modelling attempts that only the plastic part of the measured total (elastic plus plastic) strain hardening rate is effective as stabilizing the three "inducers" of crack growth: the surface attack rate, the stress relaxation, and the Poisson contraction. In the case of stress relaxation, the reason for this is clearly the plastic (only) strain rate sensitivity of the flow stress, which is equated to the stress relaxation. For the other inducers, apparently only the permanent, non-reversible portion of strain hardening has a stabilization attribute. Hence for the plastic strain hardening, the stress partial is

$$\partial \bar{\sigma}_\theta = \frac{d\bar{\sigma}}{d\bar{\epsilon}_p} \, d\bar{\epsilon}_p = \bar{\theta}_p \, d\bar{\epsilon}_p \tag{10}$$

C. Ligament Surface Annihilation

Effects of corrosion rate on tensile instability are usually negligible for ordinary macro-specimen sizes. However for micro-size ligaments at the crack tip, the effect can be substantial. From Equation (7) above let $dr_T = -V_S dt$, where V_S is the annihilation rate at the d_T ligament surface, whence this partial of A is

$$\partial A_s = -\pi \, d_T \, V_s \, dt \tag{11}$$

The surface annihilation rate V_S need not be constant, but, as in ordinary corrosion, typically diminishes with time, as indicated later. It is convenient to designate a symbol for the total surface intrusion during the entire cycle period: $\Delta r_T \equiv V_S \Delta t$.

D. Stress Relaxation

The remaining partial of $\bar{\sigma}$ is that due to stress relaxation. The effect in structural alloys at ordinary temperatures may be closely associated with the plastic-flow stress sensitivity to rate of plastic (only)deformation. For present purposes it is important to have a realistic, yet hopefully simple characterization of this effect, particularly of how it is related to the position in the stress-strain cycle in which it occurs. Since there is a consid-

erable literature on the strain rate sensitivity which could be brought to bear on this question, the basis of conversion should be noted. Derivations in the literature provided by Guiu and Pratt [26], and later by Hart [27], are abstracted here for convenience of the reader, using symbols of Guiu and Pratt.

In a tensile test, the crosshead speed $\dot{y}$ is matched by the elastic plus plastic lengthwise deformation rate of the specimen $\dot{\ell}_e + \dot{\ell}_p$ plus the elastic deformation of the machine $\dot{z}$, particularly of highly stressed elements of the load train such as the load cell and grips

$$\dot{y} = \dot{\ell}_p + \dot{\ell}_e + \dot{z} \tag{12}$$

With crosshead arrest, $\dot{y} = 0$ whence

$$\dot{\ell}_p = -(\dot{\ell}_e + \dot{z}) \tag{13}$$

The machine deformation is inversely proportional to its stiffness

$$S = \frac{dP}{dz} \tag{14}$$

assumed constant for small changes in load P. Converting length changes $\dot{\ell}$ to (engineering) strain rates $\dot{\epsilon}$, Eq. (13) becomes

$$\dot{\epsilon}_p = -\dot{\epsilon}_z - \frac{a_0}{\ell_0 S}\,\dot{\sigma} \tag{15}$$

where ℓ_o and a_o are initial length and section area of the specimen. The elastic deformation rate can be expressed

$$\dot{\epsilon}_e = \dot{\sigma}/E \tag{16}$$

where E is Young's modulus. Combining the specimen plus machine compliance into total compliance C_T*

$$C_T = \frac{a_0}{\ell_0 S} + \frac{1}{E} \tag{17}$$

---

* Designation here of compliance by C, as used by Hart, rather than by M of Guiu and Pratt, our usual practice.

whence

$$\dot{\epsilon}_p = -C_T \dot{\sigma} \tag{18}$$

Equation (18) says that a plot of σ vs $\dot{\sigma}$, is equivalent to a plot of σ vs $\dot{\epsilon}_p$. Hence the stress relaxation test provides direct measure of $\sigma(\dot{\epsilon})$.

Whether determined by stress relaxation vs time or by stress vs strain rate measurements, the character of this behavior is important here. Guiu and Pratt [26] assert that the absolute sensitivity of flow stress to relative (log) strain rate, $\frac{d\sigma}{d\log\dot{\epsilon}}$, is constant over widely ranging time/strain rates. J. D. Campbell [28] normally displays his strain rate and strain rate history effects in this manner. This is consistent with the observation [29] that the absolute sensitivity in ferrous alloys tends to be constant for varied strength levels. However, when one looks at a given alloy over a range of flow stress levels produced by straining, the relative sensitivity $\frac{d\log\sigma}{d\log\dot{\epsilon}}$ appears more nearly constant. Thus plots of true flow stress vs plastic strain rate for parametric variation of strain level tend to be more nearly straight and parallel to each other in full logarithmic display, than semilogarithmic. Hart's work supports the latter contention. It is commonly used in superplasticity calculations where very large deformations must be estimated. Our own observations support it. Thus, we have elected the latter option in this model development, using the superplasticity literature convention of designating the exponent of sensitivity as the constant m,

$$m = \frac{d \log(\bar{\sigma})}{d \log(\dot{\bar{\epsilon}}_p)} \tag{19}$$

or

$$m = \frac{d\sigma/\sigma}{d\dot{\bar{\epsilon}}_p/\dot{\bar{\epsilon}}_p} \tag{20}$$

If indeed the strain rate sensitivity is of the kind characterized by Equation (20), it is possible to measure it from a log plot of stress vs the relaxation time. Assume here, as implicit in Guiu and Pratt, and Hart, a path- or history-independent mechanical equation of state. Consider then a path in stress/plastic-strain-rate "space" to a fixed plastic strain at two different but constant strain rates $\dot{\bar{\epsilon}}_1 < \dot{\bar{\epsilon}}_2 = \dot{\bar{\epsilon}}_1 + d\dot{\bar{\epsilon}}$ in correspondingly, two different times $t_1 > t_2$. The stress differential between these end points is given by rearrangement of Eq. (20).

$$d\bar{\sigma} = m\bar{\sigma}\,\frac{d\dot{\bar{\epsilon}}}{\dot{\bar{\epsilon}}} = m\sigma\,\frac{\dot{\bar{\epsilon}}_2 - \dot{\bar{\epsilon}}_1}{\dot{\bar{\epsilon}}_1} \tag{21}$$

However, since the terminal (plastic) strain $\bar{\epsilon}$ is the same

$$\dot{\bar{\epsilon}}_2 = \frac{\bar{\epsilon}}{t_2}\,;\quad \dot{\bar{\epsilon}}_1 = \frac{\bar{\epsilon}}{t_1} \tag{22}$$

whence

$$\frac{d\bar{\sigma}}{\bar{\sigma}} = m\,\frac{\bar{\epsilon}/t_2 - \bar{\epsilon}/t_1}{\bar{\epsilon}/t_1} = -m\,\frac{dt}{t_2} \tag{23}$$

$$d\bar{\sigma} = \frac{m\bar{\sigma}\,dt}{t_2} \tag{24}$$

$$\ell n\,(\bar{\sigma}) = -m\,\ell n\,(t) \tag{25}$$

Thus the slope of the log plot, noted above, provides a direct measure of (-)m. This is much more convenient and experimentally more accurate than measuring and plotting the slope of the $\bar{\sigma}$ vs time data plot. We find good agreement between the two methods of analysing stress relaxation data, and where available, with direct strain rate sensitivity measurements.

It should be noted that the above derivations assume that relaxation of plastic strain as well as the strain hardening associated with it are negligible; however, corrections for both effects are simple enough. The strain hardening correction is handled graphically in our experimental procedure by projecting back to the elastic line with an appropriate slope reflecting the strain hardening rate.

This result permits the fourth stress partial to be designated as simply

$$\partial\bar{\sigma}_m = m\bar{\sigma}\,\frac{dt}{t} \tag{26}$$

$$\Delta\bar{\sigma}_m \cong m\bar{\sigma}\,\ell n\left(\frac{\Delta t}{t}\right) \tag{27}$$

$$\Delta\bar{\sigma}_m \cong -m\bar{\sigma}\,\ell n\left(1 + \frac{t_H}{t_L}\right) \tag{28}$$

where t_H/t_L is the ratio of the hold or dwell time t_H to the

loading time t_L of the loading waveform.

E. All Sources Together

Combining all partials into the "load-maintenance" Equation (5) gives

$$-\bar{\sigma}(\partial A_p + \partial A_s) = A(\partial \bar{\sigma}_\theta + \partial \bar{\sigma}_m) \tag{29}$$

Inserting the above defined expressions gives

$$-\bar{\sigma}\left(\frac{\pi}{8} r_T^2 \, d\bar{\epsilon}_p + \pi \, d_T V_s \, dt\right) = A\left(\bar{\theta}_p \, d\bar{\epsilon}_p - m\bar{\sigma} \, \frac{dt}{t}\right) \tag{30}$$

We substitute πr_T^2 for the specimen/ligament area A, assumed circular. It is also useful to rearrange to separate the "stabilizing" strain differential required to maintain the constant load condition, since this will be traded for crack growth with the crack tip plasticity model. With this

$$d\bar{\epsilon}_p = \left(\frac{4V_s}{d_T} \, dt + m \, \frac{dt}{t}\right)\left(\frac{\bar{\theta}_p}{\bar{\sigma}} - 1\right)^{-1} \tag{31}$$

This equation, while developed for the case of a tiny ligament of radius r_T, is applicable to any tensile specimen, wherever subjected to tension strain, corrosion, strain hardening, and stress relaxation. It assumes no attributes of the crack tip locale. But this is now required.

5. CRACK-GROWTH VS STABILIZING-STRAIN TRADEOFF

It is necessary now to ask how strain is applied to microstructural tensile elements encroached by an advancing crack which is periodically unloaded, then reloaded. For reasons noted earlier, we employ the simple analogue of the linear elastic crack-tip stress field. Repeating Equation (1) here

$$\epsilon_y = \frac{1}{\sqrt{2\pi} \, E} K_I r^{-1/2} \tag{1}$$

which differentiated becomes

$$d\epsilon = \frac{1}{\sqrt{2\pi} \, E}\left(r^{-1/2} \, dK - \frac{K}{2} r^{-3/2} \, dr\right) \tag{32}$$

where r is the distance directly ahead of the crack measured from the crack tip. The strain differential varies with the position of sampling r. In this model we calculate the value of $d\epsilon$ at the fixed point $r = d_T$, and assume that strain is constant from this point back to the actual crack tip. The effect on the local strain of moving out from d_T

a distance dr is taken to be equivalent to holding a point fast in specimen coordinates and allowing the crack to advance a distance -da up to it, whence dr = -da. With this, Eq. (32) becomes

$$d\epsilon = \frac{1}{\sqrt{2\pi\, d_T}E}\left(dK_L + \frac{K_G}{2\, d_T}\, da\right) \tag{33}$$

The second K in Equation (33) carries a suffix G to denote its function as a gradient factor. The other K term, dK_L, is associated with rising load application. It is needed later in connection with a strain-rate field mapping. However for corrosion fatigue growth, it may be neglected, as the growth event is executed during the load dwell, while K_L is constant. The variable K_G is proportional to the gradient $\frac{d\epsilon}{dr}$ of the strain field at the point d_T, of which a special provision pertains under conditions of cyclic loading, as discussed later. We retain these distinctions in reverting Eq. (33) to K-proportional strains via Eq. (31).

$$d\bar{\epsilon}_p = d\epsilon_L + \frac{\epsilon_G}{2\, d_T}\, da \tag{34}$$

Eliminating $d\bar{\epsilon}_p$ between Eq. (34) and (31), neglecting $d\epsilon_L$ yields

$$da = \left[8V_s\, d_T + 2m\, d_T\, \frac{dt}{t}\right]\left[\epsilon_G\left(\frac{\bar{\theta}_p}{\bar{\sigma}} - 1\right)\right]^{-1} \tag{35}$$

Expressing (35) in incremental form yields

$$\Delta a = \left[8V_s\Delta t + 2m\, d_T\, \ell n\left(1 + \frac{t_{Hi}}{t_L}\right)\right]\left[\epsilon_G\left(\frac{\bar{\theta}_p}{\bar{\sigma}} - 1\right)\right]^{-1} \tag{36}$$

As noted earlier, crack propagation per cycle $\Delta a(=\Delta a/\Delta N)$ is displayed vs the stress intensity factor excursion, which in this model, from Eq. (1) is

$$\Delta K = \sqrt{2\pi\, d_T}\; E\Delta\epsilon_K \tag{37}$$

Here the ε-subscript K denotes strain amplitude derived from the K amplitude. Conversion of ΔK or Δε (excursions) to maximum values is defined in terms of the load ratio R

$$K_{max} = \frac{\Delta K}{1 - R} \qquad \epsilon_{max} = \frac{\Delta\epsilon}{1 - R} \tag{38}$$

All of the variables in the right-hand bracket of Eq. (36)(as well as m) are measured from the ordinary or the cyclic stress-strain curves of the material, in a

manner to be described later. The measured tensile values are converted to true stress $\bar{\sigma}$ and true longitudinal strain $\bar{\varepsilon}_\ell$ for insertion in Eqs. (36) and (37). However, the form of the cyclic stress-strain curve, with Bauschinger effect, is smoothed out, rendering it markedly different, less angular, than that for the virgin material.

A. Dry FCP Growth Extreme

We associate the equilibrium cyclic curve with fatigue crack propagation in a benign or vacuum environment, applying the stress relaxation term of Eq. (36). If we index the cyclic flow properties by numeral 2, as likewise the growth associated with it, the appropriate parts of Eq. (36) are

$$\Delta a_2 = 2m\, d_T\, \ell n \left(1 + \frac{t_H}{t_L}\right)\left[\epsilon_{G2}\left(\frac{\bar{\theta}_{p2}}{\bar{\sigma}_2} - 1\right)\right]^{-1} \tag{39}$$

where ε_{G2}, $\bar{\sigma}_2$, and $\bar{\theta}_{p2}$ are functions of the true tensile strain $\bar{\varepsilon}_2$ of the cyclic stress-strain envelope. It is notable here that time enters only in a relative sense, a function of the form of the loading pattern, not its frequency, as is consistent with the frequency independence of fatigue crack propagation in vacuum. The frequency independence of air-environment growth is related to this but has further implications to be discussed later.

B. Sustained Load Cracking Extreme

At the other extreme we associate the ordinary virgin-material, first (quarter) cycle properties, denoted by subscript numeral 1, with the extreme case of steady loading, static fatigue under severe environmental attack. Here, only the V_S term is applicable since with its linear dependence on time it is generally much larger than the m term, which decreases with time. The appropriate part of Eq. (36) is

$$\Delta a_1 = 8V_s\Delta t \left[\epsilon_{G1}\left(\frac{\bar{\theta}_{p1}}{\bar{\sigma}_1} - \frac{\sqrt{3}}{2}\right)\right]^{-1} \tag{40}$$

where ε_{G1}, $\bar{\sigma}_1$, and $\bar{\theta}_1$ are functions of the true tensile strain $\bar{\varepsilon}_1$ of the ordinary stress strain curve. The coefficient $\sqrt{3}/2$, vs unity of Eq. (39) is to correct the instability condition for plane strain triaxiality, as proposed by Williams and Turner [17]. It has the effect of deferring the instability point to a later strain, for which $\bar{\theta}_{p1}/\bar{\sigma}_1 = 0.866$. The data correlations indicate that the $\sqrt{3}/2$ coefficient is unnecessary, if not undesirable, for cyclic growth predictions. Hence, it is reasoned that the

reverse straining due to cyclic loading has the effect of "limbering up" the ligament so as to relax the local triaxiality. The $\sqrt{3}/2$ coefficient is retained for analysis of stress corrosion cracking (in Eq. 40) because for certain high-strength maraging steels, which show early maximum load points followed by a protracted flat-topped stress-strain curve, it defers the instability point beyond the maximum load point to strain levels consistent with a fracture toughness and process zone size indicated by fatigue crack growth modelling.

C. Triaxiality Effects

Consistent with the instability triaxiality correction at the K_{Ic} limit, the yield condition is also assumed to be affected by local triaxiality. A Tresca yield condition applied to the elastic, plane-strain conditions which should border the plastic zone, equal in size to d_T at this point, is : $\sigma_x = \sigma_y$; $\sigma_z = 2\nu\sigma_y$. This gives a difference of principal stresses $\sigma_y - \sigma_z = \sigma_y(1-2\nu)$ or a triaxiality factor of $1/1-2\nu$. This is introduced by augmenting the measured elastic plus plastic strain by

$$\left(\frac{1}{1-2\nu} - 1\right)\frac{\sigma_{YS}}{E} = \frac{2\nu}{1-2\nu}\frac{\sigma_{YS}}{E}$$

where σ_{ys} is tensile yield strength and ν is the elastic Poisson ratio. In Equation (37) then, $\Delta\epsilon_K$ is augmented

$$\Delta\epsilon_K = \epsilon_{K1} = \bar{\epsilon}_1 + \frac{2\nu}{1-2\nu}\frac{\sigma_{YS}}{E} \qquad (41)$$

and in Eq. (40) $\epsilon_{G1} = \epsilon_{K1}$. This triaxiality factor for the yield condition has the effect of elevating the K-proportional strain, via Eq. (37), at which plastic flow, hence non-infinite plastic strain hardening $\bar{\theta}_{pl}$, commences. An infinite $\bar{\theta}_{pl}$ means infinite stability, hence zero growth by Eq. (40). Numerous cases of severe corrosion-induced crack propagation appear to be correctly predicted by use of this threshold-offset formulation. However it does not always work, generally underestimating the K_{Iscc} threshold for softer/tougher materials, one of the deficiencies for which this study suggests remedy.

6. OPTIONS IN MIXING OF GROWTH RATE FACTORS

An obvious approach to predicting corrosion fatigue crack growth is by mixing additively the transfer functions which seem to work for each limit: vacuum fatigue at the lower end of the growth rate scale, Eq. (39); and stress corrosion cracking, Eq. (40), at the upper. But this does not work! In seeking a successful scheme for combining the ingredients for growth, a large number of different sets of

modelling assumptions were tried. Briefly, as it turns out, there appear to be two distinct rate-limiting criteria in corrosion-fatigue crack propagation. The obvious one is the surface annihilation/corrosion rate V_S in the general context of Eq. (40). Here the correct selection of crack tip condition is critical. We have been able to do this by exercising only binary, either/or decision options: either crack tip conditions pertaining to cyclic attributes; or else those pertaining to uncycled, sustained-load attributes, may be employed. The second criterion, dependent upon correct assessment of the surface attack criterion , is one of constant ratio of plastic strain rate at the crack tip to the surface annihilation rate. The first criterion is apparently governed by the corrosion process: it is frequency dependent and sets the level of the Stage II growth corrosion fatigue. The second criterion is thought to reflect a dearth of fresh clean surface for environmental attack. Here the plastic straining, exposing nascent surface is outpaced by the corrosion rate, so that corrosion products tend to seal off the surface, effectively arresting that straining. To explain this, the following sections will treat the manner of estimating the V_S limit, then the strain rate field, then their combination leading to the second criterion.

7. SPECIAL CONDITIONS OF FATIGUE CRACK PROPAGATION

We have described rather completely the terms of the sustained load cracking model, summarized by Eq. (40). Conditions surrounding the "dry" fatigue growth are somewhat more involved, since the effects of load, hence strain-reversal, on the mean stress location, and on the effective strain gradient ε_{G2} require special definition. Consider these now in turn.

A. Mean Stress Centroid Relocation

Consider a tensile test, Fig. 2 in which the strain is reversed and then restored repeatedly at various points. If the reversal is attempted just beyond the proportional limit, point (a), the plastic yielding will induce stress relaxation. Since the true partial of stress relaxation is along the zero plastic strain, or elastic-load line, the cyclic stress-strain envelope will tend to slide back across the abscissa. In a low cycle fatigue test, in which only the strain excursion, not its absolute position, is controlled, the centroid of area of the cyclic stress-strain envelope will slip down to rest upon the zero-stress axis (30). This effect is attributed to the inequality of stress relaxation rates due to the imbalance of tensile and compressive stresses. It is consistent with the assumption,

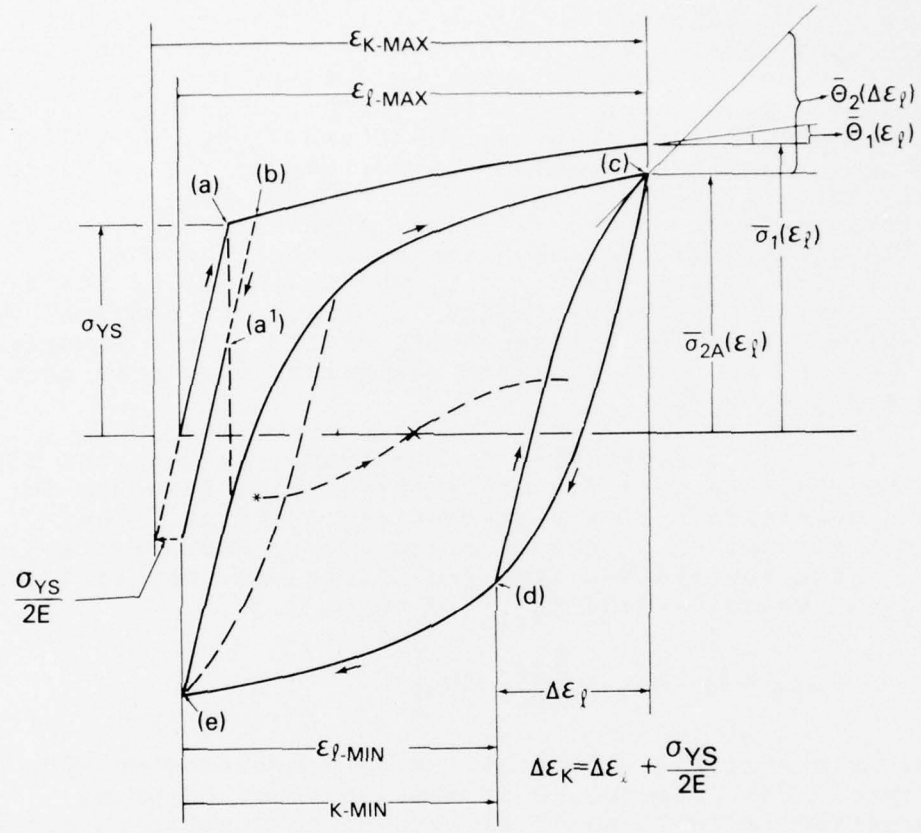

Fig. 2 — Various plastic flow terms as determined from the true stress-strain envelopes obtained from the flow property test

Sec. 4 .D. and Eq. (28), of a constant relative strain-rate sensitivity, for which the stress relaxation $\Delta\bar{\sigma}_m$ is proportional to the level of flow stress $\bar{\sigma}$.

How does centroid relocation occur at the crack tip? Here the most that can be assumed is that upon unloading the crack, collapse of the elastic stress field outside the plastic zone will drive the crack tip strain back to zero. It may not be supposed to drive it into the compressive strain quadrants. Thus, although the conditions for stress relaxation are present at point (a), there is no available permissible path along which the shift can occur. To make available sufficient compressive-stress scope, an additional strain, by simple geometric construction on Fig. 2 approximately equal to $\sigma_{YS}/2E$, must be provided. This is done by requiring a value of ΔK, with its strain equivalent via Eq. (1) of $\Delta\varepsilon_K$, greater than the measured longitudinal elastic plus plastic strain from the lower toe of the cyclic stress curve. The amount added is simply the constant value of $\sigma_{YS}/2E$. Thus for a given total cyclic strain excursion $\Delta\bar{\varepsilon}_2$ (at R = 0), the required equivalent strain is then $\Delta\varepsilon_{K2} = \Delta\bar{\varepsilon}_2 + \sigma_{YS}/2E$.

A further consideration is required. As the load ratio R increases, the need for an incursion path into the forbidden compressive strain quadrant is obviated. The minimum strain, $\bar{\varepsilon}_{2min}$ for a given strain excursion $\Delta\varepsilon_2$, is $R\,\bar{\varepsilon}_2$. Thus for cycle-2 type growth, we add only that part of $\sigma_{YS}/2E$ which exceeds $\bar{\varepsilon}_{2min}$, whence

$$\Delta\epsilon_{K2} = (1 - R)\bar{\epsilon}_2 + \left[\frac{\sigma_{YS}}{2E} - R\bar{\epsilon}_2\right] \tag{42}$$

where only positive values of the square-bracketed term are employed. The consequence of this in terms of crack propagation is to "freeze" effects of load ratio on growth rate (threshold) for R values above 1/3. This is seen from Eq. (42) by substituting σ_{YS}/E for $\Delta\bar{\varepsilon}_2$, making its term zero at R = 1/3. This attribute is desired for vacuum fatigue data, for which R-effects vanish above R ≃ 1/3, to be demonstrated later.

The next question is how to set the peak-position cyclic properties for R > 0. Our perception of this is depicted by the envelope peaking at point (c) of Fig. 2 for an R of 5/7. The form of this envelope, following the Massing hypothesis (31) (which we corroborate), is as though the full cyclic envelope were traversed from its negative toe to a total strain equal to that of the strain excursion. Thus the value of $\bar{\sigma}_{p2}$ used in Eq. (39) is that for

$$\bar{\theta}_2 = \bar{\theta}_2(\Delta\bar{\epsilon}_2) \quad \text{where} \quad \Delta\bar{\epsilon}_2 = (1-R)\bar{\epsilon}_{2,max}$$

Should then the stress level associated with the point (c) be adjusted downward for centroid neutralization? It seems reasonable that this should be so. However, our trails show this to spoil some details of correlation. Hence, seeking reasons why it should not we note that the path of strain reversal must follow that of the full cyclic curve, of which it is, in effect, a part: the path d-e of Fig. 2. If we permit the c-d envelope to skew down, execution of the d-e path would require a path excursion into the "effectively inaccessible" zone. Since this is not permitted, we justify retaining the c-d envelope pushed up against a "roof" defined by the full cyclic envelope.

For the purpose of calculating the position of this "roof", we designate the compressive stress corresponding to the negative toe of the full cyclic stress-strain curve as σ_{CUS}, the compressive "ultimate strength" analogous to σ_{TUS} for the familiar tensile ultimate. In our manner of testing for the cyclic envelope, this point is at zero strain, hence σ_{CUS} is a "true" stress. It is then added to true stress values calculated from tensile load relative to the zero load/stress axis. Calling this stress $\bar{\sigma}_{2A}$, we define an effective or averaged stress for a given $\bar{\epsilon}_2$ total cyclic envelope

$$\bar{\sigma}_{2A} = \frac{\bar{\sigma}_2 + \bar{\sigma}_{CUS}}{2} \tag{43}$$

This value $\bar{\sigma}_{2A}$ then replaces $\bar{\sigma}_2$ in the right bracket of Eq. (39).

B. Strain Field Gradient

The remaining variable in the cyclic growth equation (39) is the gradient strain ϵ_{G2}. In sustained load cracking, without unloading, this is clearly to be associated with the maximum strain level. However, insisting that maximum strain values be used in the cyclic growth model, Eq. (39), has resulted in prediction of a generally unobserved negative sensitivity of the FCP rate to load ratio. To effect correlations, we have had to assume that the gradient strain in FCP must be associated with the strain excursion in that cycle. Rationale for this expedient is to imagine that plastic strain reversal in any amount at the crack tip has the effect of cancelling out the tensile strain gradient (at $r = d_T$). The new gradient restored upon reversal again to tension should reflect only the positive strain excursion from this "zero base", not that from the

original zero strain, zero base. Thus the K-equivalent strain excursion $\Delta\varepsilon_{K2}$ is used to replace ε_{G2} in Eq. 39, which for $R \geq 1/3$ equals $\Delta\bar{\varepsilon}_2$. The use of $\Delta\varepsilon_{K2}$ vs $\Delta\bar{\varepsilon}_2$ for $R < 1/3$, is again an expedient in view of the Bucci corrosion fatigue data at high R levels, to be discussed later.

C. Choice of Conditions for Transitional Growth Factor

Crack tip conditions for cyclic m-induced growth are likely to affect those for subsequent environmental augmentation. The continuation of the m-induced growth must surely be at the same local stress level $\bar{\sigma}_{2A}$, and in the same local strain gradient $\Delta\varepsilon_{K2}$. However, in estimating the centroid neutralization displacement, the first cycle curve, Fig. 2, always has an origin of reference at the zero strain ordinate. It cannot move out from here as does the cyclic envelope, whose shape is strain-excursion, rather than maximum-strain, dependent. Thus the calculation of $\Delta\varepsilon_{K1}$ from $\Delta\bar{\varepsilon}_1$ omits a minimum strain adjustment $(R/1-R)\,\Delta\bar{\varepsilon}_1$. Otherwise its calculation is identical to that for $\Delta\varepsilon_{K2}$. Specifically, from the first cycle true stress $\bar{\sigma}_1$, vs true strain $\bar{\varepsilon}_1$ curve we define

$$\Delta\bar{\epsilon}_1 = (1 - R)\bar{\epsilon}_1 \tag{44}$$

and

$$\Delta\epsilon_{K1} = \Delta\bar{\epsilon}_1 + \frac{\sigma_{YS}}{2E} \tag{45}$$

This value of $\Delta\varepsilon_{K1}$ is converted to ΔK by its insertion in Eq. (37), to be aligned (by interpolation) with values obtained by inserting $\Delta\varepsilon_{K2}$ from Eq. (42) for the purpose of summing growth rate effects.

Obviously all transition factors cannot be the same, or the predicted CFCP characteristics would not differ from those of FCP. The difference is due to the strain hardening rate, for which first cycle properties pertain. On the curve of $\bar{\sigma}_1$ vs $\bar{\varepsilon}_1$, the $\bar{\theta}_1$ values are read as a function of $\bar{\varepsilon}_1$, the maximum strain value. The true plastic strain hardening $\bar{\theta}_{P_1}$ is then computed from $\bar{\theta}_1$, according to formulas given in section 10.

The environmental attack effective in one cycle is hard to visualize as a constant corrosion rate, V_S.
the total surface annihilation depth averaged over the cycle time is used in the transitional growth

formulation, Δr_T being substituted for $V_s \Delta t$ of Eq. 40.

8. SUMMARY OF GROWTH FACTOR FORMULAS

Preceding sections cite ingredients of the three different "growth rate factors" now collected. Assume we have measured ordinary tensile, then full cyclic-equilibrium stress-strain curves and have converted their measurements to "true" values of $\bar{\sigma}$ and $\bar{\theta}_p$ as functions of true longitudinal strain $\bar{\epsilon}$. Let subscript 1 denote first excursion properties, 2 denote cyclic properties and 2/1 those selected as germane to the transitional stage between dry fatigue 2 and constant load cracking 1. The specific equations are cited below in the order in which they govern: dry cyclic fatigue, cyclic fatigue/corrosion augmentation, and the static fatigue corrosion induced crack growth. The bracketed strains indicate the functional dependency.

For dry FCP, Eq. (39) becomes

$$\Delta a_2 = 2m\, d_T\, \ell n \left(1 + \frac{t_H}{t_L}\right)\left[\Delta\epsilon_{K2}\left(\frac{\bar{\theta}_{p2}(\Delta\bar{\epsilon}_2)}{\bar{\sigma}_{2A}(\bar{\epsilon}_2)} - 1\right)\right]^{-1} \tag{46}$$

and Eq. (37)

$$\Delta K = \sqrt{2\pi\, d_T}\; E\Delta\epsilon_{K2} \tag{47}$$

in which, from Eq. 42

$$\Delta\epsilon_{K2} = (1-R)\bar{\epsilon}_2 + \left[\frac{\sigma_{YS}}{2E} - R\bar{\epsilon}_2\right] \tag{48}$$

where only positive values of the square bracketed term are employed.

For the cyclic fatigue corrosion augmentation, Eq. (40) modified as discussed in Sec 7.C. becomes

$$\Delta a_{2/1} = (8\Delta r_T)\left[\Delta\epsilon_{K2}\left(\frac{\bar{\theta}_{p1}(\bar{\epsilon}_1)}{\bar{\sigma}_{2A}(\bar{\epsilon}_1)} - 1\right)\right]^{-1} \tag{49}$$

and Eq. (37)

$$\Delta K = \sqrt{2\pi\, d_T}\; E\Delta\epsilon_{K1} \tag{50}$$

where

$$\Delta\epsilon_{K1} = (1 - R)\bar{\epsilon}_1 + \frac{\sigma_{YS}}{2E} \tag{51}$$

In Equation 49, $\bar{\sigma}_{2A}$ is given as a function of $\bar{\epsilon}_1$, when it is in fact a second excursion (cyclic) property. The equivalencing of $\bar{\sigma}_{2A}(\bar{\epsilon}_1)$ with the appropriate $\bar{\sigma}_{2A}(\epsilon_2)$ is carried out through an interpolation scheme to be described in Section 11. For static fatigue corrosion-induced crack growth, Eq. (40) becomes

$$\frac{\Delta a}{\Delta t}_1 = 8V_s \left[\epsilon_{K1} \left(\frac{\bar{\theta}_{p1}(\bar{\epsilon}_1)}{\bar{\sigma}_1(\bar{\epsilon}_1)} - \frac{\sqrt{3}}{2} \right) \right]^{-1} \tag{52}$$

and Eq. (37)

$$K = \sqrt{2\pi d_T}\ E\epsilon_{K1} \tag{53}$$

where repeating Eq. (41)

$$\epsilon_{K1} = \bar{\epsilon}_1 + \frac{2\nu}{1 - 2\nu} \frac{\sigma_{YS}}{E} \tag{54}$$

For convenience in further development, that portion of each growth equation derived from the form of the stress-strain curve (except for m) is called a growth rate factor G, specifically:

$$G_2 = \left[\Delta\epsilon_{K2} \left(\frac{\bar{\theta}_{p2}}{\bar{\sigma}_{2A}} - 1 \right) \right]^{-1} \tag{55}$$

$$G_{2/1} = \left[\Delta\epsilon_{K2} \left(\frac{\bar{\theta}_{p1}}{\bar{\sigma}_{2A}} - 1 \right) \right]^{-1} \tag{56}$$

$$G_1 = \left[\epsilon_{K1} \left(\frac{\bar{\theta}_{p1}}{\bar{\sigma}_1} - \frac{\sqrt{3}}{2} \right) \right]^{-1} \tag{57}$$

A. Procedure for Mapping Parametric Growth Factor Curves

The parametric curves of the frequency-dependent part of CFCP are obtained by adding to the basic growth Δa_2, Eq. (46) or actually a function directly proportional

to it, G_2 Eq. (55), successively regularly larger amounts of $\Delta a_{2/1}$, Eq. (49), or its proportional function, $G_{2/1}$ Eq. (56). The sum required is:

$$\frac{\Delta a}{(\Delta N)} = \Delta a_2 + \Delta a_{2/1} = 2m\, d_T\, \ell n \left(1 + \frac{t_H}{t_L}\right) G_2 + 8\Delta r_T G_{2/1} \tag{58}$$

$$= f_2(m)G_2 + f_1(\Delta r_T)G_{2/1} \tag{59}$$

where Δa is the predicted crack growth increment for one fatigue cycle. Since G_2 is basic, we factor out its coefficient

$$\frac{\Delta a}{f_2} = G_2 + \frac{f_1}{f_2} G_{2/1} \tag{60}$$

In mapping these parametric curves, we substitute a geometric series for the coefficient of $G_{2/1}$, specifically

$$\frac{f_1}{f_2} = 2^N \times 10^{-3} \qquad 0 \leqslant N \leqslant 15 \tag{61}$$

This series of values for the coefficient of $G_{2/1}$ results in a family of curves which span the range of observed CFCP behavior for the materials considered. For future reference a particular member of this family will be designated

$$\frac{\Delta a}{f_2(m)} = G(N) \tag{62}$$

The actual numerical summations of $G(N)$ must be made at equal values of $\Delta\varepsilon_{K1}$ and $\Delta\varepsilon_{K2}$. This is accomplished by an interpolation to be detailed later.

9. STRAIN RATE FOR CRACK PROPAGATION

The concept of such a rate of straining inheres this modelling logic, as it is the means by which the stabilizing strain is provided from crack growth. Recall from Eq. 34, crack-tip strain rate combines effects of crack loading and crack growth as follows

$$d\bar{\epsilon}_p = d\epsilon_L + \frac{\epsilon_G}{2d_T}\, da \tag{34}$$

As noted earlier, the gradient strain ϵ_G for CFCP is taken to be $\Delta\epsilon_K$. Substituting also the crack propagation increment in the context of Eq. (62), Eq. (34) becomes, in incremental form,

$$\Delta\bar{\epsilon}_p = \Delta\epsilon_L + \frac{\Delta\epsilon_K}{2d_T}\, f_2(m) \quad G(N) \tag{63}$$

We have observed that the map of <u>plastic</u> strain rate rather than total elastic plus plastic strain rate provides the more "data-consistent" delineation of the frequency independent contour lines. Accordingly we seek to remove the elastic strain component. To do this we deduct $2\bar{\sigma}_{2A}/E$ from the cyclic-envelope elastic strain

$$\Delta\bar{\epsilon}_p = \Delta\bar{\epsilon}_2 - \frac{2\bar{\sigma}_{2A}(\Delta\bar{\epsilon})_2}{E} + \Delta\epsilon_K m\,\ell n\left(1 + \frac{t_H}{t_L}\right) \quad G(N) \tag{64}$$

where $f_2(m)$ has been inserted from Eq. (58) and (59) and $\bar{\sigma}_{2A}$ is a function of the strain excursion $\Delta\bar{\epsilon}_2$ not the maximum strain, as used in connection with Eq. (49). In order to compare with a map of $G(N)$, Eq. (64) can be rearranged

$$m\,\ell n\left(1 + \frac{t_H}{t_L}\right) \quad G(N) = \frac{\Delta\bar{\epsilon}_p - \Delta\bar{\epsilon}_2 + \frac{2\bar{\sigma}_{2A}}{E}}{\Delta\epsilon_K} \tag{65}$$

Abbreviate the left hand term as Y. Note further that $\Delta\bar{\epsilon}_p$ can be expressed as a strain rate by normalizing over the cycle duration Δt

$$\Delta\bar{\epsilon}_p = \frac{\Delta\bar{\epsilon}_p}{\Delta t}\,\frac{\tau}{\tilde{N}} = \frac{\dot{\bar{\epsilon}}_p}{f} \tag{66}$$

where τ is the period of a cycle $\tilde{N}$ of frequency f. With this, and using Eq. (42), Eq. 65 becomes

$$m\,\ell n\left(1 + \frac{t_H}{t_L}\right) \quad G(N) \equiv Y = \frac{\dot{\bar{\epsilon}}_p/f - \Delta\bar{\epsilon}_2 + 2\bar{\sigma}_{2A}/E}{\Delta\bar{\epsilon}_2 + \left[\sigma_{YS}/2E - \frac{R}{1-R}\,\Delta\bar{\epsilon}_2\right]} \quad \{>0 \text{ only}\} \tag{67}$$

This is shown as step (19) in Table 1.

A. Procedure for Mapping Parametric Strain Rate Curves

To map out Eq. (67) we establish a parametric set of values for $\bar{\dot{\epsilon}}_{p/f}$ using the same type of geometric series as for the G (N) map. The values used are

$$\bar{\dot{\epsilon}}_{p/f} = \frac{2^M}{10} \qquad -10 \leq M \leq 4 \tag{68}$$

for a map area sufficient to cover most ranges of CFCP growth.

The maps of growth rate factor, G(N) vs $\Delta\epsilon_K$, and those of constant crack strain rate, $\bar{\dot{\epsilon}}_{p/f}$ vs $\Delta\epsilon_K$, can be superposed by aligning coordinates. The abscissa scales, both in terms of $\Delta\epsilon_K$, may be superposed. For the ordinate scales, we align Y = 1 (Log Y = 0) on the strain rate map in accord with Eq. (65)

$$G(N) = \frac{1}{m\,\ell n\left(1 + \frac{t_H}{t_L}\right)} \tag{69}$$

Alternatively the strain rate maps may be plotted directly in terms of G(N) by inserting known values of m and t.

B. Matching of Combined Curves to CFCP Data

Superposition of the combined map on CFCP data plot produces a value of d_T by the location thereon. The procedure used is to solve the growth equations (62) and (47) for a line on the G vs $\Delta\epsilon_K$ map of constant d_T. Since G varies(inversely)with d_T while $\Delta\epsilon_K$ as its root, this line has a slope +2 on equally scaled logarithmic paper. Our preference is to use graph paper with an abscissa scale twice that of the ordinate, on which this slope appears at a 45° angle. If we select a reference point $\left.\frac{\Delta a}{\Delta N}\right|_{ref}$ = 10 μm/cycle, $\Delta K|_{ref}$ = 10 MPa $\sqrt{m}$ on the data plot, a corresponding point on the G vs $\Delta\epsilon_K$ match line is, from substitution in Eqs. (62) and (47) and rearranging with d_T set at 100 μm

$$G|_{ref} = \frac{1}{20m\,\ell n\left(1 + \frac{t_H}{t_L}\right)} \tag{70}$$

$$\Delta\epsilon_K|_{ref} = \frac{1000}{\sqrt{2\pi}\,E} \quad \text{(in MPa)} \tag{71}$$

Matching involves sliding the plots to a best fit with the match line of slope 2 through the point $(\Delta\varepsilon_K, \quad G)\,|_{ref}$ passing through the $(\Delta K, \Delta a/\Delta N)|_{ref}$ point. Using this specific value of $\Delta\varepsilon_K|_{ref}$ (any other could be chosen) is convenient in that in match location it corresponds on the ΔK scale to $\sqrt{d_T}$ (in μm). The match must also honor the location of $K = K_{IC}$ which should correspond to the $\Delta K/(1-R)$ at which $G_1 \to \infty$.

10. PROCEDURES FOR OBTAINING PLASTIC FLOW DATA

The manner of processing data to obtain the parametric growth rate factor maps will depend on the form of the data. Hence we interject at this point a brief description of how ours was obtained. Tensile and full-cycle equilibrium tension-compression stress-strain curves of the material are needed. In the data shown here, the cyclic curve is obtained after an initial tensile excursion to a strain slightly exceeding that for maximum load. This allows measurement of Θ_d to the slightly negative values required to make $\bar{\Theta}_{pl}/\bar{\sigma}_1$, reach the value $\sqrt{3}/2$ in Eq. (57). Subsequent to this, straining is reversed and initial length is restored. At this point the cyclic measurement commences. Again the specimen is extended to slightly beyond maximum load. In the ferrous alloy used here, this curve is equivalent to the equilibrium cyclic curve. However, in the titanium alloys, further cycling will typically introduce the two-stage hardening effect. We had sought to avoid this effect in early modelling attempts as there appears to be no undulation in FCP which corresponds to that reflecting two-stage hardening in the G (N) profiles, the parametric lines of constant "N" in the growth rate factor maps. It is now apparent that the constant strain-rate/corrosion-rate profiles, lines of constant N-M, will fit the data evenwith inclusion of two stage hardening. For normal growth increments, much smaller than d_T, each ligament should experience many strain cycles. Consequently, the condition of two stage hardening should occur at the crack tip. Accordingly, we now recommend continued cycling in these measurements until a true equilibrium condition is established. The strain excursion applied should not exceed that for the equilibrium-condition maximum load, to assure maximum endurance of the specimen. It is important that the flow measurements be made on specimens which have not begun to fracture, which is favored by a minimal strain excursion. The tensile specimen axis is oriented normal to the crack surface, to simulate d_T-ligament orientation. Miniature tensile specimens are employed with test section d_o = 4.32 mm diameter and length about 13 mm. Deformation is sensed with a diametral bi-lobed clip type strain gage, although we now believe that longitudinal

strain measurement would be more desirable. This would remove the necessity to convert to longitudinal strain for use in the model calculations providing better definition in the growth threshold region. Usually several tests of the same material are run to assure reproducibility of the data. The cyclic envelope is held in the positive longitudinal (= negative diametral) strain quadrants, as noted earlier, to better simulate the crack tip condition of no potential for compressive strain. The two curves scaled in terms of engineering stress $\sigma = P/A_o$ and diametral strain $\varepsilon_d = \Delta d/d_o$ are marked at closely spaced strain stations, particularly in the low strain and/or high curvature regions. At each station, the tensile stress σ_T and slope $d\sigma_T/d\varepsilon_d$ are measured and recorded. Specific point measurements on each curve, distinguished as before by subscript 1 for ordinary and 2 for cyclic, are required:

Tensile yield strength, σ_{YS} (at 0.2% offset);
Elastic diametral moduli, $\theta_{d0,1}$, $\theta_{d0,2}$; and
Compressive Ultimate Strength, σ_{CUS}

Additionally a value of the longitudinal elastic modulus E is needed; one may normally employ handbook values. This permits the Poisson ratio to be calculated.

$$\nu_{e,i} = -\frac{E}{\theta_{d_{0,i}}} \qquad i = 1, 2 \tag{72}$$

Values of ν specific to each curve must be retained since those for the cyclic toe are sometimes higher, i.e., $\theta_{d0,2} < \theta_{d0,1}$.

Data for determining the stress relaxation exponent m is obtained by abruptly stopping the testing machine head, with load recorder gain increased by a factor of 10, and observing the consequent load slackening with electrically imparted time marks superposed on the strain signal. This is usually done in a region of low strain hardening rate to obviate errors from this source, noted earlier. A cross plot of log stress decrement vs log time, provides a slope of value m in accordance with Eq. (25).

A. Conversion to True Values

The load and diametral contraction data are converted into true stress and true longitudinal strain using the following formulas, which can be found in references on low-cycle fatigue techniques. For clarity in this section d and ℓ represent diametral and longitudinal respectively.

As previously noted the ℓ-subscript designation is omitted for brevity of other equation formulations. Subscripts e and p represent elastic and plastic. The diametral strain is first converted to "true" strain because the formulas which follow are not valid otherwise:

$$\bar{\epsilon}_d = \int_{d_0}^{d} \frac{dD}{D} = \ell n \left(\frac{d}{d_0}\right) = \ell n \left(\frac{d_0 + \Delta d}{d_0}\right) \tag{73}$$

$$\bar{\epsilon}_d = \ell n (1 + \epsilon_d) \tag{74}$$

in which $\epsilon_d = \frac{\Delta d}{d_o}$, which is the measured engineering strain.

The true stress is computed from the uniaxial load

$$\bar{\sigma} = P/A = \frac{P}{A_0} \frac{A_0}{A} = \sigma_T \left(\frac{d_0}{d}\right)^2 \tag{75}$$

$$\bar{\sigma} = \sigma_T (1 + \epsilon_d)^{-2} \tag{76}$$

in which σ_T is the measured engineering stress. The conversion of diametral strain to true longitudinal strain is effected by considering the elastic and plastic components separately

$$\bar{\epsilon}_d = \bar{\epsilon}_{d,e} + \bar{\epsilon}_{d,p} = \frac{\bar{\sigma}}{\theta_0} + \bar{\epsilon}_{d,p} \tag{77}$$

in which Θ_0 is the elastic modulus from the stress/diametral strain measurement for the excursion (first or cyclic) being considered. Therefore

$$\bar{\epsilon}_{d_p} = \bar{\epsilon}_d - \frac{\bar{\sigma}}{\theta_0} \tag{78}$$

For plastic strain only, Poisson's ratio $\nu = 0.5$, and

$$\bar{\epsilon}_{\ell,p} = -\frac{\bar{\epsilon}_{d,p}}{\nu} = -2\bar{\epsilon}_{d,p} \tag{79}$$

The longitudinal strain is similarly decomposed

$$\bar{\epsilon}_\ell = \bar{\epsilon}_{\ell,e} + \bar{\epsilon}_{\ell,p} = \frac{\bar{\sigma}}{E} - 2\bar{\epsilon}_{d,p} \tag{80}$$

$$\bar{\epsilon}_\ell = \frac{\bar{\sigma}}{E} - 2\bar{\epsilon}_d + \frac{2\bar{\sigma}}{\theta_0} \tag{81}$$

Since the elastic moduli are related through the elastic Poisson's ratio, Eq. (72), we can express Eq. (81) as

$$\bar{\epsilon}_\ell = (1 - 2\nu_e)\frac{\bar{\sigma}}{E} - 2\bar{\epsilon}_d \tag{82}$$

Finally, the instantaneous slope, $\bar{\theta}_\ell$, of the true stress true longitudinal strain curve is computed using the following relationships:

$$\bar{\theta}_d = \frac{d\bar{\sigma}}{d\bar{\epsilon}_d} = \frac{d\bar{\sigma}}{d\epsilon_d}\frac{d\epsilon_d}{d\bar{\epsilon}_d} \tag{83}$$

$$= \left[\frac{\frac{d\sigma_T}{dc_d}}{(1+\epsilon_d)^2} - \frac{2\sigma_T}{(1+\epsilon_d)^3}\right](1+\epsilon_d) \tag{84}$$

$$= \frac{\theta_d}{(1+\epsilon_d)} - \frac{2\sigma_T}{(1+\epsilon_d)^2} = \frac{\theta_d}{(1+\epsilon_d)} - 2\bar{\sigma} \tag{85}$$

in which θ_d is the measured slope of the engineering stress/diametral strain curve. From this quantity, $\bar{\theta}_\ell$ is computed:

$$\bar{\theta}_\ell = \frac{d\bar{\sigma}}{d\bar{\epsilon}_\ell} = \frac{d\bar{\sigma}}{d\bar{\epsilon}_d}\frac{d\bar{\epsilon}_d}{d\bar{\epsilon}_\ell} = -\frac{1}{2}\bar{\theta}_d \tag{86}$$

$$= \frac{1}{2}\left[\frac{\theta_d}{1+\epsilon_d} - 2\bar{\sigma}\right]$$

11. COMPUTER PROGRAM FOR GROWTH AND STRAIN RATE FACTORS

Table I provides a set of computational formulas about which the computer program* was fashioned. Each step is numbered so that the following comments can be easily referenced, although most steps should be self evident. Generally, calculations pertaining to first cycle or ordinary tensile properties are on the left of the table; cyclic properties on the right.

Step 1) converts nominal stress to true and on extreme right provides the centroid normalized cyclic stress $\bar{\sigma}_{2A}$.

Step 2) converts to true strain hardening, still diametral.

Step 3) converts to true longitudinal elastic plus plastic strain hardening.

Carrying on through Step 6), two lists of true stress ($\bar{\sigma}_1$, $\bar{\sigma}_{2A}$), true strain hardening values ($\bar{\theta}_1$, $\bar{\theta}_2$) versus true, R-adjusted strain range ($\Delta\bar{\varepsilon}_1$, $\Delta\bar{\varepsilon}_2$) are established. However, their strain-wise positions do not necessarily coincide, and in order to proceed with the addition in G(N), we must achieve this coincidence. It would be possible to interon one set with respect to the other, but for greater uniformity and accuracy in a subsequent interpolation, we interpolate both $\Delta\bar{\varepsilon}_1$ and $\Delta\bar{\varepsilon}_2$ bases with respect to a third station set — a geometric series with intervals of logarithmic spacing of 5%, and a strain range which covers that of these materials. That operation is given in Step 7), and the interpolation is carried out in Step 8). It is helpful to note that interpolating for $\bar{\sigma}$ or $\bar{\theta}$ by addressing the $\Delta\bar{\varepsilon}$ list results in values which correspond to an $\bar{\varepsilon}_{max}$ value equivalent to $\Delta\bar{\varepsilon}/(1-R)$. Conversely, if one interpolates on the $\bar{\varepsilon}_{max}$ list, values of $\bar{\sigma}$ and $\bar{\theta}$ would correspond to R-adjusted strain range, $\Delta\bar{\varepsilon}$ values.

Step 9) adds the centroid neutralization strain to the measured longitudinal (true) strain. However since this correction differs between the two sets for $R < 1/3$, it is necessary to interpolate again to realign the stations at which the summations are to occur. Step 11) specifies this. Step 12), removal of the elastic part of the strain hardening creating a singular point, is done here, after the interpolations, since linear interpolations suffer in accuracy when approaching a singularity.

Step 13) is the answer line, the two growth factors $G_{2/1}$ and G_2 needed for the mapping, which is specified in step 14).

---

* Available from authors on request.

TABLE I

TLIM Calculation Procedure Ordinary Tensile Curve (1) from $\sigma_1 = 0$, Meas. σ_1, θ_{d1} vs ϵ_{d1}; σ_{YS}, σ_{TUS}, θ_{01}, E, m	Full Cyclic Equilibrium Curve (2) from σ_{CUS} toe, Meas. σ_2 θ_{d2} vs ϵ_{d2}; σ_{CUS}, θ_{02}
(1) $\bar{\sigma}_1 = \sigma_1/(1+\epsilon_{d1})^2$	$\bar{\sigma}_2 = \sigma_2/(1+\epsilon_{d2})^2$; $\bar{\sigma}_{2A} = \dfrac{\bar{\sigma}_2 - \bar{\sigma}_{CUS}}{2}$
(2) $\bar{\theta}_{d1} = \theta_{d1}/(1+\epsilon_{d1}) - 2\bar{\sigma}_1$	$\bar{\theta}_{d2} = \theta_{d2}/(1+\epsilon_{d2}) - \bar{\sigma}_2$
(3) $\bar{\theta}_1 = -\bar{\theta}_{d1}/2$	$\bar{\theta}_2 = -\bar{\theta}_{d2}/2$
(4) $\bar{\epsilon}_{d1} = \ln(1+\epsilon_{d1})$	$\bar{\epsilon}_{d2} = \ln(1+\epsilon_{d2})$
(5) $\bar{\epsilon}_1 = (1 - E/\theta_{01})\dfrac{\bar{\sigma}_1}{E} - 2\bar{\epsilon}_{d1}$	$\bar{\epsilon}_2 = (1 - E/\theta_{02})\dfrac{\bar{\sigma}_2}{E} - 2\bar{\epsilon}_{d2}$
(6) $\Delta\bar{\epsilon}_1 = (1-R)\bar{\epsilon}_1$	$\Delta\bar{\epsilon}_2 = (1-R)\bar{\epsilon}_2$
(7) (a) Establish from steps (1), (3), (5), and (6), list of sets: of σ_1, $\bar{\theta}_1$, $\bar{\epsilon}_1$, $\Delta\bar{\epsilon}_1$; of $\bar{\sigma}_{2A}$, $\bar{\theta}_2$, $\bar{\epsilon}_2$, $\Delta\bar{\epsilon}_2$	
(b) Establish log-uniform ϵ-station set; $\epsilon = 10^{0.05L-3}$ $\quad 0 \leq L \leq 40$	
(8) Interpolate to set ϵ on $\Delta\bar{\epsilon}_1$ list: $\bar{\theta}_1 = \bar{\theta}(\bar{\epsilon}_{max})$; on $\Delta\bar{\epsilon}_2$ list: $\bar{\sigma}_{2A} = \bar{\sigma}(\bar{\epsilon}_{max})$; on $\bar{\epsilon}_2$ list: $\bar{\theta}_2 = \bar{\theta}(\Delta\bar{\epsilon})$, $\bar{\sigma}_{2A} = \bar{\sigma}(\Delta\bar{\epsilon})$	
(9) $\Delta\epsilon_{K1} = \Delta\bar{\epsilon}_1 + \dfrac{\sigma_{YS}}{2E}$	$\Delta\epsilon_{K2} = \Delta\bar{\epsilon}_2 + \left[\sigma_{YS}/2E - \dfrac{R}{1-R}\Delta\bar{\epsilon}_2\right]$ $\left\{\begin{matrix}>0\\ \text{Values}\\ \text{Only}\end{matrix}\right\}$
(10) (a) Establish from steps (8) and (9), list of sets of $\bar{\theta}_1$, $\Delta\epsilon_{K1}$; $\bar{\theta}_2$, $\bar{\sigma}_{2A}$, $\Delta\epsilon_{K2}$.	
(b) Establish second ϵ-set as in (7)	
(11) Interpolate to set ϵ values: $\bar{\theta}_1(\Delta\epsilon_{K1})$; $\bar{\theta}_2(\Delta\epsilon_{K2})$; $\bar{\sigma}_{2A}(\Delta\epsilon_{K2})$	
(12) $\bar{\theta}_{p1}^{-1} = \bar{\theta}_1^{-1} - \theta_{01}^{-1}$	$\bar{\theta}_{p2}^{-1} = \bar{\theta}_2^{-1} - \theta_{02}^{-1}$
(13) $G_{2/1} = \left[\Delta\epsilon_K\left(\dfrac{\bar{\theta}_{p1}}{\bar{\sigma}_{2A}} - 1\right)\right]^{-1}$	$G_2 = \left[\Delta\epsilon_K\left(\dfrac{\bar{\theta}_{p2}}{\bar{\sigma}_{2A}} - 1\right)\right]^{-1}$
(14) Plot $G(N) = G_2$ & $G_2 + 10^{-3} \cdot 2^N G_{2/1}$; $(0 \leq N \leq 15)$ vs $\Delta\epsilon_K$ on log scale	
(15) $\theta_{p1}^{-1} = \bar{\theta}_1^{-1} - \bar{\theta}_{01}^{-1}$	For Strain Rate Map
(16) $\epsilon_{K1} = \bar{\epsilon}_1 + \left(\dfrac{\theta_{01}}{E} - 1\right)^{-1}\dfrac{\sigma_{YS}}{E}$	(19) $m \ln\left(1 + \dfrac{t_H}{t_L}\right)$ $G(N) \equiv Y = \dfrac{\dot{\epsilon}_p/f - \Delta\bar{\epsilon}_2 + 2\bar{\sigma}_{2A}/E}{\Delta\bar{\epsilon}_2 + \left[\sigma_{YS}/2E - \dfrac{R}{1-R}\Delta\bar{\epsilon}_2\right]}$ $(>0$ only$)$
(17) $G_1 = \left[\epsilon_{K1}\left(\dfrac{\bar{\theta}_{p1}}{\bar{\sigma}_1} - \dfrac{\sqrt{3}}{2}\right)\right]^{-1}$	(20) Plot Y vs $\Delta\epsilon_{K2}$, from eq. (9) above for $\dot{\epsilon}_p/f = 2^M \cdot 10$ $\quad -10 \leq M \leq 4$
(18) Plot G_1 vs ϵ_{K1} on log scale	

Steps 15) - 18) pertain to calculation of G_1 and triaxially augmented ε_{K1}. Since it is not to be added to that from another data set, we simply compute and plot these at the measured-data strain stations. The strain ε_{1K} at which G_1 goes to infinity should correspond to K_{Ic} in the data match.

Steps 19) and 20) detail computation of the strain rate maps. For this paper, strain rate maps were plotted manually, although as time permits we will computerize these as well. Our maps were computed only for the cases R = 0 and R > 0.33 to obviate the task of producing a different map for each R level when R < 0.33. Once automated, strain rate maps should be paired to the G (N) maps in a single computer run for the exact value of R.

12. "DE-LUDERIZATION" PROCEDURE

In this model, any tensile strain hardening rate less than zero, or true rate less than $\bar{\sigma}$, signals an infinite growth rate factor. This occurs ostensibly around the yield point of lower strength steels, where it is associated with the upper yield point and "delayed yield" phenomenon. In Bucci's stress-corrosion cracking data of a highly tempered 4340 steel [32], the trend in growth rate, an early peak corresponding to the lower yield or Luder's strain, was observed. However, we have not seen this effect in corrosion fatigue data on it and other softer steels. We have not, in fact, been able to reproduce the Bucci observation in SCC. However, in the transitional state associated with $G_{2/1}$, it is likely that the upper yield effect would be erased or "unlocked" by the cyclic exercise of the material. The lower yield plateau is diminished by the proliferation of multiple simultaneous bands [33] which such exercise would promote. Accordingly we assume that it is absent in the crack tip ligament. To remove it from the measured curve we follow a procedure used by Holloman [34]. A plot is made of the log of true stress vs strain values from the data sets. A straight line is fitted through the points beyond the Lüder's band region, with slope measured to determine n, the strain hardening exponent. We measure the stress $\bar{\sigma}_o$ at $\bar{\varepsilon}_o$ = 4% strain. Then other stresses $\bar{\sigma}$ can be computed at arbitrary strain $\bar{\varepsilon}$ from

$$\bar{\sigma} = \sigma_0 \left(\frac{\bar{\varepsilon}}{\bar{\varepsilon}_0}\right)^n \tag{87}$$

and by differentiating Eq. (87) the true strain hardening

$$\bar{\theta}_1 = \frac{n\bar{\sigma}_0}{\bar{\varepsilon}} \left(\frac{\bar{\varepsilon}}{\bar{\varepsilon}_0}\right)^{n-1} \tag{88}$$

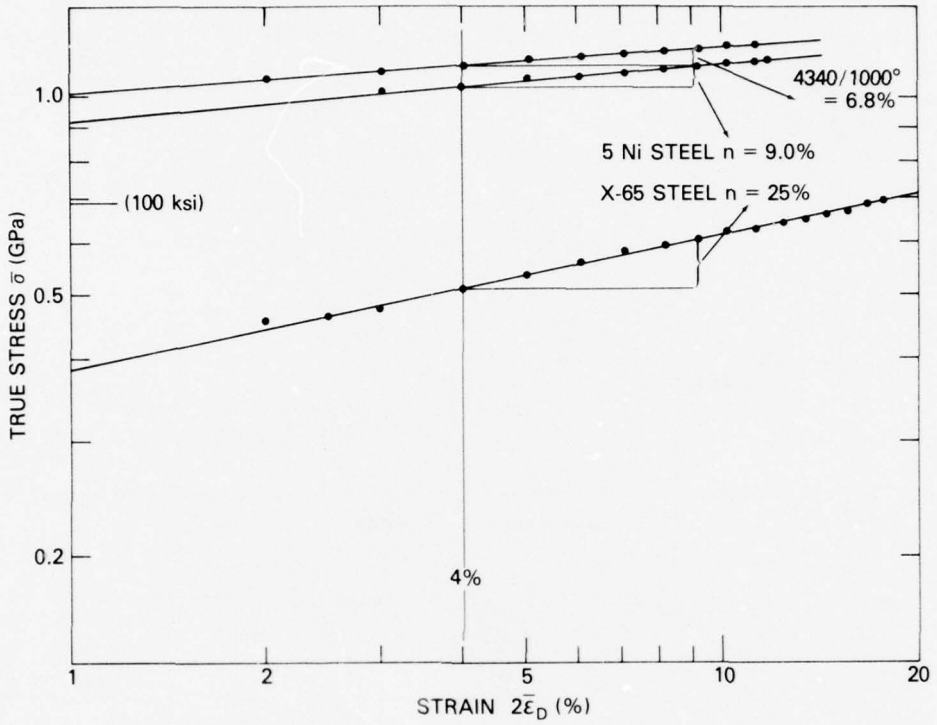

Fig. 3 — A straight line fit of a logarithmic plot of true stress vs strain, of slope n, provides an equation for use in the Lüder band region of the medium strength steels of this study

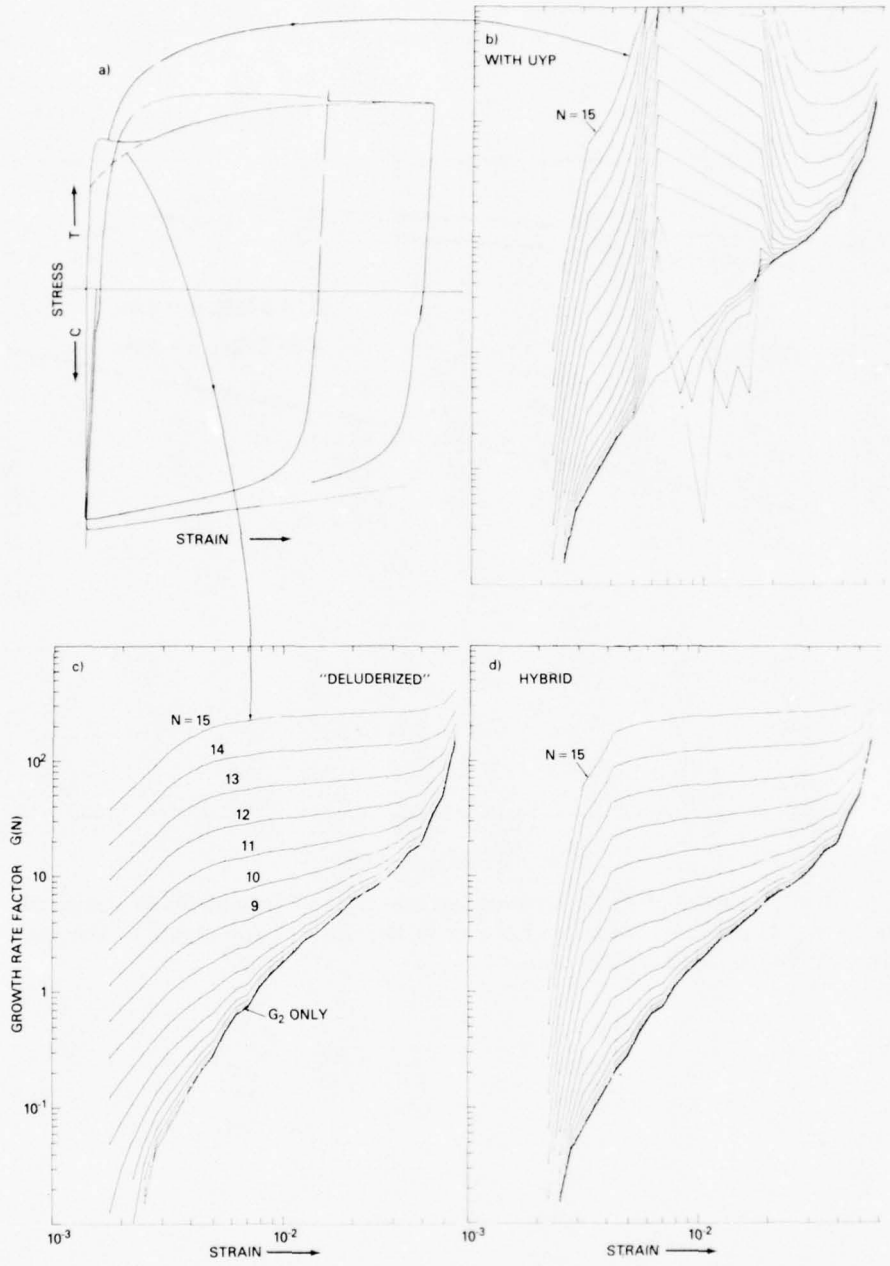

Fig. 4 — The "de-Lüderization" procedure includes (a) stress-strain curve for X-65 steel with upper yield point in first (quarter) cycle; which (b) converted directly to growth rate factor maps shows singularity; while (c) converted via equation from Fig. 3 is continuous; whence (d) combined front from (b) and rear from (c) provides G(N) map used

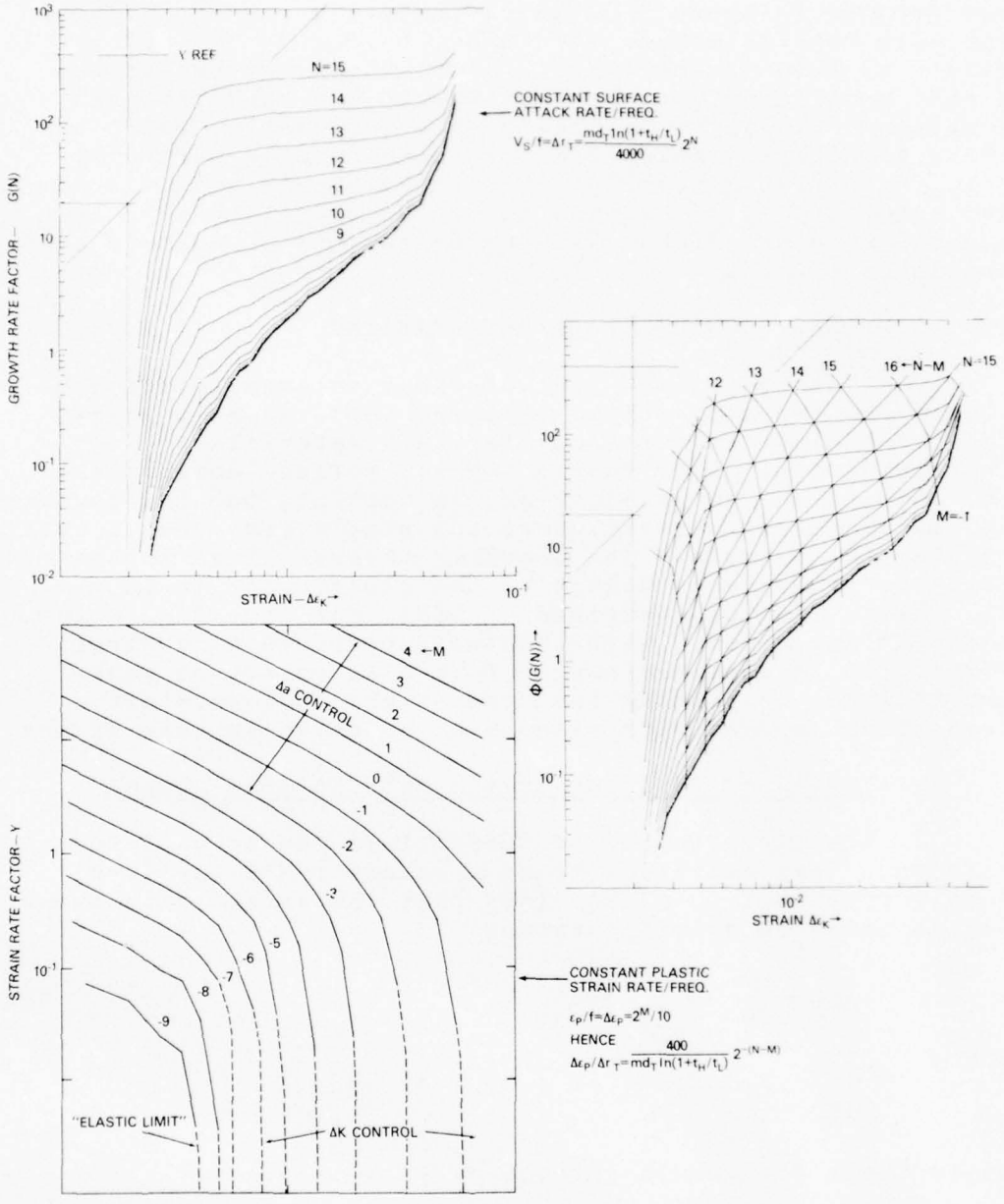

Fig. 5 — Combined growth and strain rate maps for X-65 steel: (a) Growth Rate Factor, N-map, from Fig. 4, (b) parametric set of lines of constant plastic strain rate, M map, in coordinates of (a), superposed in (c), whence segmented curves of constant strain rate/surface attack rate N-M map are drawn

Plots of this sort are shown in Fig. 3 for the three steels of the present study, in order of decreasing strength: 4340 steel tempered at 1000°F; 5Ni steel; and X-65 line-pipe carbon steel. The resulting G(N) parametric curve set for X-65 is shown in Fig. 4, comparing the "unretouched" set with that from Eqs. (87) and (88) for an n = 0.25. The result of this is the "hybrid" set, the front end of the normal plot joined to the back end of the constitutive equation map. It is fortunate that for steels, which are prone to delayed yield effects, the parabolic hardening rule, Eq. (87), generally fits rather nicely and indeed the two sets of G(N) curves superpose closely beyond the Lüder's strain region. "N" values for the parametric curves are noted thereon.

13. COMBINED GROWTH/STRAIN RATE MAPPING

The "de-Lüderized" X-65 provides an example for combining the two maps. Fig. 5, lower left, shows a parametric strain rate curve set for this material. The lines of -1 slope toward the top reflect dominance of strain rate due to propagation, Δa control, turning downward at low propagation rates where the strain rate due to crack loading ΔK controls. The crowding of these lines to the right is produced by deducting the elastic strain in Eq. (64). The "de-Lüderized" G(N) map from Fig. 4 is shown at upper left, with the two superposed at central right. It is possible now to form a third set of parametric lines by joining the upper-right to lower-left trapezoidal apexes with diagonals, as shown in this figure.

A. Curves of Constant Strain Rate/Surface Attack

The significance of these lines can be explained as follows. They represent lines of constant M-N (or -(N-M)). Recall from Sec. 9. A. Eq. (68) that the strain rate parametric lines represent constant

$$\Delta\bar{\epsilon}_p = \frac{2^M}{10} \tag{89}$$

where

$$\Delta\bar{\epsilon}_p = \frac{\dot{\epsilon}_p}{f}$$

while those for growth rate, Sec. 8. A., Eq. (61)

$$\frac{8\Delta r_T}{2m\, d_T\, \ell n \left(1 + \frac{t_H}{t_L}\right)} = 2^N \times 10^{-3} \tag{90}$$

Dividing (89) by (90), and rearranging

$$\frac{\Delta\bar{\epsilon}_p}{\Delta r_T} = \frac{\dot{\bar{\epsilon}}_p}{V_s} = \frac{400}{m\, d_T\, \ell n \left(1 + \frac{t_H}{t_L}\right)}\, 2^{M-N} \qquad (91)$$

This means then, that lines of constant M-N are of constant plastic strain increment relative to the surface annihilation increment, or alternatively, of constant plastic strain rate relative to surface annihilation rate. These two manners of description are thought to be relevant to the two frequency-independent loci of CFCP data, respectively: of the air growth curve; and of the onset of Stage II CF augmentation with respect to frequency. Discussion on this point will follow the case studies.

14. PROCEDURE FOR COMPARING MAPS TO DATA

Several sets of CFCP data will now be compared to the model predictions. In each case data sheet provides a tabulation from ordinary and cyclic stress-strain curves. The data has been processed to obtain true longitudinal values to facilitate comparison with data by non-diametral strain measurements, which are the more customary (and in fact to be preferred). Other necessary and/or useful information on the material is also tabulated. The figures are arranged to show the combined parametric curves of the N series, M series, and N-M series for each R-level on the left. Then the nearest fitting in N, and N-M curves are draw on the CFCP data to the right. Functional values estimated to best fit the data are recorded on the data sheet as part of the results, which includes also the value of d_T at the match position. The characterizing indexes are reduced: N value to Δr_T and N-M to $\Delta\epsilon_p/\Delta r_T$ using Eqs. (90) and (91) respectively.

15. MODEL ORGANIZATION FOR TITANIUM-6Al-4V

This alloy has received much CFCP evaluation because of its extensive utilization in aerospace applications, with attendant concern for environmental degradation. Thus we have a variety of results to model.

A. Irving and Beevers, Vacuum, R-effects, Fig. 6

Irving and Beevers [10] compared CFCP data for a mill-annealed product and two special heat treatments. The martensitic condition, quenched and tempered, is only slightly harder than the mill-annealed material from Fitzgerald and Wei used for our tensile data. The correlation of $G_2(R)$ vs $\Delta\epsilon_K$ plots for their R-levels 0.12, 0.35, 0.61 is fairly satisfactory, and their observed R-insensitivity

above R = 0.35 indicated. Only the basic $G_2(R)$ plot is shown here since the environmental effect is absent.

B. Fitzgerald and Wei, Air R-effects, Fig. 7.

This data (Ref. 12) was an enigma for the long time in which we sought to match it with constant-N curves. At constant N-M = 9 all principal features seem coherent. G-maps are shown for R-levels covering the range of the data, but to avoid extreme crowding not every one, as indicated on Fig. 6. For the highest load ratio, R = 0.9 the G maps lie at the extreme lower limit of strain rate map definition. Here the parametric curve for an N = - 1.5 seems to fit the data. Accurate prediction in this region requires extreme sensitivity and accuracy in the yield point region of the stress-strain curves, which is lacking in our present experimental technique. Nonetheless, the present prediction in the ΔK_{TH} region is quite encouraging.

C. Pettit, Krupp, Ryder and Hoeppner, Salt Water CFCP, Fig. 8.

Again using the flow data from the Fitzgerald and Wei sample, this data [15] illustrates the leveling of "Stage II" growth with cycle time, well modelled, and a moderately "swept-back" entry profile of onset of Stage II. The crossover of curves in transition from Stage II drops down from one to the other once the $\dot{\varepsilon}_p/V_S$ limit corresponding to N-M = 15 is exceeded. An N-M of +9, the same as with the Wei data on this alloy, appears to fit the air data and establish an lower-bound envelope for the Stage II growth.

16. MODEL ORGANIZATIONS FOR TI-8AL-1MO-1V

The material for our stress-strain curves was obtained from the plate used by Meyn. Bucci's specimens were also from this heat, also provided to him by Meyn.

A. Meyn's Classic Case of CFCP, Fig. 9.

Meyn's work [36] was first to show the now-familiar trend in CFCP behaviors. The Stage II threshold appears to be definied by a constant N-M = 13.5 contour, which differs from the subsequent Bucci result.

B. Bucci R-effects in Argon and Salt Water, Fig. 10.

Bucci's growth rates [14] show an up-trend in Stage II growth plateaus with increasing R, an attribute of the

model. The argon data at both R = 0.05 and 0.50, all that is published, is matched by the same N-M = 10.5, which is the same value as for Meyn's air data. The lateral translation of these curves, vs the tight overlap for the Ti-6Al-4V (Fig. 7) is expected if the N-M for the gaseous-environment effect is high, as appears to be the case here. The onset of Bucci's stage II growth appears unlimited by an N-M contour, matching instead the natural contour of the $\Phi(G(N))$ curve for N ≃ 10.5. This data is extremely critical of model calibration, its digestion providing many insights. The irregular excursion for low M sets of the $\dot{\bar{\epsilon}}_p/f$ maps is attributed to inaccuracy in converting diametral to longitudinal strains in the region around the elastic limit. This is another reason for favoring longitudinal strain measurements for these predictions.

17. MODEL ORGANIZATION FOR ALUMINUM 2219-T851

A. Unangst, Shih and Wei [35], R-effects in Air, Fig. 11.

This is the only aluminum alloy included in the study. It is included to show the one case which we have been unable to model satisfactorily. We have successfully modelled a number of other aluminum alloys. The reason for this exception is unknown to us. The FCP data is curious in that it appears to exhibit no definable stage II region, to connect the FCP data to the $\Delta K \rightarrow K_{Ic}$ region.

18. MODEL ORGANIZATION FOR FERROUS ALLOYS

We reanalyze by the present methodology previously published NRL data of Krafft and Smith [6] on 4340 steel of four tempers. To continue the coverage to lower strengths, CFCP data on a 5Ni steel and carbon steel linepipe have been analyzed.

A. 4340/400°F Temper, CFCP data, Fig. 12.

A satisfactory match, and, for the first time, a rationale for the air data with an N-M = 13 for a lower growth rate limit.

B. 4340/600°F Temper CFCP, Fig. 13.

Here again, a reasonable fit. The 10^{-7} torr data of Gallagher [37], inserted, is not quite as slow as the prediction for this material, although it approaches it.

C. 4340/800°F Temper CFCP, Fig. 14.

Now with air effects less severe, the (N-M = 11.5) air limit is seen to fashion the lower limit curve of frequency dependent "constant-N" growth.

D. 4340/1000°F Temper CFCP, Fig. 15.

With this high degree of tempering, the upper yield point effect is restored. In the analysis it has been removed by the "de-Lüderization" procedure described earlier.

E. CFCP data of Gallagher and Ryder [38] and of Cares and Crooker, [39], on a Steel, Fig. 16.

This material is rather stable in salt water, but apparently somewhat susceptible to excessive cathodic polarization. Because of its low susceptibility, relatively long cycle durations were required to show a measurable effect. "De-Lüderization" was required here.

F. X-65 Line Pipe CFCP Data of Vosikovsky, Fig. 17.

The curves, shown to illustrate the de-Lüderization and strain rate mapping in Figs. 2, 3, and 4 is overlaid Vosikovsky's data [40] in salt water, and in salt water with a closely coupled zinc. In the salt water the match is fairly satisfactory. However, with the zinc coupling, the air-line profile prediction lies at higher growth rates than measured, which then is also higher than the Vosikovsky air data, not shown. Vosikovsky employed a triangular, rather than sinusoidal, loading waveform. If one were to compensate for this by reducing the value of $\ell n(1 + t_H/t_L)$ by a factor of two, the match would be greatly improved. However this step is questionable since FCP data on similar steels using sine wave loading is consistent with the Vosikovsky air data. Also it is difficult to understand how the triangular wave form could have been maintained at the higher loading frequency of the air data. Regarding waveform effects, this model has no explanation for Vosikovsky's observation of reduced CFCP rate with square wave loading. Here a greater value of $\ell n(1 + t_H/t_L)$ would be expected, leading to an increased CFCP rate. Data of Dawson and Pelloux [8] on Ti-6Al-6V-2.5N does indeed show the expected upward trend.

It should be noted here that it is not anticipated that this model, as presently constituted, will be applicable to CFCP in softer alloys. This limitation is associated with greater spacing distances between strength-controlling microconstituents, so that these distances

become comparable to the size of the fracture process zone, d_T. In mild steel, this is associated with control of fracture by properties of the matrix, alpha-ferrite in this case. Since the ferrite is softer and more ductile than the overall material including its strengthening carbides, the fracture resistance tends to be greater than predicted from plastic flow measurements on macro-specimens which reflect the overall rather than matrix properties [41].

This model has been set up with no correction for crack closure effects. It does appear that introducing such an influence could provide a closer fit for the softer steels reported here. This is a matter for further study.

19. SUMMARY GRAPH FOR "ORGANIZED" DATA

It is proposed that a great deal of information about CFCP behaviors can be summarized in a simple, yet highly definitive way once the three modelling parameters are determined. The graph of Δr_T vs cycle time, Fig. 18, shows the degree of frequency-dependent cracking. Generally in materials fatigued at ΔK levels below the K_{Iscc} threshold, the $\Delta r_T/\tau$ curves should eventually level out as $V_S \rightarrow 0$. The X-65 and 5 Ni steel, both of this description, appear to be so leveling. The value of the Δr_T crossover at the one-second cycle ordinate is a measure of V_S, the surface annihilation rate. Cases where V_S has been determined from stress-corrosion cracking measurements can be associated with the one-second crossover point as shown on Fig. 18 for Ti-8-1-1 from Sullivan [42] and for 4340 from Ref. [6]. Values of the size and strain rate/corrosion rate parameters are shown in Table II. It should be possible to reconstruct and extend any of the data sets used here, and presumably others, with these few characterization parameters, plus appropriate stress-strain data.

20. MODEL COMPARISON WITH POOK'S $\Delta K_{TH}(R)$ COLLECTION

There is considerable practical importance to the question of the load ratio effect on the threshold for FCP; in fact there is some question as to whether one exists. The way this model-attempt has evolved would suggest its existence, inasmuch as a truly elastic limit of the material exists. Roughly the model predicts a minimum threshold value proportional to $\sigma_{YS}/2E$ at $R = 1$, this limit due to the centroid neutralization effect. It reaches a value $3\sigma_{YS}/2E$ at $R = 0$ when the elastic yield strain has been added. If the value of d_T is known, the threshold can indeed be directly calculated

MATERIAL: TI - 6AL - 4V (MA)

REFERENCE:
A. PETTIT EL AL, REF 15, FIG. 8
B. FITZGERALD AND WEI, REF 12, FIG. 7
C. IRVING AND BEEVERS, REF 10, FIG. 6

NOMINAL CHEMISTRY WT. PCT. (FROM REF 52)

AL	5.50 - 6.75	C	TO	0.1	TI BALANCE
V	3.50 - 4.50	N	TO	0.05	
FE	TO 0.30	H	TO	0.0125	
O	TO 0.20	OTHERS	TOTAL	<0.40	

MECHANICAL PROPERTIES

σ_{YS} = 916 KPA = 133 KSI

σ_{TUS} = 985 KPA = 143 KSI

σ_{CUS} = -1268 KPA = - 184 KSI

ε_U = .075

E = 110.2 MPA = 16000 KSI

θ_{10} = -316.9 MPA = -46000 KSI

θ_{20} = -328.0 MPA = -47600 KSI

M = 0.0136

FIRST EXCURSION DATA

N	STRAIN	STRESS (MPA)	STRESS (KSI)	THETA (MPA)	THETA (KSI)
1	0.000	0	0.0	159000	23000
2	0.002	227	33.0	159000	23000
3	0.005	532	77.3	159000	23000
4	0.008	810	117.6	128000	19000
5	0.010	937	136.0	25300	3700
6	0.012	959	139.3	9960	1450
7	0.014	975	141.6	5060	740
8	0.018	989	143.6	2380	350
9	0.023	1001	145.4	1910	280
10	0.033	1015	147.4	1650	240
11	0.043	1029	149.4	1590	230
12	0.054	1047	152.0	1580	230
13	0.064	1061	154.1	1490	220
14	0.074	1076	156.2	1260	180
15	0.085	1087	157.9	1100	160
16	0.095	1095	159.0	951	138
17	0.106	1103	160.1	813	118

FULL-CYCLIC EXCURSION DATA

N	STRAIN	STRESS (MPA)	STRESS (KSI)	THETA (MPA)	THETA (KSI)
1	-0.012	-1267	-184.0	164000	24000
2	-0.001	-973	-141.3	164000	24000
3	0.002	-657	-95.4	164000	24000
4	0.005	-360	-52.3	148000	22000
5	0.008	-138	-20.2	122000	18000
6	0.009	0	0.0	104000	15000
7	0.011	97	14.1	101000	15000
8	0.012	188	27.3	90300	13100
9	0.013	292	42.5	86900	12600
10	0.014	356	51.7	72500	10500
11	0.016	426	61.9	66300	9600
12	0.017	489	71.1	57400	8300
13	0.018	549	79.8	50600	7300
14	0.019	595	86.5	40900	5900
15	0.021	677	98.4	35500	5100
16	0.024	739	107.3	30300	4400
17	0.026	796	115.7	22500	3300
18	0.028	833	121.0	17700	2600
19	0.030	874	126.9	15500	2300
20	0.032	897	130.3	12800	1900
21	0.037	948	137.7	8380	1220
22	0.042	978	142.0	5690	830
23	0.048	1005	145.9	3960	550
24	0.053	1024	148.7	3000	440
25	0.063	1046	151.9	1900	280
26	0.074	1060	154.0	1420	210
27	0.084	1071	155.6	1110	160

GRAPHICAL REFERENCE POINTS

$GRF|_{REF}$ = $10^{0.958}$ = 10.78

$\Delta\varepsilon_K|_{REF}$ = $10^{-2.468}$ = .003403

$Y|_{REF}$ = $10^{2.259}$ = 181.3

RESULTS

ENV	FREQ (HZ)	R	N	Δr_T (nm)	N-M	$\Delta\varepsilon_p/\Delta r_T$ $(\mu m)^{-1}$	d_γ (nm)
A	10	0.1	1		9	39.4	6.3
SW	10	0.1	9	4.45	15	.351	
SW	1.0	0.1	11.5	25.2			
SW	0.1	0.1	14	142.			

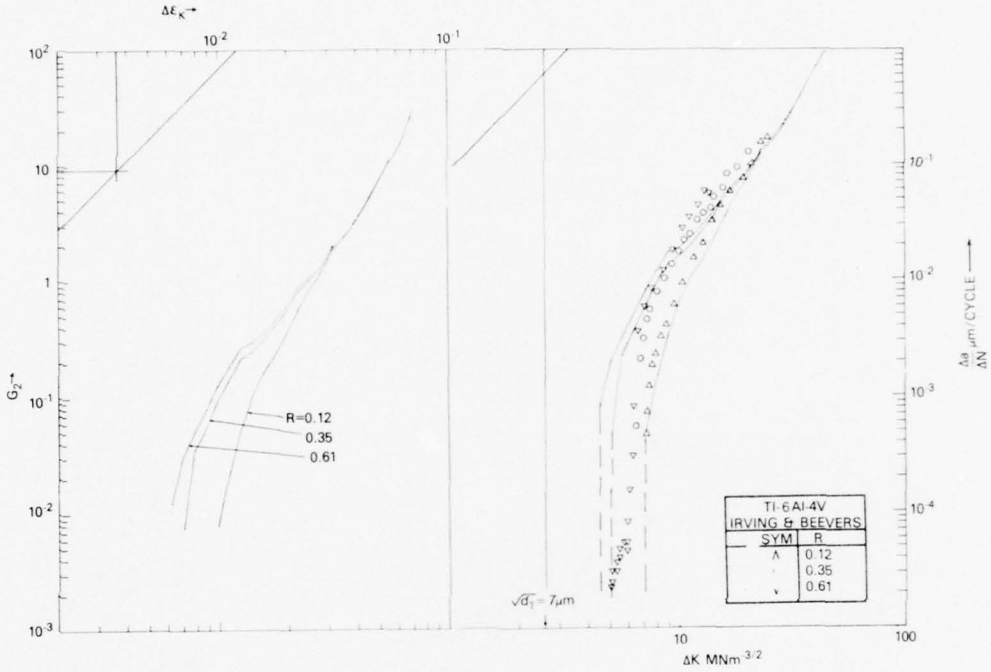

Fig. 6 — The minor effect of load ratio R on FCP rate in vacuum is compared to the m-induced G_2 growth prediction of the present scheme for the Ti-6Al-4V noted

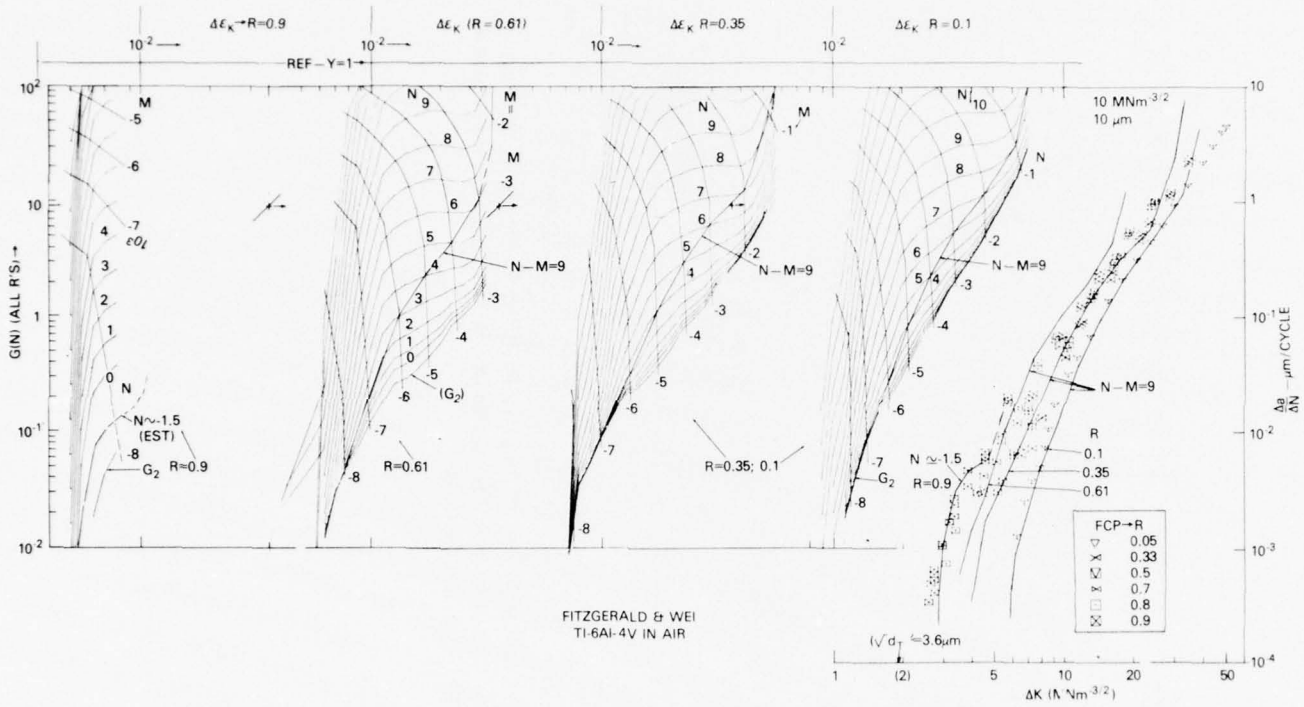

Fig. 7 — When exercised in air, FCP rates of Ti-6Al-4V are markedly increased and the ΔK-threshold decreased with R; the growth pattern is matched by curves of constant ratio of total plastic strain $\Delta\epsilon_p$ to surface attack Δr_T in each load cycle, N-M = 9 set. At the highest R, these curves are poorly defined by a line of constant growth rate factor, $N \simeq -1.5$ matches here. Note that pertinent data on this and other case studies is given in tables identified with figure numbers.

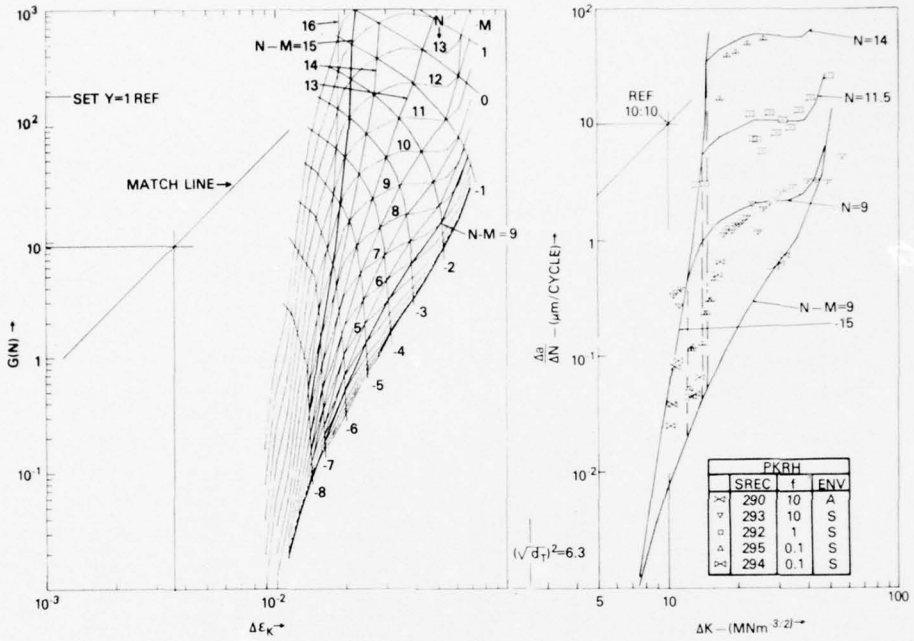

Fig. 8 — Salt-water CFCP data of Pettit et al for a Ti-6Al-4V is bounded by frequency independent $\Delta\bar{\epsilon}_p/\Delta r_T$ lines of N-M indices shown for Stage II onset as an upper limit of growth rate (N-M $\simeq$ 15) and air environment as a lower limit (N-M = 9 as in Fig. 7 results) whereas crossover is at constant Δr_T for the cycle (N set).

MATERIAL: TI - 8AL - 1MO - 1V (MA)

REFERENCE: A. BUCCI, REF 14, FIG. 10
B. MEYN, REF 36, FIG. 9

NOMINAL CHEMISTRY WT. PCT. (FROM REF 36)

AL	7.4	C	0.08	TI	BALANCE
MO	1.16	N	0.004		
V	0.86	O	0.086		
FE	0.14	H	40 PPM		

MECHANICAL PROPERTIES

σ_{YS} = 875 KPA = 127 KSI

σ_{TUS} = 1006 KPA = 146 KSI

σ_{CUS} = -1171 KPA = -170 KSI

ϵ_U = 0.11

E = 127.5 MPA = 18500 KSI

σ_{10} = -399.6 MPA = -58000 KSI

σ_{20} = -385.8 MPA = -56000 KSI

M = 0.012

FIRST EXCURSION DATA

N	STRAIN	STRESS (MPA)	STRESS (KSI)	THETA (MPA)	THETA (KSI)
1	0.000	0	0.0	200000	29000
2	0.003	441	64.1	200000	29000
3	0.005	663	96.3	194000	28000
4	0.006	774	112.4	97400	14100
5	0.007	837	121.6	56100	8100
6	0.009	880	127.8	34700	5000
7	0.011	923	134.1	15400	2200
8	0.013	953	138.4	9470	1370
9	0.015	962	139.7	4220	610
10	0.018	972	141.1	2990	430
11	0.023	984	142.8	2360	340
12	0.033	1001	145.3	1910	280
13	0.043	1018	147.9	1790	260
14	0.054	1036	150.4	1740	250
15	0.064	1054	153.0	1690	250
16	0.074	1072	155.7	1570	230
17	0.085	1091	158.4	1520	220
18	0.095	1102	160.1	1460	210

FULL-CYCLIC EXCURSION DATA

N	STRAIN	STRESS (MPA)	STRESS (KSI)	THETA (MPA)	THETA (KSI)
1	-0.009	-1171	-170.0	193000	28000
2	-0.002	-951	-138.1	193000	28000
3	-0.000	-780	-113.2	193000	28000
4	0.001	-601	-87.3	193000	28000
5	0.003	-394	-57.2	186000	27000
6	0.004	-242	-35.2	155000	23000
7	0.006	-103	-15.1	150000	22000
8	0.007	41	6.0	145000	21000
9	0.008	180	26.2	130000	19000
10	0.011	389	56.6	91800	13300
11	0.013	523	75.9	57400	8300
12	0.016	621	90.3	49200	7100
13	0.018	700	101.6	32000	4600
14	0.022	829	120.4	23800	3500
15	0.026	925	134.3	13400	1900
16	0.033	979	142.2	8810	1280
17	0.038	1020	148.1	6630	960
18	0.043	1047	152.0	4070	590
19	0.053	1072	155.7	2560	370
20	0.064	1098	159.4	1670	240
21	0.074	1117	162.2	1220	180
22	0.085	1121	162.8	978	142

GRAPHICAL REFERENCE POINTS

$GRF|_{REF} = 10^{1.012} = 10.28$

$\Delta\epsilon_K|_{REF} = 10^{-2.505} = .003127$

$Y|_{REF} = 10^{2.313} = 205$

RESULTS

ENV	FREQ (HZ)	R	N	Δr_T (nm)	N-M	$\Delta\epsilon_p/\Delta r_T$ $(\mu m)^{-1}$	θ_T (um)
IA	5	.05	6		10.5	4.73	10.0
IA	5	.5					
SW	5	.05	10.5	21.1	10.5	4.73	
SW	5	.5	10.5	21.1			
SW	5	.75	10.5	21.1			
V	10-30	0					
A	10-30	0			10.5	3.68	12.0
SW	10-30	0	7.5	2.20	13.5	.710	
SW	2	0	11	24.9			
SW	0.5	0	13	99.6			

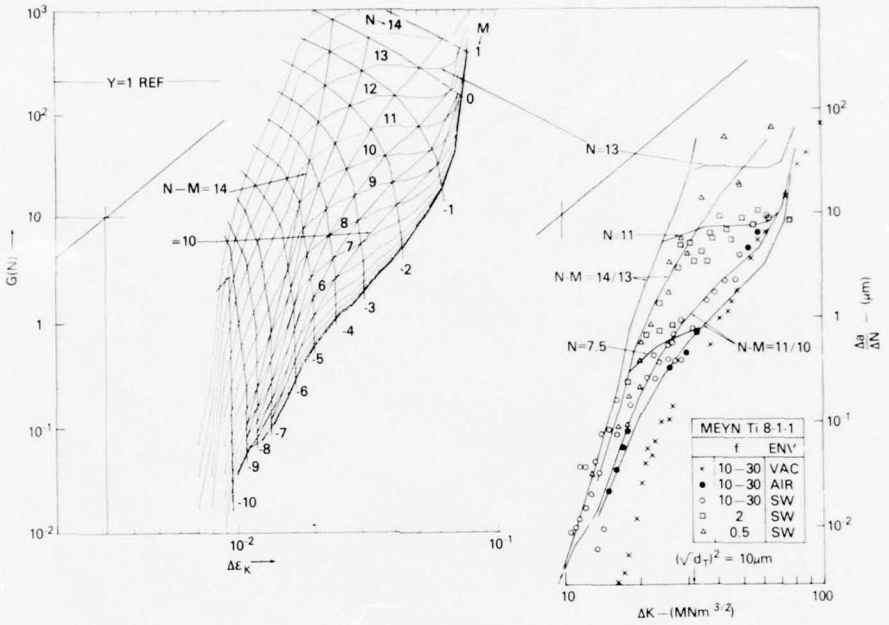

Fig. 9 — Salt water CFCP data of Meyn for a Ti-8Al-1Mo-1V is bounded in the manner of Fig. 8. The lower bound G_2-only curve of the predictive map is of the same trend as Meyn's FCP rate in vacuum but fails to anticipate the trend at low growth ΔK levels.

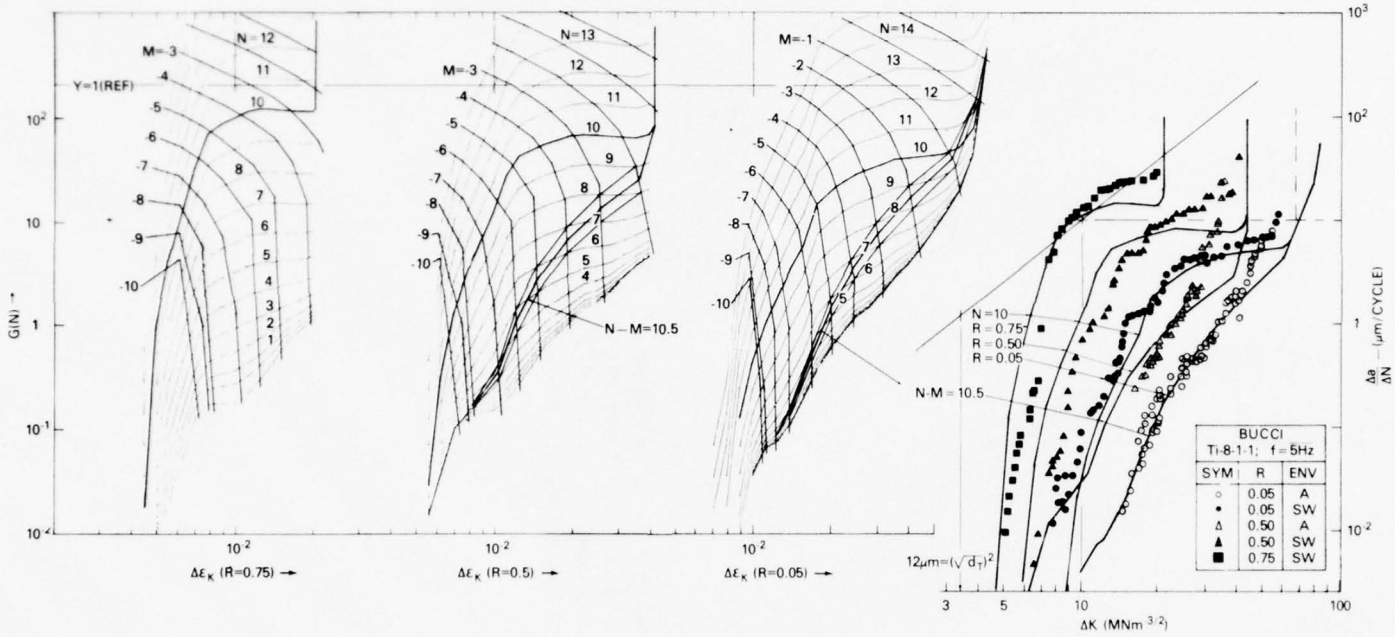

Fig. 10 — Dry argon and salt water FCP data of Bucci for the Ti-8Al-1Mo-1V of Meyn shows the argon data fitted by about the same $\Delta\bar{\epsilon}_p/\Delta r_T$ (N-M $\simeq$ 10.5) as the air-environment data of Meyn. The salt water CFCP trends are fitted by constant Δr_T per cycle, N $\simeq$ 10, for all thru R levels with no apparent $\Delta\bar{\epsilon}_p/\Delta r_T$ upper limit.

Preceding Page BLANK - NOT FILMED

MATERIAL: 2219-T851 ALUMINUM ALLOY

REFERENCE: UNANGST AND WEI, REF 35, FIG. 11

NOMINAL CHEMISTRY WT. PCT. (FROM REF 52)

CU	5.8 - 6.8	TI	0.02 - 0.10
MG	TO 0.02	ZN	TO 0.10
MN	0.20 - 0.40	OTHER	TO 0.05, TOTAL
PE	TO 0.30	AL	BALANCE
SI	TO 0.20		

MECHANICAL PROPERTIES

σ_{YS} = 369 KPA = 53.5 KSI

σ_{TUS} = -

σ_{CUS} = -455 KPA = -60 KSI

σ_U =

= 73.0 MPA = 10600 KSI

θ_{10} = -215.0 MPA = -31200 KSI

θ_{20} = -162.6 MPA = -23600 KSI

M = 0.0081

FIRST EXCURSION DATA

N	STRAIN	STRESS (MPA)	STRESS (KSI)	THETA (MPA)	THETA (KSI)
1	0.000	0	0.0	108000	16000
2	0.002	113	16.5	108000	16000
3	0.003	220	32.1	108000	16000
4	0.004	304	44.1	74100	10800
5	0.006	349	50.7	21100	3100
6	0.007	361	52.5	8510	1240
7	0.008	368	53.4	5830	850
8	0.010	379	55.1	4050	590
9	0.012	384	55.8	3640	530
10	0.017	402	58.5	3250	470
11	0.022	420	61.0	3130	450
12	0.027	432	62.8	2940	430
13	0.032	447	64.9	2410	350
14	0.042	467	67.8	1860	270
15	0.053	483	70.2	1350	200
16	0.063	492	71.5	919	133
17	0.065	494	71.8	836	121

FULL-CYCLIC EXCURSION DATA

N	STRAIN	STRESS (MPA)	STRESS (KSI)	THETA (MPA)	THETA (KSI)
1	-0.006	-461	-67.0	80800	11700
2	0.000	-379	-55.1	78900	11500
3	0.002	-296	-43.1	79000	11500
4	0.003	-231	-33.6	79100	11500
5	0.004	-166	-24.1	79200	11500
6	0.005	-76	-11.1	79400	11500
7	0.006	-6	-1.0	79500	11500
8	0.006	0	0.0	79500	11500
9	0.007	52	7.6	72700	10500
10	0.008	104	15.1	61700	9000
11	0.010	196	28.5	33400	4900
12	0.012	245	35.6	20300	3000
13	0.014	279	40.6	15200	2200
14	0.016	301	43.7	10500	1500
15	0.019	321	46.6	8590	1250
16	0.021	336	48.9	7300	1060
17	0.024	365	53.1	5600	810
18	0.031	391	56.8	4450	650
19	0.036	412	59.9	3850	560
20	0.041	430	62.5	3170	460
21	0.046	445	64.7	2910	420
22	0.051	456	66.3	2470	360
23	0.056	469	68.2	2030	290
24	0.062	477	69.3	1760	250
25	0.067	485	70.5	1340	190
26	0.072	490	71.2	990	144
27	0.074	493	71.6	936	136

GRAPHICAL REFERENCE POINTS

$GRF|_{REF} = 10^{1.183} = 15.22$

$\Delta\varepsilon_K|_{REF} = 10^{-2.763} = 0.00546$

$Y|_{REF} = 10^{2.483} = 304.4$

RESULTS

a_T = 16 μm

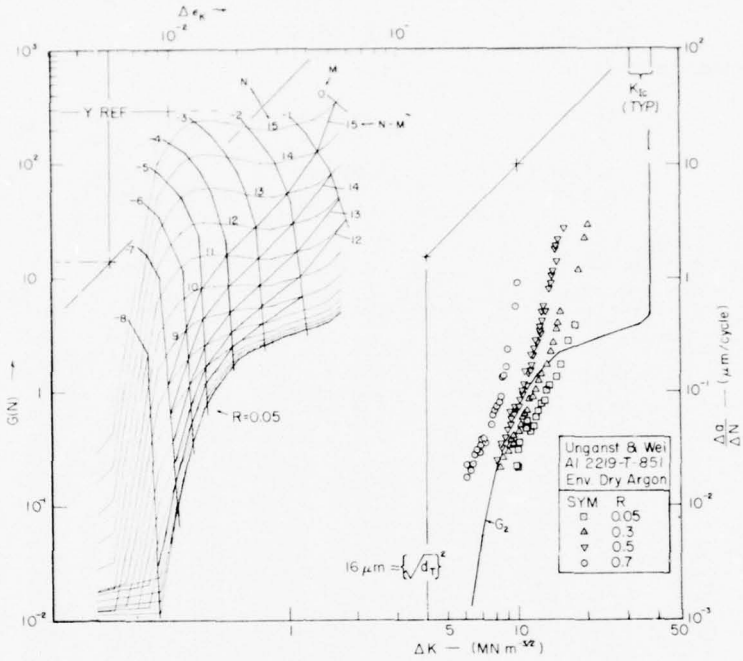

Fig. 11 — Dry argon FCP data of Unangst and Wei is poorly matched by G_2 curves, a failure unexpected in view of accurate model predictions of FCP for many other aluminum alloys

MATERIAL: 4340 STEEL (QUENCHED AND TEMPERED AT 400°F)

REFERENCE: KRAFFT AND SMITH, REF 6, FIG. 12

NOMINAL CHEMISTRY WT. PCT. (FROM REF 6)

C	0.40	S	0.02	FE	BALANCE
MN	0.72	CR	0.82		
SI	0.31	NI	1.85		
P	0.01	MO	0.22		

MECHANICAL PROPERTIES

σ_{YS} = 148.8 KPA = 216 KSI

σ_{TUS} = 188.1 KPA = 273 KSI

σ_{CUS} = -213.6 KPA = -310 KSI

ν = 0.11

E = 206.7 MPA = 30000 KSI

σ_{10} = -613.2 MPA = -89000 KSI

σ_{20} = -592.5 MPA = -86000 KSI

M = 0.0065

FIRST EXCURSION DATA

N	STRAIN	STRESS (MPA)	STRESS (KSI)	THETA (MPA)	THETA (KSI)
1	0.000	0	0.0	307000	45000
2	0.003	655	95.9	306000	44000
3	0.005	988	143.4	284000	41000
4	0.006	1217	176.7	215000	31000
5	0.007	1357	197.0	115000	17000
6	0.008	1469	213.3	76800	11100
7	0.010	1562	226.8	42400	6200
8	0.013	1628	236.4	32100	4700
9	0.015	1680	243.9	18300	2700
10	0.017	1718	249.5	15600	2300
11	0.019	1750	254.0	14900	2200
12	0.023	1799	261.2	10500	1500
13	0.027	1842	267.4	8610	1250
14	0.031	1870	271.6	7040	1020
15	0.035	1899	275.8	5820	840
16	0.039	1921	279.0	5220	760
17	0.043	1944	282.2	3980	580
18	0.049	1961	284.7	3510	510
19	0.054	1971	286.1	3240	470
20	0.064	1999	290.1	2640	380
21	0.074	2019	293.2	2090	300
22	0.085	2040	296.2	1610	230
23	0.095	2054	298.2	1410	200
24	0.105	2066	300.0	1200	170

FULL-CYCLIC EXCURSION DATA

N	STRAIN	STRESS (MPA)	STRESS (KSI)	THETA (MPA)	THETA (KSI)
1	-0.010	-2135	-310.0	296000	43000
2	0.000	-1242	-180.4	296000	43000
3	0.002	-932	-135.4	296000	43000
4	0.003	-615	-89.4	289000	42000
5	0.004	-401	-58.3	266000	39000
6	0.006	-110	-16.1	231000	34000
7	0.007	0	0.0	214000	31000
8	0.008	208	30.2	210000	30000
9	0.009	403	58.5	173000	25000
10	0.010	570	82.8	125000	18000
11	0.012	668	97.0	115000	17000
12	0.013	766	111.3	101000	15000
13	0.014	851	123.5	84100	12200
14	0.016	992	144.1	66900	9700
15	0.018	1106	160.6	50400	7300
16	0.020	1200	174.2	40800	5900
17	0.025	1353	196.4	32000	4600
18	0.029	1457	211.6	23800	3500
19	0.033	1548	224.8	19100	2800
20	[illegible]	1626	236.1	17800	2600
21	0.043	1703	247.4	11700	1700
22	0.050	1776	257.9	9110	1320
23	0.055	1822	264.4	7760	1130
24	0.060	1860	270.0	6400	930
25	0.070	1916	278.2	5050	730
26	0.081	1951	283.3	4390	640
27	0.091	1979	287.3	2840	410
28	0.102	2015	292.6	2670	390
29	0.113	2038	295.8	2330	340
30	0.124	2059	299.0	2060	300
31	0.134	2066	299.9	1260	180

GRAPHICAL REFERENCE POINTS:

$GRF|_{REF} = 10^{1.278} = 18.97$

$\Delta K|_{REF} = 10^{-2.715} = 0.001928$

$Y|_{REF} = 10^{2.579} = 379.4$

RESULTS

ENV	FREQ (HZ)	R	N	Δr_T (nm)	N-M	$\Delta K_P/\Delta r_T$ $(\mu m)^{-1}$	d_T (nm)
A	10	0.1			13.5	4.23	3.1
FW	10	0.1	11	4.18	18.5	.0939	
FW	4	0	12.3	10.3			
FW	2	0	13.3	20.6			
FW	1	0	14.3	41.2			
FW	0.5	0	15.3	82.4			

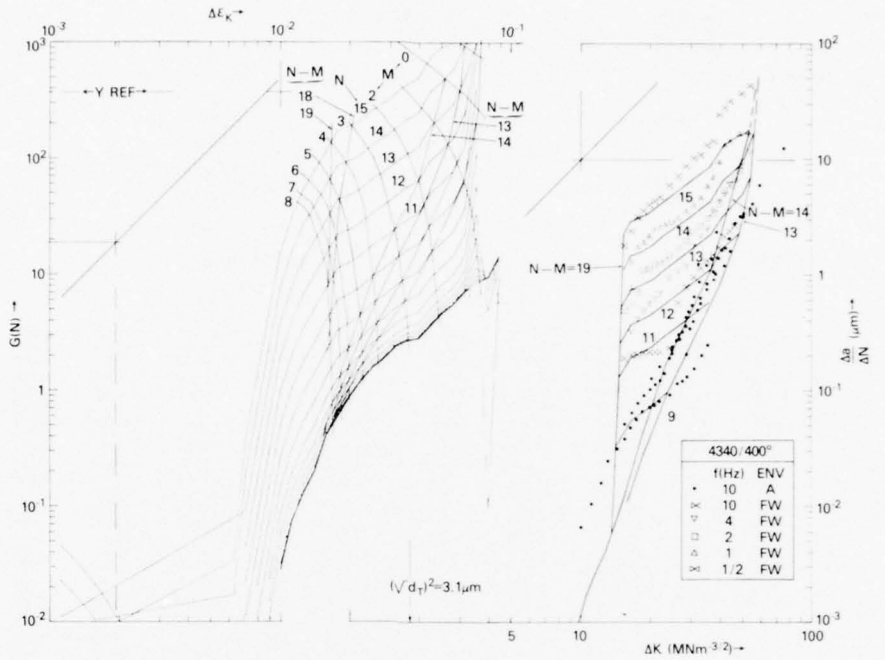

Fig. 12 — Fresh (distilled) water and air data of NRL on 4340 steel of four tempers is shown in the next four figures. Here the hardest condition, 205°C tempering, appears nicely bounded N-M = 19 for upper frequency-independent limit, 13.5 for the lower one, with various constant-N lines fitting stage II data in transition there.

MATERIAL: 4340 STEEL (QUENCHED AND TEMPERED AT 600°F)

REFERENCE: J.M. KRAFFT AND H.L. SMITH REF 6, FIG. 13

NOMINAL CHEMISTRY WT. PCT. (FROM REF 6)

C	0.40	S	0.02	FE BALANCE
MN	0.72	CR	0.82	
SI	0.31	NI	1.85	
P	0.01	MO	0.22	

MECHANICAL PROPERTIES

σ_{YS} = 1406 KPA = 204 KSI

σ_{TUS} = 1605 KPA = 233 KSI

σ_{CUS} = -1619 KPA = -235 KSI

ϵ_U = 0.015

E = 206.7 MPA = 30000 KSI

σ_{10} = -654.6 MPA = -95000 KSI

σ_{20} = -620.1 MPA = -90000 KSI

M = 0.0048

FIRST EXCURSION DATA

N	STRAIN	STRESS (MPA)	STRESS (KSI)	THETA (MPA)	THETA (KSI)
1	0.000	0	0.0	329000	48000
2	0.005	1022	148.4	329000	48000
3	0.006	1328	192.8	177000	26000
4	0.007	1377	200.0	33200	4800
5	0.009	1414	205.2	28000	4100
6	0.011	1465	212.7	28000	4100
7	0.013	1510	219.2	20300	3000
8	0.015	1548	224.7	12900	1900
9	0.017	1565	227.2	10600	1500
10	0.019	1582	229.7	7830	1140
11	0.023	1609	233.6	5790	840
12	0.028	1632	236.9	3590	520
13	0.033	1647	239.1	2910	420
14	0.038	1663	241.4	2220	320
15	0.043	1671	242.6	2230	320
16	0.054	1688	245.1	1550	220
17	0.064	1698	246.6	989	143
18	0.074	1709	248.1	638	93
19	0.085	1712	248.5	348	51

FULL-CYCLIC EXCURSION DATA

N	STRAIN	STRESS (MPA)	STRESS (KSI)	THETA (MPA)	THETA (KSI)
1	-0.008	-1619	-235.0	310000	45000
2	-0.001	-1310	-190.2	310000	45000
3	0.000	-980	-142.3	310000	45000
4	0.002	-691	-100.3	310000	45000
5	0.003	-456	-66.3	310000	45000
6	0.005	-193	-28.1	269000	39000
7	0.006	0	0.0	242000	35000
8	0.007	194	28.2	201000	29000
9	0.009	354	51.4	177000	26000
10	0.010	514	74.7	129000	18000
11	0.011	577	83.8	104000	15000
12	0.012	696	101.1	76900	11200
13	0.013	781	113.4	58300	8500
14	0.015	866	125.8	50800	7400
15	0.018	938	136.2	38400	5600
16	0.020	1010	146.6	31900	4600
17	0.024	1120	162.6	22600	3300
18	0.028	1195	173.5	16100	2300
19	0.032	1242	180.4	11900	1700
20	0.036	1290	187.3	10100	1500
21	0.041	1331	193.3	8280	1200
22	0.045	1365	198.2	7420	1080
23	0.049	1393	202.2	6120	890
24	0.054	1422	206.4	5240	760
25	0.059	1443	209.6	4560	660
26	0.070	1488	216.0	3770	550
27	0.080	1518	220.4	3020	440
28	0.090	1542	223.8	2620	380
29	0.101	1566	227.3	2000	290
30	0.111	1590	230.8	1810	260
31	0.122	1607	233.3	1398	200
32	0.133	1600	232.4	571	83

GRAPHICAL REFERENCE POINTS

$GRF|_{REF} = 10^{1.410} = 25.69$

$\Delta\epsilon_K|_{REF} = 10^{-2.715} = .001928$

$Y|_{REF} = 10^{2.711} = 513.8$

RESULTS

ENV	FREQ (HZ)	R	N	Δr_T (nm)	N-M	$\Delta\epsilon_p/\Delta r_T$ $(\mu m)^{-1}$	β_T (nm)
V	10		7.5				
A	10	0.1	10	4.48	11.5	7.88	
FW	4	0	11.5	12.7	20.5	.0154	
FW	2	0	12.5	25.4			
FW	1	0	13.5	50.7			
FW	0.5	0	14.5	101.			

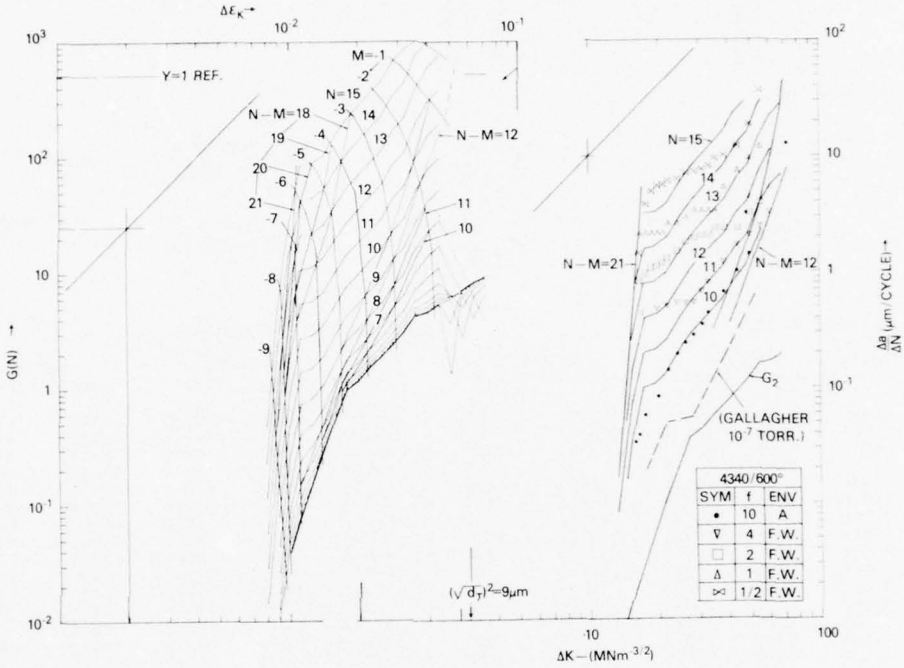

Fig. 13 — G-map vs CFCP data for 4340 steel as in Fig. 12 but for tempering at 315°C. FCP data of Gallagher is much lower than NRL data for air but not quite as low as present prediction for m-induced growth, the G_2-only line.

MATERIAL: 4340 STEEL (QUENCHED AND TEMPERED AT 800°F)

REFERENCE: KRAFFT AND SMITH, REF 6, FIG. 14

NOMINAL CHEMISTRY WT. PCT. (FROM REF 6)

C	0.40	S	0.02	FE	BALANCE
MN	0.72	CR	0.82		
SI	0.31	NI	1.85		
P	0.01	MO	0.22		

MECHANICAL PROPERTIES

σ_{YS} = 1250 KPA = 181 KSI

σ_{TUS} = 1370 KPA = 199 KSI

σ_{CUS} = -1450 KPA = -210 KSI

ϵ_U = 0.11

E = 206.7 MPA = 30000 KSI

θ_{10} = -654.6 MPA = -95000 KSI

θ_{20} = -654.6 MPA = -95000 KSI

M = 0.0059

FIRST EXCURSION DATA

N	STRAIN	STRESS (MPA)	STRESS (KSI)	THETA (MPA)	THETA (KSI)
1	0.000	0	0.0	329000	48000
2	0.005	981	142.4	329000	48000
3	0.006	1210	175.7	73700	10700
4	0.007	1267	183.9	19200	2800
5	0.008	1275	185.1	11200	1600
6	0.010	1291	187.5	10500	1500
7	0.012	1308	189.9	10500	1500
8	0.014	1331	193.3	7360	1070
9	0.016	1348	195.7	5100	740
10	0.019	1358	197.1	4140	600
11	0.023	1370	199.0	3810	550
12	0.028	1377	200.0	3120	450
13	0.033	1398	203.0	2940	430
14	0.038	1413	205.1	1970	290
15	0.043	1420	206.2	1630	240
16	0.053	1442	209.3	1650	240
17	0.064	1457	211.5	1460	210
18	0.074	1464	212.6	894	130
19	0.084	1472	213.8	468	68

FULL-CYCLIC EXCURSION DATA

N	STRAIN	STRESS (MPA)	STRESS (KSI)	THETA (MPA)	THETA (KSI)
1	-0.007	-1378	-200.0	327000	47000
2	-0.001	-965	-140.1	327000	47000
3	0.001	-635	-92.2	327000	47000
4	0.002	-345	-50.2	317000	46000
5	0.004	-117	-17.1	231000	34000
6	0.005	0	0.0	228000	33000
7	0.006	200	29.2	159000	23000
8	0.007	332	48.3	128000	19000
9	0.008	430	62.5	90300	13100
10	0.009	528	76.7	69700	10100
11	0.011	605	87.8	53200	7700
12	0.012	668	97.0	42900	6200
13	0.014	718	104.3	38200	5500
14	0.016	789	114.7	30200	4400
15	0.018	847	123.0	24500	3600
16	0.022	935	135.8	16600	2400
17	0.026	988	143.5	12700	1800
18	0.031	1035	150.3	11000	1600
19	0.035	1075	156.0	8080	1170
20	0.039	1100	159.8	7280	1060
21	0.043	1126	163.6	6120	890
22	0.047	1153	167.4	5590	810
23	0.052	1180	171.4	4930	710
24	0.057	1201	174.4	4180	610
25	0.068	1235	179.4	3510	510
26	0.078	1271	184.5	2850	410
27	0.089	1306	189.7	2600	380
28	0.099	1328	192.8	1980	290
29	0.110	1343	194.9	1630	240
30	0.121	1357	197.0	1360	200
31	0.131	1356	196.8	548	80

GRAPHICAL REFERENCE POINTS

$GRF|_{REF} = 10^{1.320} = 20.90$

$\Delta\epsilon_K|_{REF} = 10^{-2.715} = 0.001928$

$Y|_{REF} = 10^{2.621} = 418.02$

RESULTS

ENV	FREQ (HZ)	R	N	Δr_T (nm)	N-M	$\Delta\epsilon_p/\Delta r_T$ $(\mu m)^{-1}$	d_T (um)
A	10	0.1			11.5	6.41	9.0
A	10	0.5					
FW	2	0	8	1.38	18	.0709	
FW	0.5	0	10	5.51			

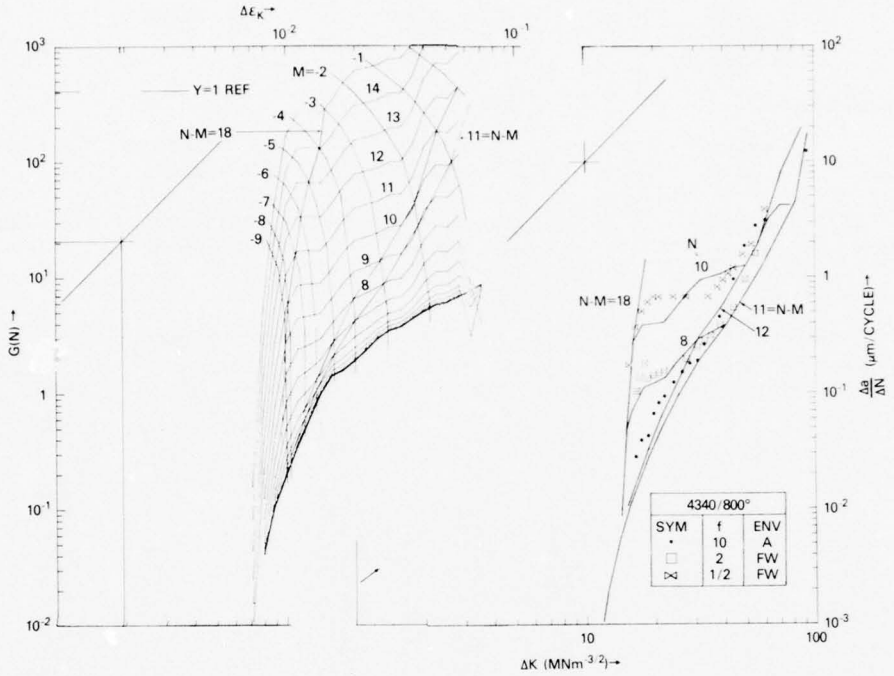

Fig. 14 — G-map vs CFCP data for 4340 steel as in Fig. 12 but for tempering at 427°C. A marked decrease in the level of stage II growth rate is evident here.

MATERIAL: 4340 - 1000°F TEMPER

REFERENCE: KRAFFT AND SMITH, REF 6 , FIG. 15

NOMINAL CHEMISTRY WT. PCT. (FROM REF 6)

C	0.40	S	0.02	FE BALANCE
MN	0.72	CR	0.82	
SI	0.31	NI	1.85	
P	0.01	MO	0.22	

MECHANICAL PROPERTIES

σ_{YS} = 1030 KPA = 150 KSI

σ_{TUS} = 1080 KPA = 157 KSI

σ_{CUS} = -1160 KPA = -168 KSI

ε_U = 0.075

E = 206.7 MPA = 30000 KSI

σ_{10} = -603.6 MPA = -87600 KSI

σ_{20} = -603.6 MPA = -87600 KSI

M = .0066

FIRST EXCURSION DATA

N	STRAIN	STRESS (MPA)	STRESS (KSI)	THETA (MPA)	THETA (KSI)
1	0.000	0	0.0	303000	44000
2	0.003	635	92.2	303000	44000
3	0.004	932	135.4	278000	40000
4	0.005	1023	148.5	45200	6600
5	0.006	1030	149.6	8620	1250
6	0.007	1038	150.8	1310	190
7	0.012	1043	151.5	1320	190
8	0.017	1049	152.3	2440	350
9	0.[illegible]	1068	155.1	3020	440
10	0.032	1093	158.7	2700	390
11	0.042	1119	162.4	2240	330
12	0.052	1137	165.2	1920	280
13	0.063	1149	166.9	1360	200
14	0.073	1161	168.6	1230	180
15	0.083	1173	170.4	1100	160
16	0.094	1178	171.0	890	129
17	0.104	1190	172.9	756	110
18	0.115	1203	174.7	693	101
19	0.126	1208	175.4	549	80

FULL-CYCLIC EXCURSION DATA

N	STRAIN	STRESS (MPA)	STRESS (KSI)	THETA (MPA)	THETA (KSI)
1	-0.006	-1157	-168.0	302000	44000
2	-0.000	-841	-122.1	302000	44000
3	0.001	-538	-78.2	302000	44000
4	0.003	-255	-37.1	252000	37000
5	0.004	-34	-5.0	214000	31000
6	0.004	0	0.0	200000	29000
7	0.006	242	35.2	125000	18000
8	0.008	381	55.4	78500	11400
9	0.009	486	70.6	58600	8500
10	0.011	556	80.8	44200	6400
11	0.013	609	88.5	33700	4900
12	0.014	663	96.3	27900	4100
13	0.017	728	105.7	20900	3000
14	0.020	772	112.1	15300	2200
15	0.024	810	117.6	11300	1600
16	0.027	848	123.1	9430	1370
17	0.030	871	126.5	8070	1170
18	0.033	888	129.0	6770	980
19	0.036	920	133.5	6180	900
20	0.044	962	139.8	5110	740
21	0.051	984	142.9	3670	530
22	0.059	1007	146.2	2780	400
23	0.067	1029	149.4	2450	360
24	0.082	1060	154.0	2130	310
25	0.098	1092	158.6	2000	290
26	0.114	1125	163.4	1850	270
27	0.130	1151	167.1	1510	220

GRAPHICAL REFERENCE POINTS

$GRF|_{REF} = 10^{1.271} = 18.68$

$\Delta\varepsilon_K|_{REF} = 10^{-2.715} = .001928$

$Y|_{REF} = 10^{2.572} = 373.7$

RESULTS

ENV	FREQ (HZ)	R	N	Δr_T (nm)	N-M	$\Delta\varepsilon_p/\Delta r_T$ $(\mu m)^{-1}$	d_T (μm)
A	10	0.1			11.5	5.73	
FW	1	0	8.5	2.18	14	1.01	9.0
FW	0.5	0	8.5				

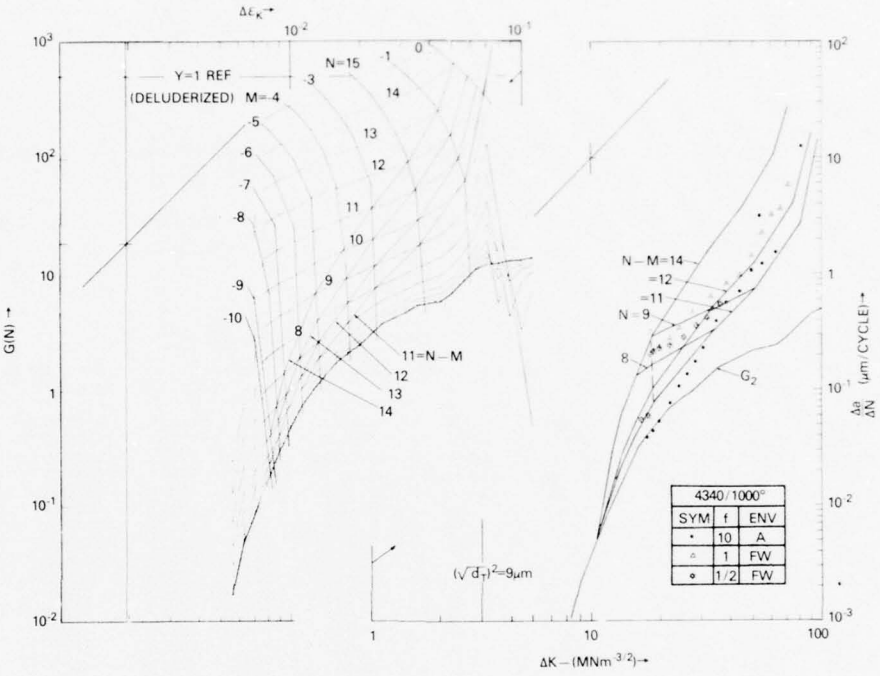

Fig. 15 — G-map vs CFCP data for 4340 steel as in Fig. 12 but for tempering at 538°C. The G-map has been prepared by the "de-Lüderizing" process to remove the upper yield point effect.

MATERIAL: FE - 5NI+ {CR, MO, V}, QUENCHED AND TEMPERED

REFERENCE: A. RYDER AND GALLAGHER, REF 38, FIG. 16
B. CARES AND CROOKER, REF 39, FIG. 16

NOMINAL CHEMISTRY WT. PCT. {FROM REF 38}

NI	4.90	MN	0.80	SI	0.27
CR	0.57	C	0.11	FE	BALANCE
MO	0.50	P	0.014		
V	0.07	S	0.008		

MECHANICAL PROPERTIES

σ_{YS} = 958 KPA = 139 KSI

σ_{TUS} = 1030 KPA = 148 KSI

σ_{CUS} = -1102 KPA = -160 KSI

ϵ_U = 0.08

E = 203.3 MPA = 29500 KSI

σ_{10} = -523.6 MPA = -76000 KSI

σ_{20} = -523.6 MPA = -76000 KSI

M = 0.0077

FIRST EXCURSION DATA

N	STRAIN	STRESS (MPA)	STRESS (KSI)	THETA (MPA)	THETA (KSI)
1	0.000	0	0.0	263000	38000
2	0.001	344	50.1	263000	38000
3	0.003	607	88.2	263000	38000
4	0.004	843	122.4	97400	14100
5	0.005	933	135.5	31300	4500
6	0.006	948	137.7	18200	2600
7	0.007	970	140.8	8090	1170
8	0.009	982	142.6	3890	560
9	0.011	988	143.4	2130	310
10	0.021	1005	145.9	1490	220
11	0.031	1026	148.9	1760	260
12	0.042	1043	151.5	1780	260
13	0.052	1061	154.1	1630	240
14	0.062	1076	156.2	1500	220
15	0.072	1091	158.4	1380	200
16	0.083	1104	160.4	1250	180
17	0.093	1117	162.2	1120	160
18	0.104	1129	163.9	1060	150
19	0.114	1138	165.2	992	144
20	0.120	1140	165.5	921	134

FULL-CYCLIC EXCURSION DATA

N	STRAIN	STRESS (MPA)	STRESS (KSI)	THETA (MPA)	THETA (KSI)
1	-0.005	-1102	-160.0	262000	38000
2	0.000	-737	-107.1	262000	38000
3	0.001	-490	-71.1	262000	38000
4	0.003	-234	-34.1	245000	36000
5	0.004	0	0.0	221000	32000
6	0.005	207	30.1	190000	28000
7	0.006	398	57.8	132000	19000
8	0.008	590	85.7	76700	11100
9	0.011	713	103.5	43600	6300
10	0.013	784	113.8	24300	3500
11	0.015	827	120.1	18200	2600
12	0.020	898	130.4	8860	1290
13	0.025	938	136.2	4840	700
14	0.030	964	140.0	4390	640
15	0.035	987	143.3	3230	470
16	0.045	1011	146.8	2000	290
17	0.056	1029	149.4	1530	220
18	0.066	1043	151.5	1190	170
19	0.076	1056	153.4	1130	160
20	0.087	1069	155.2	1070	160
21	0.097	1079	156.6	1010	150
22	0.108	1090	158.2	1020	150
23	0.119	1100	159.7	987	143

GRAPHICAL REFERENCE POINTS

$GRF|_{REF} = 10^{1.204} = 16.01$

$\Delta\epsilon_K|_{REF} = 10^{-2.708} = .00196$

$Y|_{REF} = 10^{2.506} = 320$

RESULTS

ENV	FREQ {HZ}	R	N	Δr_T {nm}	N-M	$\Delta\epsilon_p/\Delta r_T$ $\{\mu m\}^{-1}$	β_T {μm}
SW	2.5	0	-	-	-	-	17.4
SW	0.5	0	-	-	-	-	
SW	0.05	0	8.5	4.92	13	.899	
SW	0.005	0	11	27.8			
SW	0.167	0	7	1.74	14	.499	
SW {-1050 MV}	0.167	0	9.5	9.83			
SW {-1050 MV}	0.0167	0	10.5	19.7			

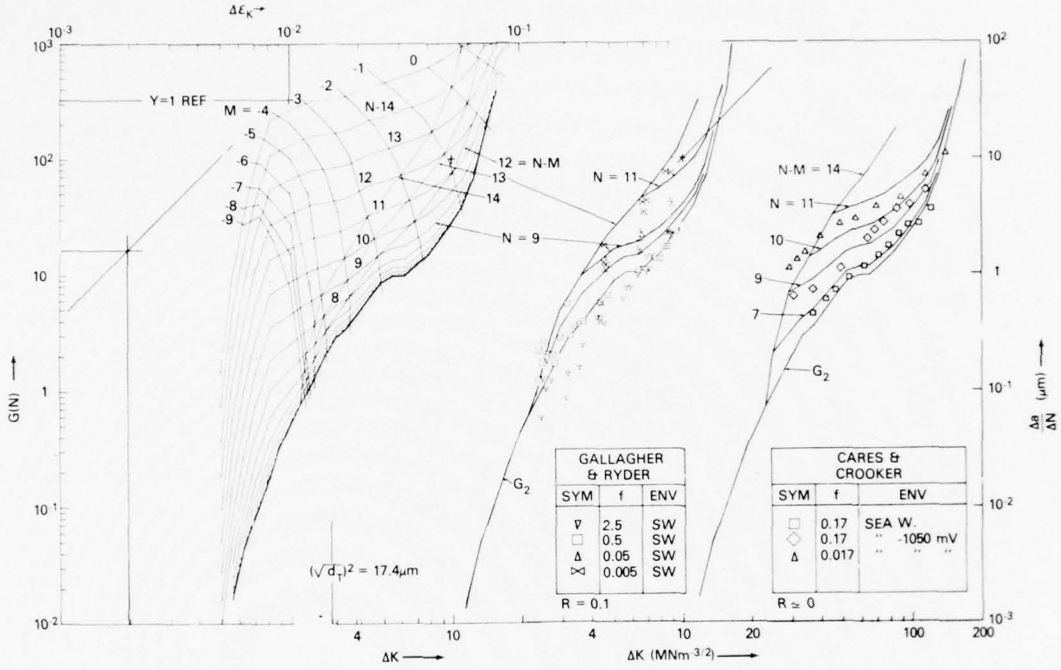

Fig. 16 — Two data sources on a 5-Ni steel are compared with a G-map for a low R-value $\simeq 0.1$. In both cases the lower bound is matched by curves of G_2 only, indicating a negligible effect of the air environment. The upper CFCP rate bound and transitional curves are as in preceding figures.

MATERIAL: X-65 LINE PIPE STEEL

REFERENCE: VOSIKOVSKY, REF 40, FIG. 17

NOMINAL CHEMISTRY WT. PCT. (FROM REF 40)

C	0.16	NB	0.031
MN	1.34	S	0.009
SI	0.16	FE	BALANCE
V	0.046		

MECHANICAL PROPERTIES

σ_{YS} = 448 KPA = 65 KSI

σ_{TUS} = 572 KPA = 83 KSI

σ_{CUS} = -703 KPA = -102 KSI

ε_U = 0.165

E = 199.8 MPA = 29000 KSI

σ_{10} = -496.1 MPA = -72000 KSI

σ_{20} = -399.6 MPA = -58000 KSI

M = 0.0063

FIRST EXCURSION DATA

N	STRAIN	STRESS (MPA)	STRESS (KSI)	THETA (MPA)	THETA (KSI)
1	0.000	0	0.0	248000	36000
2	0.001	275	40.0	248000	36000
3	0.002	400	58.1	45900	6700
4	0.003	435	63.2	25300	3700
5	0.004	449	65.3	9770	1420
6	0.005	457	66.3	1290	190
7	0.006	457	66.4	457	66
8	0.008	451	65.5	451	66
9	0.010	452	65.7	452	66
10	0.016	454	66.0	455	66
11	0.021	456	66.3	596	87
12	0.026	466	67.7	1580	230
13	0.031	475	69.1	3460	510
14	0.041	509	73.9	3160	460
15	0.051	536	77.8	2590	380
16	0.061	563	81.8	2130	310
17	0.072	584	84.8	1870	270
18	0.082	598	86.8	1500	220
19	0.093	611	88.8	1230	180
20	0.103	622	90.3	985	143
21	0.114	632	91.8	953	138
22	0.124	643	93.4	936	136
23	0.135	654	94.9	912	132
24	0.146	665	96.5	850	123
25	0.157	672	97.6	784	114
26	0.167	683	99.2	721	105
27	0.178	691	100.3	616	89
28	0.189	694	100.8	543	79

FULL-CYCLIC EXCURSION DATA

N	STRAIN	STRESS (MPA)	STRESS (KSI)	THETA (MPA)	THETA (KSI)
1	-0.004	-723	-105.0	220000	32000
2	-0.000	-689	-100.0	220000	32000
3	0.001	-551	-80.1	220000	32000
4	0.001	-413	-60.1	220000	32000
5	0.002	-276	-40.1	200000	29000
6	0.003	-138	-20.1	186000	27000
7	0.004	0	0.0	166000	24000
8	.005	114	16.6	138000	20000
9	0.006	249	36.2	86600	12400
10	0.007	312	45.3	71500	10400
11	0.008	354	51.4	48100	7000
12	0.009	389	56.5	36400	5300
13	0.010	431	62.6	28800	4200
14	0.012	474	68.8	17200	2500
15	0.014	502	73.0	13100	1900
16	0.016	524	76.2	9410	1370
17	0.018	539	78.4	7350	1070
18	0.020	555	80.6	5500	800
19	0.022	566	82.3	4610	670
20	0.024	571	82.9	3990	580
21	0.029	588	85.4	2760	400
22	0.034	605	87.9	1870	270
23	0.039	612	88.9	1560	230
24	0.044	619	89.9	1110	160
25	0.055	627	91.0	769	112
26	0.065	634	92.1	634	92
27	0.070	636	92.4	566	82

GRAPHICAL REFERENCE POINTS

$GRF|_{REF} = 10^{1.292} = 19.57$

$\Delta\varepsilon_K|_{REF} = 10^{-2.700} = .001995$

$Y|_{REF} = 10^{2.593} = 391.5$

RESULTS

ENV	FREQ (HZ)	R	N	Δr_T (nm)	N-M	$\Delta\varepsilon_p/\Delta r_T$ $(\mu m)^{-1}$	d_T (μm)
A	10	0.2					
SW	1.0	0.2					
	0.1	0.2	11	20.9	14.5	.422	16.0
	0.01	0.2	13	83.9			
SW+ZN	0.1	0.2	10.5	14.8	16	.149	
	0.01	0.2	13	83.7			

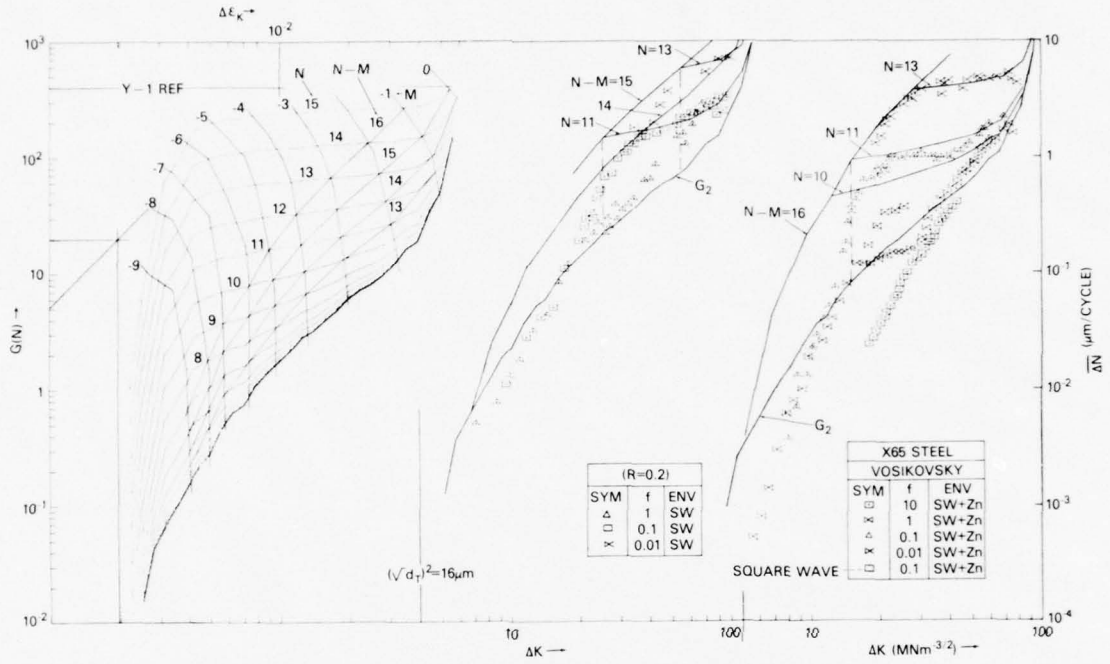

Fig. 17 — CFCP data on X-65 steel is roughly matched by G-maps developed in Figs. 3, 4, and 5. However, this strength level is thought to violate the lower limit of applicability of this model as presently constituted without reckoning for crack closure effects, and/or microstructural vs d_T size effects.

TABLE II.
DATA ON CONDITIONS OF CFCP TEST AND OF CHARACTERIZING PARAMETERS

MATERIAL	ENV	FREQ (Hz)	R	n	d_T	N	Δr_T (nm)	$\Delta r_T \cdot f$ (nm/sec)	N-M	$\Delta\varepsilon_p/\Delta r_T$ $(\mu m)^{-1}$
Ti-6Al-4V Fitzgerald & Wei Pettit et al σ_{YS} = 916 KPa σ_{TUS} = 985 KPa	A	10	0.1	0.0136	6.3				9	19.4
	SW	10	0.1			9	4.45	44.5	13	0.351
	SW	1.0	0.1			11.5	25.2	25.2		
	SW	0.1	0.1			14	142.	14.2		
Ti-8Al-1Mo-1V Bucci	IA	5	0.05	0.012	10.0	b	-	-	10.5	4.73
	IA	5	0.5							
	SW	5	0.05			10.5	21.1	105		
	SW	5	0.5			10.5	21.1	105		
	SW	5	0.75			10.5	21.1	105		
Ti-8Al-1Mo-1V Meyn σ_{YS} = 875 KPa σ_{TUS} = 1007 KPa	V	10-30	0	0.012	12.0	-	-	-	-	-
	A	10-30	0			-	-	-	10.5	5.68
	SW	10-30	0			7.5	2.20	22 - 66	13.5	0.710
	SW	2	0			11	24.9	49.8	"	"
	SW	0.5	0			13	99.6	49.8	"	"
Ti-8Al-1Mo-1V Sullivan	SW	0					(SCC V_S =) 348			
4340/400°F Krafft & Smith σ_{YS} = 1488 KPa σ_{TUS} = 1881 KPa	A	10	0.1	0.0065	3.1	-	-	-	13.5	4.23
	FW	10	0.1			11	4.18	41.8	18.5	0.0939
	FW	4	0			12.3	10.3	41.2	"	"
	FW	2	0			13.3	20.6	41.2	"	"
	FW	1	0			14.3	41.2	41.2	"	"
	FW	0.5	0			15.3	82.4	41.2	"	"
	FW	0					(SCC V_S =) 220			
4340/600°F Krafft & Smith σ_{YS} = 1406 KPa σ_{TUS} = 1605 KPa	V	10		0.0048	9.0	7.5	-	-	-	-
	A	10	0.1			10	4.48	4.48	11.5	7.88
	FW	4	0			11.5	12.7	50.8	20.5	0.0154
	FW	2	0			12.5	25.4	50.8	"	"
	FW	1	0			13.5	50.7	50.7	"	"
	FW	0.5	0			14.5	101.	50.5	"	"
	FW	0					(SCC V_S =) 34			
4140/800°F Krafft & Smith σ_{YS} = 1250 KPa σ_{TUS} = 1370 KPa	A	10	0.1	0.059	9.0	-	-	-	11.5	6.41
	A	10	0.5			-	-	-		
	FW	2	0			8	1.38	2.76	18.0	0.0709
	FW	0.5	0			10	5.51	2.76	"	"
	FW	0					(SCC V_S =)11.5		"	"
4340/1000°F Krafft & Smith σ_{YS} = 1030 KPa σ_{TUS} = 1080 KPa	A	10	0.1	0.0066	9.0	-	-	-	11.5	5.73
	FW	1	0		8.5	2.18	2.18	1.09	14.0	1.01
	FW	0.5	0			8.5	2.18	1.09	"	"
	FW	0					(SCC V_S =) 0.45			
Fe-5Ni + (Cr, Mo, V) Ryder & Gallagher σ_{YS} = 958 KPa σ_{TUS} = 1030 KPa	SW	2.5	0	0.0077	17.4	-	-	-	-	-
	SW	0.5	0			-	-	-	-	-
	SW	0.05	0			8.5	4.92	0.216	13.0	0.899
	SW	0.005	0			11	27.8	0.139	"	"
Fe-5Ni + (Cr, Mo, V) Cares & Crooker	SEA	0.167	0	0.0077	17.4	7	1.74	0.291	14.0	0.499
	SEA (-1050MV)	0.167	0			9.5	9.83	1.64	"	"
	SEA (-1050MV)	0.0167	0			10.5	19.7	0.329	"	"
X-65 Steel σ_{YS} = 448 KPa σ_{TUS} = 572 KPa	A	10	0.2	0.0063	16.0	-	-	-	-	-
	SW	1.0	0.2			-	-	-	-	-
		0.1	0.2			11	20.9	2.09	14.5	0.422
		0.01	0.2			13	83.9	0.839		
	SW + Zn	0.1	0.2			10.5	14.8	1.48	16.0	0.149
		0.01	0.2			13	83.7	0.837	"	"

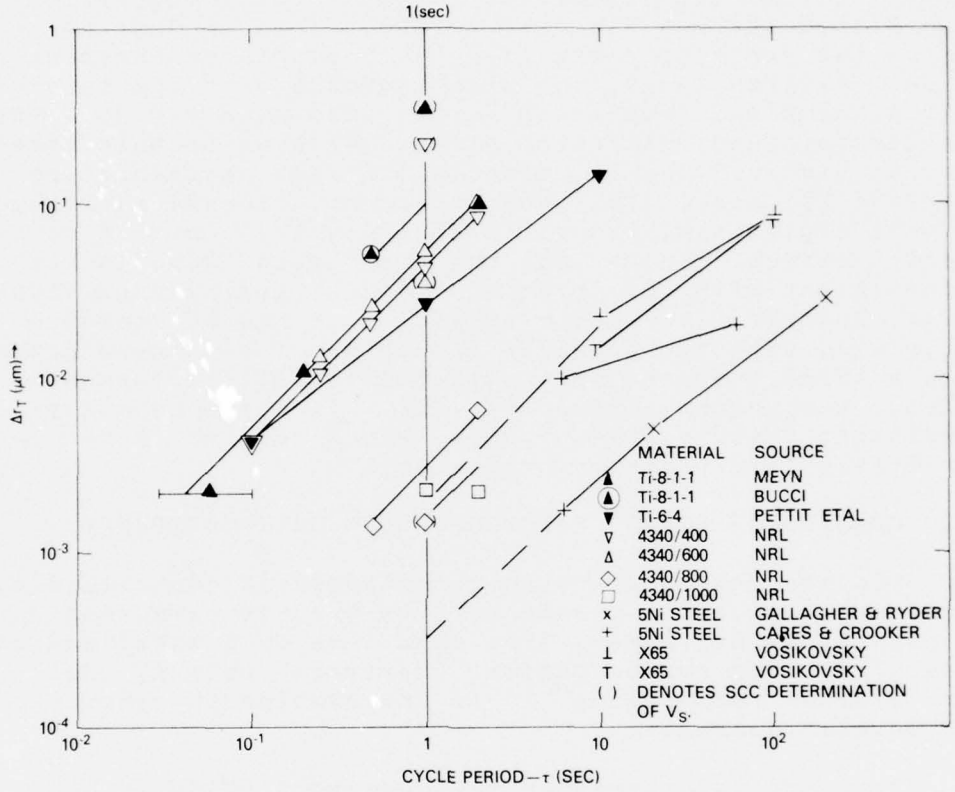

Fig. 18 — Data organization is proposed in terms of this log plot of Δr_T vs cycle duration τ, plus the $\Delta\epsilon_p/\Delta r_T$ values (N-M indexes) defining frequency independent limits of Table II. Here the one second intercept is compared with V_S estimates in stress corrosion cracking experiments. A 1:1 slope denotes constant V_S.

$$\Delta K_{th} = \sqrt{2\pi d_T}\, E\left(\frac{3}{2} - R\right)\frac{\sigma_{YS}}{E} \qquad (93)$$

Such a trend line, normalized with respect to ΔK_{TH} at R = 0 is compared in Fig. 19 with the extensive ΔK_c or ΔK_{TH} collection of Pook [43]. The Pook data is normalized with respect to the ΔK_{TH} intercept for R = 0 of a regression line fitted through his data points. This is done to reduce the error of normalizing to a single measurement value. Alternatively, one might normalize to the intercept at some intermediate R value, such as R = 0.33 where the centroid neutralization effect vanishes in this model. Also at higher R-levels, effects of crack reclosure are expected to cease. This model does not include reclosure effects explicitly, except that due to the centroid neutralization effect. In general the model prediction is not inconsistant with Pook's data. From an engineering viewpoint, however, it is discouraging that none of Pook's materials, with the possible exception of his 60-40 brass, show a trend favoring that expected for no environmental effect, the vacuum line of Fig. 19. Is there no alloy condition, heat treatment, etc., which obtains an R- insensitivity for the air environment?

21. MEANING OF STRAIN RATE/CORROSION RATE CONSTANCY

The meaning of a growth rate threshold controlled by a fixed ratio of local strain rate to surface corrosion rate is not altogether clear. The data base is limited and in need of further corroboration. However, assuming that this will be forthcoming, it is interesting to speculate on possible mechanisms.

There are two threshold contours to consider. The upper one, the locus of Stage II growth augmentation, could well be a rate controlled process. Here one might regard the strain rate of the d_T-ligament as a means of producing fresh, nascent surface, by the emergence of dislocation steps at localized regions at its surface. The rate of supply of fresh surface via the strain rate is augmented by the environmental attack, which induces growth, hence strain rate. But this appears to be a stable process. There is a self-stabilization inherent most corrosion processes. Corrosion produces inert waste products which tend to seal off the surface under attack, hence slow the process. Since the corrosion is self-generating of its "fuel" in the sense that nascent metal is fuel, one might expect that the self-impedance of the supply of fresh surface might prove unstable in the

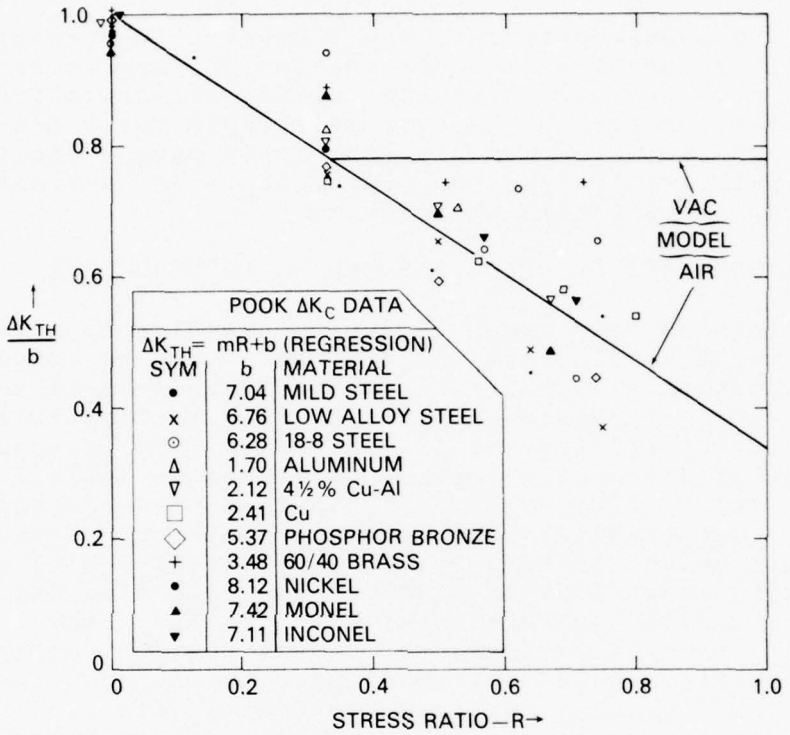

Fig. 19 — The model, as a result of T-C envelope centroid neutralization, predicts the trends shown for the ΔK_{TH} limit vs R, which seems fairly consistent with extensive NEL-data of Pook

negative sense. A bit of surface fouling slows the attack rate, hence the crack growth rate, hence the strain rate, hence the supply of fresh fuel, hence the attack, etc.,etc., until the process is cut off. In this way, even though the oxide film is not impervious, still an absolute cutoff might be reached at a particular level of strain rate relative to corrosion rate.

The lower contour is the frequency independent air line. The parametric line of constant $\Delta\bar{\varepsilon}_p/\Delta r_T$ is frequency independent. Wei [44] sees the initial air-oxidation of clean steel surfaces to be extremely rapid for a monolayer or so; then stop. Presumably, then this puts a limit on what we call Δr_T, which then limits $\Delta\bar{\varepsilon}_p$. The rationale here is not too satisfactory at present.

22. MICROGRAPHIC EVIDENCE FOR THE d_T PROCESS ZONE

There have been some published investigations in which or from which a calculated d_T from Eq. 2 can be compared with quantitative microstructural or fractographic measurements. The most reasonable parameters are the fractographic dimple size or spacing and the inclusion size or spacing. Such data of which we are aware is listed in Table III and crossplotted in Fig. 20. The trend is positive although far from quantitative. Actually the departure of the trend from a 1:1 match, in Fig. 20, is a relatively small effect. Thus adding about 1 μm to each process zone size calculation, as a fixed correction, would shift the slope to that expected. Even if perfect, the d_T fractographic dimple size correlation would say nothing of the numerous non-dimpled fractographic features associated with high cycle fatigue and stress-corrosion cracking. It can be argued [45] that the instability event, which controls the rate of the fracturing process, could be followed by a separation process which tends to obliterate the evidence for such a stage. At the present time, the more definitive way of determining the d_T quality index is by data vs G-map matching procedures.

CONCLUSIONS

The following are indicated by this study.

A. It is possible to track CFCP data with a double set of parametric lines. The first of these represents the frequency dependent growth. It is derived by summing a transitional growth rate factor to that basic to vacuum fatigue. The other is derived from the first, overlaid by a map of the strain rate at the crack tip due to crack loading plus crack propagation. This provides loci of

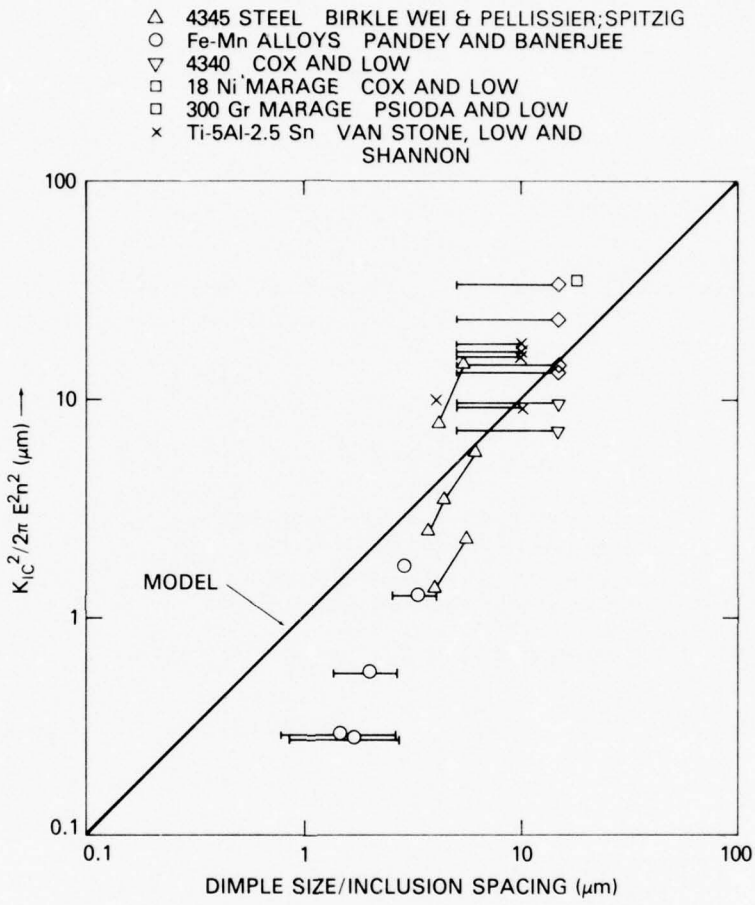

Fig. 20 — Comparison of calculated d_T process zone size with measured fractographic/microstructural features, from sources noted (see Table III) shows a reasonable correspondence

TABLE III.

TABULATION OF VARIOUS MICROSTRUCTURAL AND FRACTOGRAPHIC SIZE PARAMETERS

SOURCE	ALLOY & HEAT TREAT				TEST TEMP	σ_{YS} (GPa)	σ_{TUS} (GPa)	E (GPa)	σ_{YS}/σ_{TUS}	"m"(a)	n	UNIFORM STRAIN	K_{Ic} (MPa-m$^{1/2}$)	d_T(d) (μm)	DIMPLE SIZE Min	(μm) Avg.	Max
Pandey & Banerjee Ref. 46	$3B_2$	12Mn-8	Mo + Fe	Heat	Ambient	1.23		212			0.13		37.1	0.29	0.80	1.44	2.69
	$3B_1$	12Mn-8		WQ	Ambient	1.25		212			0.10		27.5	0.29	0.85	1.70	2.74
	$2A_2$	12Mn-8	Mo + Fe	LN	Ambient	1.14		212			0.09		36.0	0.55	1.38	2.01	2.61
	$4C_2$	12MN-2	Ni -2Mo	Temper	Ambient	1.21		212			0.07		50.3	1.7	2.77	2.87	3.00
	$1C_1$	13MN-2	Ni -4Mo	WQ	Ambient	1.03		212			0.08		46.9	1.3	2.58	3.30	4.26
Spitzig Birkle Wei Pelissier Refs. 47 & 48	4345	0.0085	Q & T	-204°C	Ambient	1.63	2.08	200	0.787	0.085	0.06		45.3	2.3		5.6(e)	
	4345	0.0255	Q & T	-204°C	Ambient	1.64	2.05	200	0.801	0.080	0.06(t)		40.8	1.8		——	
	4345	0.0495	Q & T	-204°C	Ambient	1.61	2.03	200	0.793	0.084	0.06		33.3	1.2		4.0(e)	
	4345	0.0085	Q & T	316°C	Ambient	1.45	1.63	200	0.594	0.050	0.06		71.8	5.7		6.1(e)	
	4345	0.0255	Q & T	316°C	Ambient	1.48	1.64	200	0.599	0.049	0.06		56.0	3.5		4.4(e)	
	4345	0.0495		316°C	Ambient	1.50	1.63	200	0.924	0.040	0.06		47.0	2.5		3.7(e)	
	4345	0.0085	Q & T	427°C	Ambient	1.39	1.50	200	0.927	0.0039	0.05		94.6	14.2		5.4(e)	
	4345	0.0255		427°C	Ambient	1.40	1.50	200	0.935	0.0035	0.05		78.8	9.9		——	
	4345	0.0495		427°C	Ambient	1.38	1.48	200	0.930	0.0017	0.05		69.2	7.6		4.3(e)	
Cox & Low Ref. 49	4340	Comm.	Q & T	427°C	Ambient	1.41	1.53	200	0.923	0.04	0.055(b)		74.6	7.3		5 - 10	
	4340	Hi Pur	Q & T	427°C	Ambient	1.41	1.50	200	0.940	0.034	0.068		10.7	9.9			
	18N1	Comm.	Age	454°C	Ambient	1.34	1.37	181	0.980	0.017	0.052		124.	28		——	
	18N1	Hi Pur	Age	454°C	Ambient	1.31	1.37	181	0.955	0.028	0.040		164(c)	82		14	
Paloda & Low Ref. 50	18N1	Comm	Age	427°C 3h	Ambient	1.55	1.65	181	0.941	0.033	0.049(b)		10.6	23			
	Maraging	300Gr	Age	482°C/ 3h	Ambient	1.85	1.92	181	0.964	0.024	0.033		85.9	33		5 - 15	
	Maraging	300Gr	Age	538°C/ 3h	Ambient	1.70	1.79	181	0.946	0.031	0.043		73.3	14			
	Maraging	300Gr	Age	427°C/ 100h	Ambient	2.07	2.12	181	0.971	0.021	0.034		55.9	13			
Van Stone Low & Shannon Ref. 51	Ti-5Al-2.5Sn		Air	Cool	295°K	0.703	0.758	107	0.927	0.038	0.106(b)	0.076	119	17		5 - 10	
	ELI		Air	Cool	77	1.18	1.25	121	0.944	0.033	0.090	0.103	111	16			
			Air	Cool	20			128					90.1				
			Furnace	Cool	295	0.682	0.747	107	0.912	0.044	0.107	0.107	114	16		5 - 10	
			Furnace	Cool	77			121			0.090		82.4	9.1			
			Furnace	Cool	20			127					69.2				
			β-aged		295	1.28	1.36	107	0.945	0.032	0.065	0.029	54.9	10			

(a) After Rowe, Ref. 53

$$\left(\frac{0.002\,e}{m}\right) = \frac{\sigma_{ys}}{\sigma_{TUS}}$$

(b) From slope δ and stress δ of authors' true stress-strain curves at 10% strain

$$n = \frac{\delta}{\sigma}$$

(c) K_Q value, invalid K_{Ic}

(d) $d_T = \frac{1}{2e}\left(\frac{K_{Ic}}{Em}\right)^2$

(e) Inclusion Spacing

(f) Bracket denotes nominal value

constant ratio of strain rate to surface attack rate. These loci match CFCP trends in air, and the threshold of Stage II growth in aqueous environments.

B. A minimum-parameter characterization scheme results from these considerations. It involves finding the members of the two parametric families best fitting a particular data set. Such characterization appears to provide a useful predictive capability for estimating effects of CFCP.

ACKNOWLEDGEMENTS

This work was carried out in the Ocean Technology Division, J. P. Walsh, Superintendent, under auspices of NAVAIR and ONR funding in the Structural Mechanics Sub-element. Appreciation is also due our Junior Associate, Harry L. Archer, Jr., who labored assiduously to devise and perfect the computer techniques.

REFERENCES

1. Krafft, J. M. "Correlation of Plane Strain Crack Toughness with Strain-Hardening Characteristics of a Low, Medium, and a High Strength Steel," Appl. Mat. Res. Vol. 3, (1964) pp. 88-101.

2. Krafft, J. M. and Mulherin, J. H., "Tensile-Ligament Instability and the Growth of Stress-Corrosion Cracks in High-Strength Alloys," Trans. ASM Vol. 62, (1969) p. 64-81.

3. Landes, J. D. and Wei, R. P., "The Kinetics of Sub-Critical Crack Growth and Deformation in a High-Strength Steel," Trans. ASME, J. Eng. Mat. Tech., Series H, Vol. 95, (1973), p. 2-9.

4. Krafft, J. M., "Strain-Hardening vs Stress-Relaxation Effects on Fatigue Crack Propagation," Report of NRL Progress, p. 1-10, July (1971).

5. Krafft, J. M., Lamb, C. L., and Simmonds, K. E., "Corrosion- and Creep-Induced Instability Modeling of Fatigue-Cracking in Various Alloys," NRL Memorandum Report 2399, February 1972.

6. Krafft, J. M. and Smith, H. L., "Ligament Instability Model for Stress Corrosion and Fatigue Crack Propagation in a 4340 Steel," NRL Memorandum Report 2598, April 1973.

7. Speidel, M. O., "Corrosion Fatigue in Fe-N-Cr Alloys," Conf. on "Stress Corrosion and Hydrogen Embrittlement of Iron Base Alloys" Unieux-Firminy, France, 10-12 June 1973.

8. Dawson, D. B. and Pelloux, R., "Corrosion Fatigue Crack Growth of Titanium Alloys in Aqueous Environments," Met. Trans. Vol. 5, (1974) p. 723-731.

9. Paris, P. and Erdogan, F., "A Critical Analysis of Crack Propagation Laws," ASME Trans., Sec. D., Vol. 85, p. 528-534 (1963).

10. Irving, P. E. and Beevers, C. J., "The Effect of Air and Vacuum Environments on Fatigue Crack Growth Rates in Ti-6Al-4V," Met. Trans. Vol. 5, p. 391-398 (1974). Also: "Microstructural Influences on Fatigue Crack Growth in Ti-6Al-4V," Mat. Sci. Engrs. Vol. 14, p. 229-238 (1974).

11. Cooke, R. J., Irving, P. E., Booth, G. S., "The Slow Fatigue Crack Growth and Threshold Behavior of a Medium Carbon Alloy Steel in Air and Vacuum," Engrg. Fract. Mech. Vol. 7, pp. 69-77 (1975).

12. Fitzgerald, J. H. and Wei, R. P., "A Test Procedure for Determining the Influence of Stress Ratio on Fatigue Crack Growth," J. Testing and Evaluation, Vol. 2, p. 67-70 (1974).

13. Paris, P. C., Bucci, R. J., Wessel, E. T., Clark, W.G., and Mager, T. R., "An Extensive Study on Low Fatigue Crack Growth Rates in A533 and A508 Steels," ASTM-STP #513, pp. 141-176 (1972).

14. Bucci, R. J. "Environment-Enhanced Fatigue and Stress Corrosion Cracking of a Titanium Alloy Plus a Simple Model for the Assessment of Environmental Influence on Fatigue Behavior," Ph.D. Thesis, Lehigh University, Bethlehem, Pennsylvania (1971).

15. Pettit, D. E., Krupp, W. E., Ryder, J. T. and Hoeppner, D. W., "Investigation of the Effects of Stress and Chemical Environments on the Prediction of Fracture in Aircraft Structural Materials," Report LR 26026, Lockheed-California Co. July 1973.

16. Orowan, E., "Conditions of High-Velocity Ductile Fracture," J. Appl. Phys., Vol. 26, pp. 900-902, (1975).

17. Williams, J. G. and Turner, C. E., "The Plastic Instability Viewpoint of Crack Propagation," Appl. Mat. Res. Vol. 3, p. 144-147 (1964).

18. McClintock, F. A., "Ductile Fracture Instability in Shear," J. Appl. Mech. Vol. 25, p. 582-588 (1958).

19. Hutchinson, J. W., "Singular Behavior at the End of a Tensile Crack in a Hardening Material," J. Mech. Phys. Solids, Vol. 16, pp. 13-31, (1968).

20. Rice, J. R. and Rosengren, G. F., "Plane Strain Deformation Near the Crack Tip in a Power Hardening Material," J. Mech. Phys. Solids, Vol. 16, pp. 1-12, (1968).

21. Liu, H. W., "Shear Cracks and Double-Ended Dislocation Arrays," J. Appl. Phys., Vol. 36, pp. 1468-1470, (1965). Also Ke, J. S. and Liu, H. W., "Measurements of Fracture Toughness of Ductile Materials,"

Eng. Fract. Mech., Vol. 5, pp. 187-202, (1973).

22. Tetleman, A. S., "Recent Developments in Classical (Internal) Hydrogen Embrittlement," in Hydrogen in Metals, American Society for Metals, I. M. Bernstein and A. W. Thompson, pp. 17-34 (1974).

23. Troiano, A. R., Keynote Lecture in Hydrogen in Metals, American Society for Metals, I. M. Bernstein and A. W. Thompson, eds. pp. 1-15, (1974).

24. Paton, N. E. and Williams, J. C., "Effect of Hydrogen on Titanium and Its Alloys," in Hydrogen in Metals, American Society for Metals, I. M. Bernstein and A. W. Thompson, eds. pp. 409-432, (1974).

25. Krafft, J. M. "An Interpretation of the Yoder-Griffis-Crooker Observations of Sustained-Load Cracking in Ti-6Al-4V," J. Eng. Mat. Tech., p. 275-282 (1974).

26. Guiu, F. and Pratt, P. L., "Stress Relaxation and Plastic Deformation of Solids," Phys. Stat. Solidi, Vol. 6, pp. 111-120 (1964).

27. Hart, E. W., "A Phenomenological Theory for Plastic Deformation of Polycrystalline Metals," Acta Met., Vol. 18, pp. 599-610 (1970). Also: D. Lee and E. W. Hart, "Stress Relaxation and Mechanical Behavior of Metals," Met. Trans. Vol. 2, p. 1245-1248 (1971).

28. Marsh, K. J. and Campbell, J. D., "The Effect of Strain Rate on the Post-Yield Flow of Mild Steel," J. Mech. Phys. Solids, Vol. 11, pp. 49-63 (1963).

29. Krafft, J. M. and Sullivan, A. M., "On Effects of Carbon and Manganese Content and of Grain Size on Dynamic Strength Properties of Mild Steel," ASM Trans. Vol. 55, pp. 101-118, (1962).

30. Landgraf, R. W., "Cumulative Fatigue Damage Under Complex Strain Histories," in ASTM-STP #519, p. 213-228 (1973).

31. Jhansale, H. R. and Topper, T. H., "Engineering Analysis of the Inelastic Stress Response of a Structural Metal Under Variable Cyclic Strains," ASTM STP-519, p. 240-270 (1973).

32. Bucci, R. J., Paris, P. C., Loushin, L. L. and Johnson, H. H., "A Fracture Mechanics Consideration of Hydrogen Sulfide Cracking in High Strength Steels," ASTM-STP #513, pp. 292-307 (1972).

33. Krafft, J. M., "An Interpretation of Lower Yield Point Plastic Flow in the Dynamic Testing of Mild Steel," Acta. Met. Vol. 10, p. 85-93 (1962).

34. Hollomon, J. H., "Tensile Deformation, Trans. AIME, Iron and Steel Div. 162, p. 268-290 (1945).

35. Unangst, K. D., Shih, T. T. and Wei, R. P., "Crack Closure and Fatigue Crack Growth in 2219-T851 Aluminum Alloy," Interim Report to Air Force Office of Scientific Research, Lehigh University, Bethlehem, Pennsylvania (1976).

36. Meyn, D. A., "An Analysis of Frequency and Amplitude Effects on Corrosion Fatigue Crack Propagation in Ti-8Al-1Mo-1V," Met. Trans. Vol. 2, pp. 853-865, (1971).

37. Gallagher, J. P., "Corrosion Fatigue Crack Growth Rate Behavior Above and Below K_{Iscc} in Steels," J. of Materials, JMLSA Vol. 6, pp. 941-964 (1971).

38. Ryder, J. T. and Gallagher, J. P. "Temperature Influence on Corrosion Fatigue Behavior of 5Ni-Cr-Mo-V Steel," J. Test. Eval. Vol. 2, pp. 180-189 (1974).

39. Crooker, T.W., Bogar, F. D., and Cares, W. R., "Effects of Flowing Natural Seawater and Electrochemical Potential on Fatigue Crack Growth in Several High-Strength Marine Alloys, NRL Report 8042, August 1976.

40. Vosikovsky, O., "Fatigue-Crack Growth in an X-65 Line-Pipe Steel of Low Cyclic Frequencies in Aqueous Environments," Trans. ASME, JEMT, p. 298-304 (1975).

41. Krafft, J. M. and Gray, R., Jr., "Effects of Neutron Irradiation on Bulk and Micro Flow-Fracture Behaviors of Pressure Vessel Steels," in Proceedings, Practical Applications of Fracture Mechanics to Pressure Vessel Technology, Inst. Mech. Engrg., London 1971, pp. 93-102.

42. Sullivan, A. M., "Velocity of Cracks Extending under Stress in an Adverse Environment," Proc. 2nd Intl. Conf. on Fracture, Chapman-Hall, Ltd. Brighton, Great Britian, p. 396 (1970).

43. Pook, L. P., "Fatigue Crack Growth Data for Various Materials Deduced from the Fatigue Lives of Pre-cracked Plates," ASTM-STP-#513, pp. 106-124 (1972).

44. Wei, R. P., Private Communication.

45. Krafft, J. M., "Tests for Fracture Strength, Static to Impact," in Techniques of Metals Research, 5, Part 2, p. 1, (1971).

46. Pandey, R. K. and Banerjee, S., "Studies on Fracture Toughness and Fractographic Features in Fe-Mn Base Alloys," Engrg. Fract. Mech., Vol. 5, pp. 965-975, (1973).

47. Spitzig, W. A., "Correlations Between Fractographic Features and Plane-Strain Fracture Toughness in an Ultrahigh-Strength Steel,". Also Spitzig, W. A., Pellisier, G. E., Beachem, C. D., Brothers, A. J., Hill, M. and Warke, W. R., "A Fractographic Analysis of the Relationships Between Fracture Toughness and Surface Topography in Ultra-high Strength Steels," ASTM-STP#436, p. 17, (1968).

48. Birkle, A. J., Wei, R. P. and Pellissier, G. E., "Analysis of Plane-Strain Fracture in a Series of 0.45C-Ni-Cr-Mo Steels with Different Sulfur Contents," Trans. ASM, Vol. 59, pp. 981-990, (1966).

49. Cox, T. B. and Low, J. R., "An Investigation of the Plastic Fracture of High Strength Steels," NASA Technical Report No. 5, Carnegie-Mellon University, Pittsburgh, Pa. 15213 (1973).

50. Psioda, J. A. and Low, J. R., "The Effect of Microstructure and Strength on the Fracture Toughness of an 18Ni-300 Grade Maraging Steel," NASA Technical Report #6, Carnegie-Mellon University, Pittsburgh, Pa. 15213, (1974).

51. Van Stone, R., Low, J. and Shannon, "The Effect of Microstructure on the Fracture Toughness of Titanium Alloys," NASA Technical Report No. 2-Ti, Carnegie-Mellon University, Pittsburgh, Pa. 15213, (1974).

52. Aerospace Structural Metals Handbook-1970 Edition, Mechanical Properties Data Center, Belfour Stulin, Inc. (1970).

53. Rowe, G., "Correlation of High-Cycle Fatigue Strength with True Stress-Strain Behavior," J. of Materials, Vol. 1, 1968, pp. 689-715.

APPENDIX
ILLUSTRATED SUMMARY OF NRL MEMO REPORT #3505

1. Corrosion fatigue crack propagation, CFCP, is frequently implicated in mechanical failures of machinery and structures subjected to frequent loading fluctuations in operational environments. However, CFCP behaviors vary so markedly with material, environment, load ratio and frequency that engineering estimates of its course are imprecise, and data required to refine predictions costly. This report describes improvements of a model relating CFCP to Engineering mechanical properties - ordinary and cyclic stress-strain curves - by which many hitherto anomolous behaviors are reconciled. The new method could improve accuracy and reduce cost of safe-life predictions for engineering structures.

2. Developed here is a connection between the strain rate of material at the crack tip and CFCP. It is found that the plastic strain rate in the loading cycle time must exceed a level commensurate with the total corrosive activity in the cycle before the environment can affect crack growth. Thus the threshold of corrosion-fatigue augmentation, generally a large jump in crack growth rate, hence decrease in "safe life", is defined by a locus of constant ratio of crack-tip strain rate to crack-tip corrosion rate. Parametric maps of such loci, readily prepared from stress-strain data, provide a useful means for characterizing CFCP behavior.

3. Briefly this summary reviews concepts of the earlier, basic model, which provides crack-growth rate-factors for the limiting cases of dry vacuum fatigue and of stress corrosion cracking. A hybrid growth-rate-factor is then developed and combined with growth-factor parametric mapping to define the frequency independent growth rate limit of CFCP. An example of model-to-data comparison illustrates the manner of presentation of the numerous case studies of the full report.

4. The hypothesis of this model is that cracks grow to, and only to, that extent required to maintain a constant load condition within a small fixed distance from a crack tip. Examining this proposal leads to two basic questions: firstly, how is the constant-load condition maintained in ordinary uniaxial tensile deformation; and secondly, how can crack growth serve to maintain it in the context of the corrosion fatigue environment? Consider now these questions in turn.

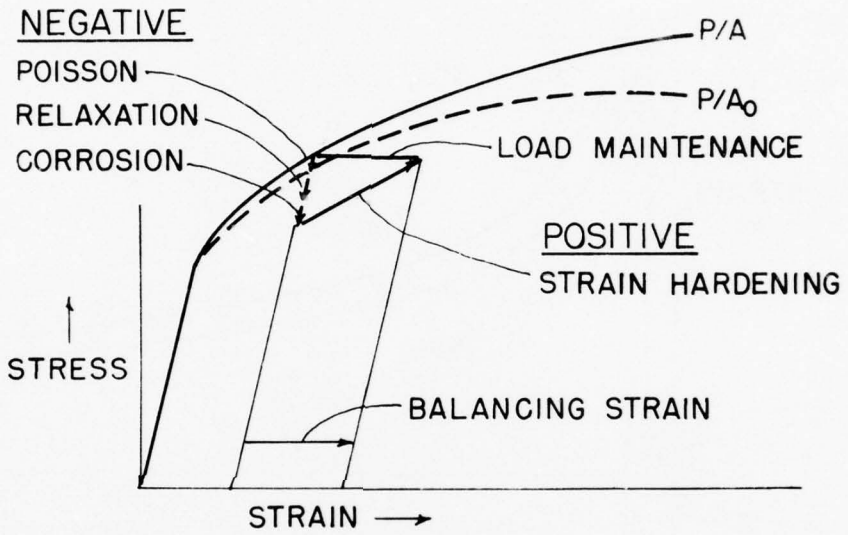

Fig. A-1 — Load partials

5. In the ordinary tension test of a material, free of an upper yield point effect, constant load occurs in the maximum or ultimate tensile stress region. Here, Fig. A1, the strain hardening rate, as a strength partial, has decreased to a level too low to compensate for load loss due to lateral (Poisson) contraction, as an areal partial. Two additional partials can affect crack tip stability: a strength partial, stress relaxation; and an areal partial, corrosion-like surface attack. Three of the four partials are negative, hence reduce the load capability; only that of strain hardening is positive. Since strain-hardening requires straining, setting the sums of the four partials to zero indicates how much strain is required to strike this balance.

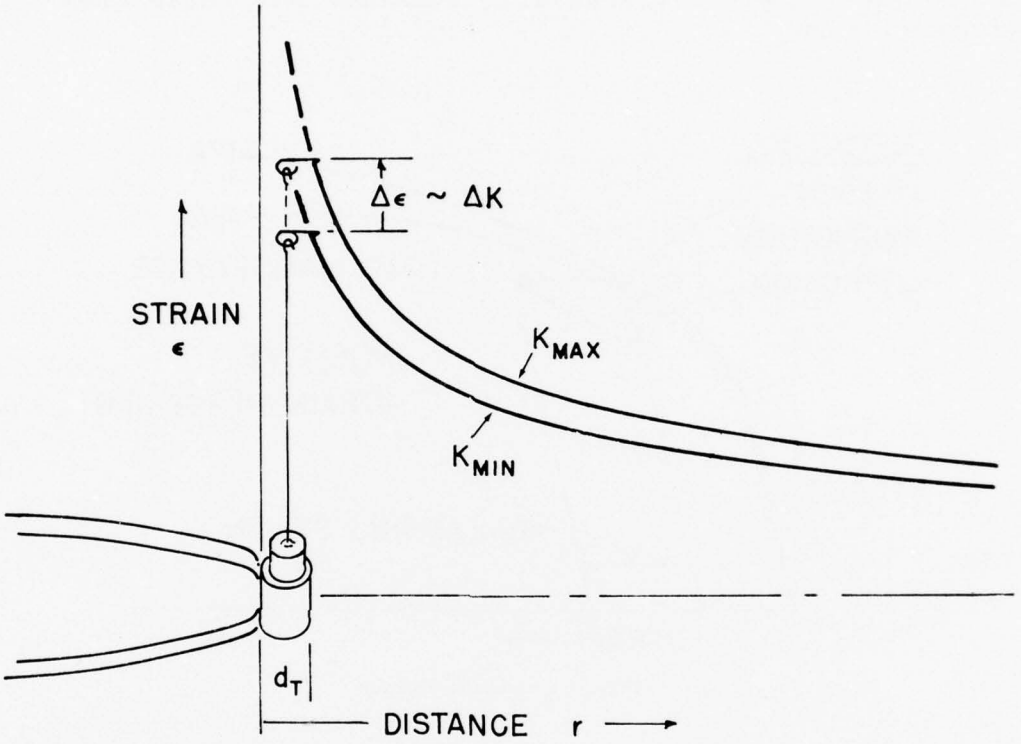

Fig. A-2 — Strain from crack loading

6. Next we ask how such straining can be provided to "specimen material" within some fixed distance from a crack tip. There are two ways. Fig. A2 depicts that due to crack loading. Here we envisage a tiny tensile specimen as connected to the strain concentration or singularity pattern associated with the loaded crack. As load increases, so does the whole pattern of strain concentration, hence so does the strain.

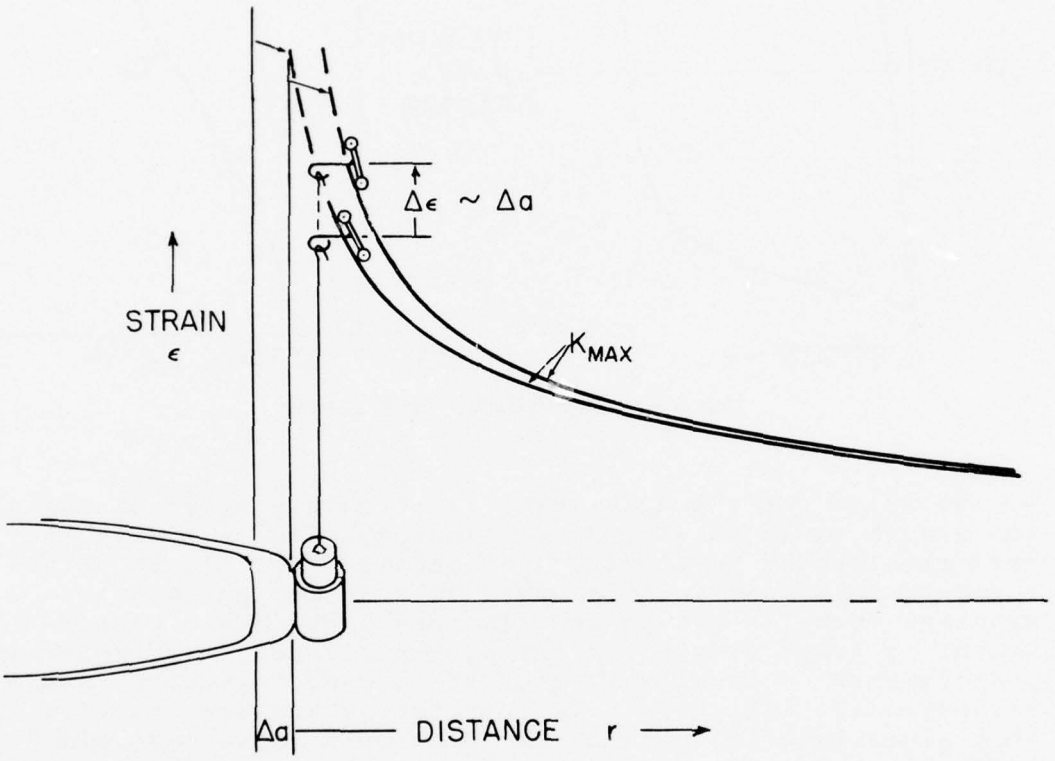

Fig. A-3 — Strain from crack growth

7. Alternatively suppose load on the cracked body is maintained, while the crack advances towards a fixed point in the material. Then, Fig. A3, our "specimen" coupled to the strain singularity "ramp" is extended by the wedging action of the advancing ramp. In balancing the load-partial equation for CFCP, only the propagation strain of Fig. A3 is applicable since the growth is executed after the load has been applied to the crack. However the loading-strain term is needed to estimate the total strain, hence strain rate, averaged over the total cycle time.

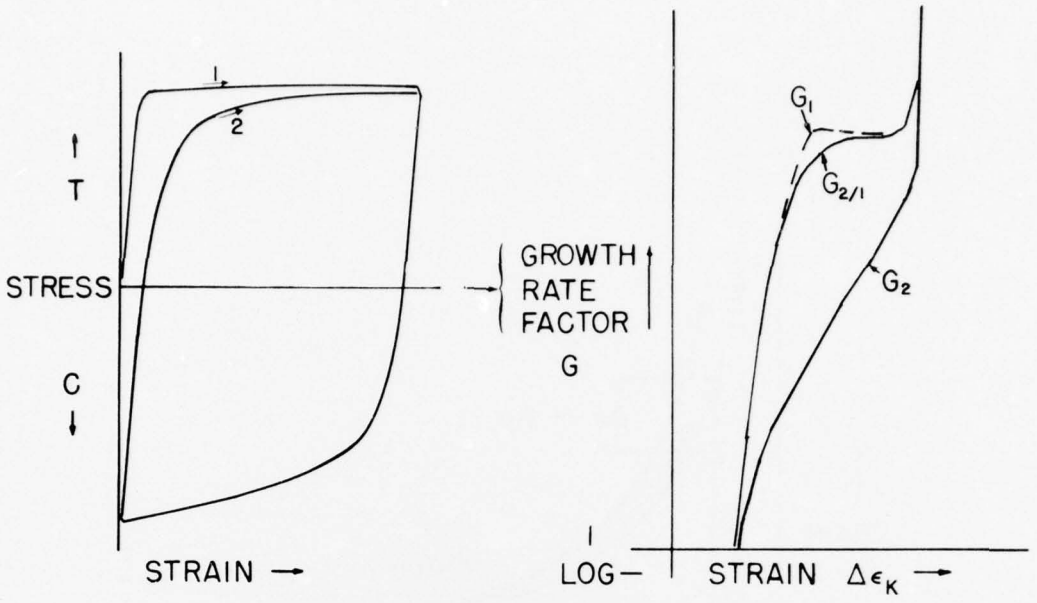

Fig. A-4 — Stress/strain — crack growth

8. We solve for a crack-growth relationship by combining the growth vs local strain relationship, Fig. A3, with the load maintenance vs strain relationship, Fig. A1, to obtain a growth relationship, Fig. A4. This is set up in dimensionless form, in growth rate factors G which are proportional to crack growth per cycle, and a strain $\Delta\varepsilon_K$, which is proportional to crack loading or the stress intensity factor excursion ΔK. The growth rate factor curves are specific to a given material through its particular stress-strain curve(s), hence its strain hardening behavior. The ordinary tensile curve, denoted by 1 in Fig. A4, is typically of more acute yield point than the cyclic curve 2; so correspondingly is its growth rate factor G_1. We regard G_2 as basic, applying to it a proportionality factor associated with the stress-relaxation partial. Sustained load or stress-corrosion cracking, on the other hand, is associated with G_1. For corrosion fatigue, a transitional growth rate factor $G_{2/1}$ is defined which employes the strain hardening rate of the ordinary 1 (true) stress strain curve but the stress of the cyclic 2 curve. Since the cyclic stress envelope is lower and smoother, so correspondingly is $G_{2/1}$ vs G_1 only. We associate $G_{2/1}$ with the corrosive partial only, as an adjunct to the stress relaxation partial utilyzed in conjunction with G_2.

9. Three additional features of the new modelling should be noted; illustrated by Fig. 2 of the full report.

a. Firstly, a centroid neutralization rule is invoked, whereby the cyclic true stress-strain envelope skews along its elastic load line until its centroid of area rests on the zero stress axis. For very low plastic strain, stress excursions just exceeding the yield point, this is impossible without introducing compressive strain, which in turn is an impossible effect of an elastic stress field collapsing upon crack unloading. A slight additional tensile strain, hence ΔK-offset, one-half the yield strain, permits the centroid neutralization under these conditions. This strain offset sets the minimum value of ΔK for the fatigue propagation threshold, however high the load ratio R.

b. The second feature pertains to the disposition of the cyclic envelope for $R > 0$. We assume it to be of the same form as the full cyclic curve of reduced strain excursion, but subtended from the profile of the full cyclic stress-strain curve exercised to the maximum strain.

c. The third feature, closely related to the second, is that the strain gradient, the ramp slope for propagation in Fig. A3, is assumed proportional to the strain excursion $\Delta\varepsilon_K$, not the maximum strain, ε_{max}.

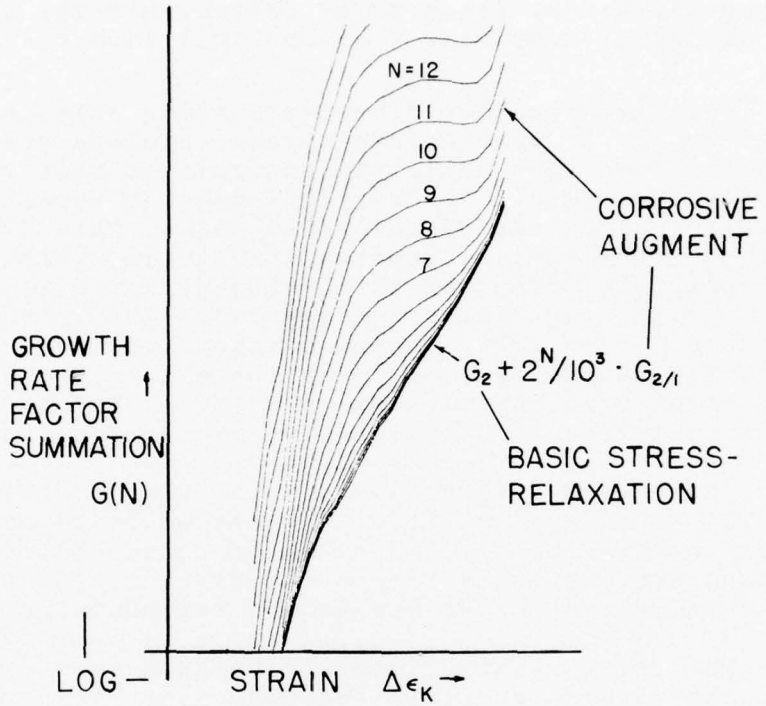

Fig. A-5 — Combined growth sources

10. One doesn't know, prior to comparing G plots with crack growth rate data, how much of the "corrosion partial" is applicable to a particular material/corrosive environment combination. How much involves a fitting parameter. To provide a range of selections, we map out a parametric family of G curves, adding to the basic G_2 an arbitrary initial coefficient times $G_{2/1}$, Fig. A5. Then a second plot is made with the arbitrary coefficient doubled, then again times 4, 8, 16, etc. to 2^{15}. We call the sum G(N), and in data comparisons ask what value of N provides a member of the parametric curve family best fitting the growth rate data of a given loading frequency.

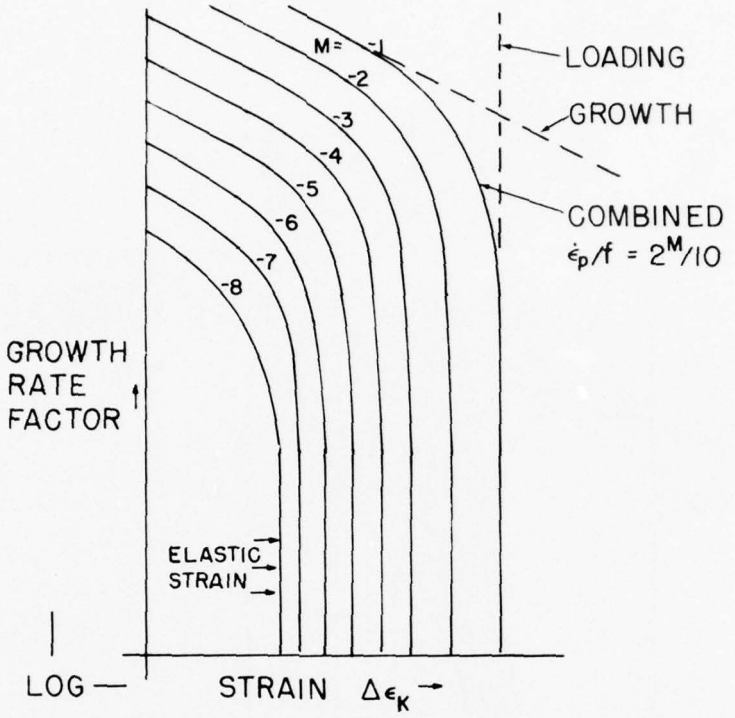

Fig. A-6 — Combined crack-tip strain rate

11. The next step is to map out a parametric family of curves of constant strain rate. This family, Fig. A6, is of the same geometric-series base (two) and (log) coordinates as the G(N) vs $\Delta\varepsilon_K$ map of Fig. A5. Two limiting conditions are observed. Strain due to a given amount of crack propagation increases as the K-level, hence gradient steepness, increases. Hence lines of constant strain rate due to propagation slope down -1 in G(N) /$\Delta\varepsilon_K$ space. However, the loading strain, independent of crack growth, is a function of ΔK alone. A base 2 family is a set of vertical lines an equal 2X apart on log paper. We use only the plastic part of the loading strain so that deducting the elastic strain compresses this set to the right. The combined loading and propagation strain rates joins these two extremes. In the text, indexing integers of the strain rate set are designated by M, those for the growth rate set by N.

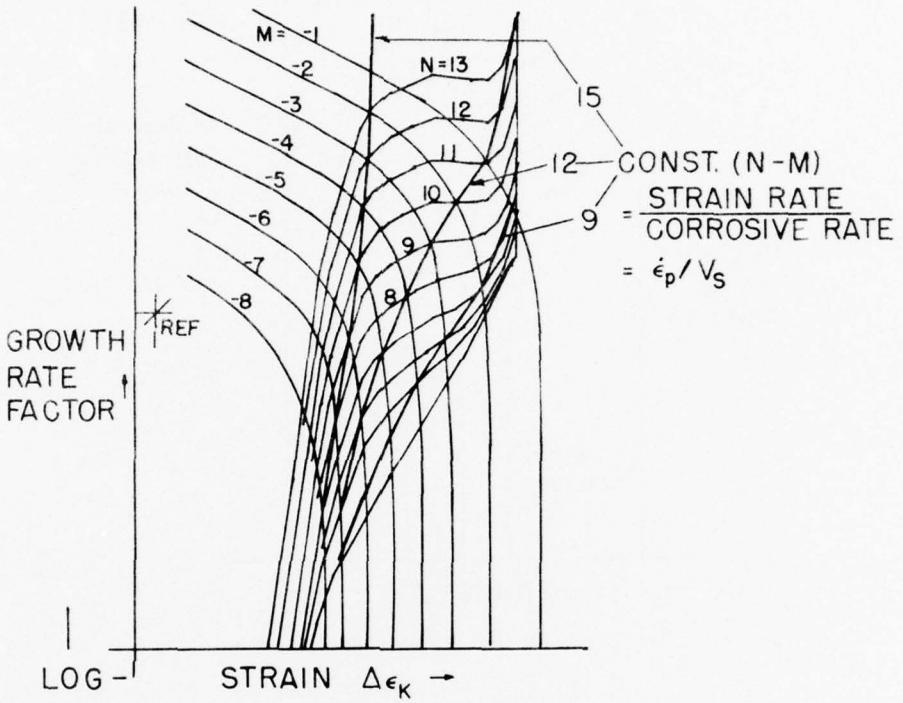

Fig. A-7 — Growth X strain rate mapping

12. The next step is to combine "M" and "N" maps, by simply superposing them as in Fig. A7. The loci of certain intersections of these now obtain a special significance. Traces of constant N-M (or M-N) indexes represent lines of constant ratio of total plastic strain to total surface attack during the loading cycle: $\Delta\varepsilon_p / \Delta r_T$. Relative to cycle duration these are rates - plastic strain vs surface attack rates: $\dot{\varepsilon}_p / V_S$.

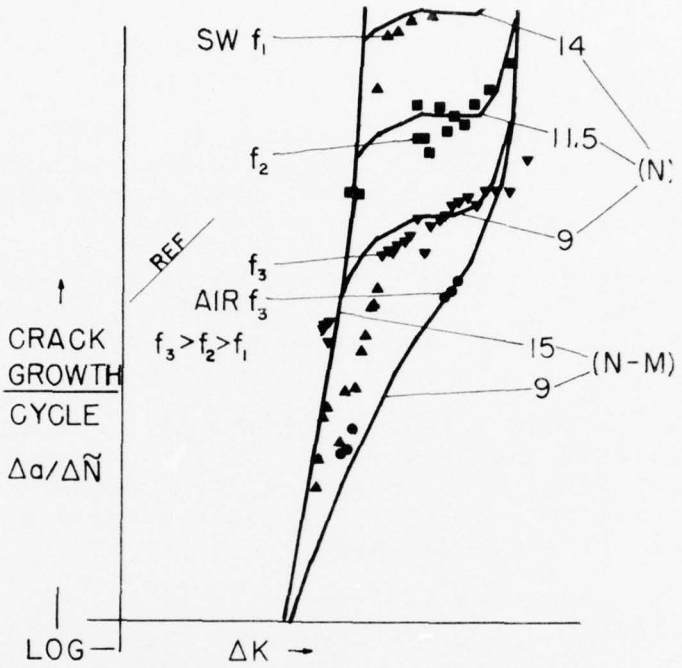

Fig. A-8 — Mapping crack growth data

13. The fit of the combined mapping of Fig. A7 to real CFCP data is done by selecting those factors of proportionality providing best fit of $G/\Delta\varepsilon_K$ to the $\frac{\Delta a}{\Delta N}/\Delta K$ data. This fit requires selecting one parameter- the microstructural size constant d_T. Since d_T affects both ordinate and abscissa scales, its selection constrains the fit to one degree of freedom: the reference point established on the growth X strain rate map, Fig. A7, must lie on the reference line of the crack growth data plot, Fig. A8. Once d_T is obtained, we observe that locus lines of constant N-M match the two frequency-independent growth rate limits of CFCP. The lower one in ΔK (upper in growth rate) appears to define the threshold of Stage II growth, the onset of the frequency-dependent plateau region on the $\frac{\Delta a}{\Delta N}$ vs ΔK plot, Fig. A8. Generally, a higher index N-M, means a lower critical value of relative strain rate ε_p/V_S, which corresponds to a lower and more steeply sloped ΔK line for stage II transition. When the stage II transition is unfavorable, i.e., of low ε_p/V_S, so generally is the upper ΔK limit which corresponds with the air environment growth profile.

14. To recapitulate, various anamolous behaviors of CFCP are fitted by use of three characterizing parameters, taken in conjunciton with tensile test data of each material. The parameters are:

a. The process zone size d_T, which locates in one degree of freedom, the map on the data. It is the crack tip distance within which the constant load condition is maintained.

b. The surface attack per cycle Δr_T, associated with the N index, for the growth rate curve of best fit to data of a given loading frequency. In susceptible alloys, the surface attack rate $\Delta r_T \cdot f = V_S$ is typically a constant, independent of frequency; and

c. The new parameter, the relative plastic strain (rate) $\Delta\varepsilon_p/\Delta r_T \approx \dot{\varepsilon}_p/V_S$ associated with the N-M index. Generally one value N-M pertains to stage II threshold, a lower one to the air environment growth rate.

14. The efficacy of this three-parameter characterization of CFCP is demonstrated by some dozen examples in the report. They include many of the known anomalous behaviors of CFCP. This success speaks of the opportunity to:

a. Analyse more cases of CFCP data with the improved model; and succeeding in this

b. Convert the method into simplified engineering rules and/or computer programs for safe-life prediction and damage tolerant design analysis.

AD-A043 368 NAVAL RESEARCH LAB WASHINGTON D C F/G 20/11
ORGANIZATIONAL SCHEME FOR CORROSION-FATIGUE CRACK PROPAGATION D--ETC(U)
JUL 77 J M KRAFFT, W H CULLEN

UNCLASSIFIED NRL-MR-3505 NL

2 OF 2
AD
A043 368

END
DATE
FILMED
9-77
DDC

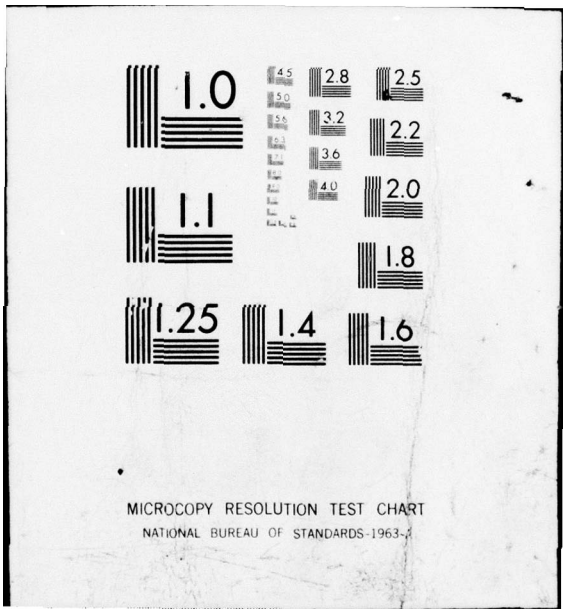
1.0
1.1
1.25
1.4
1.6
1.8
2.0
2.2
2.5
2.8
3.2
3.6
4.0
4.5
5.0
5.6
6.3
7.1
8.0
9.0
MICROCOPY RESOLUTION TEST CHART
NATIONAL BUREAU OF STANDARDS-1963-A

LIST OF ABBREVIATIONS, ACRONYMS AND SYMBOLS

K	- crack tip stress intensity factor, after Irwin
K_I	- mode I, plane strain stress intensity factor
ΔK	- stress intensity factor excursion
K_{Ic}	- K_I for onset of fast fracture instability or plane strain fracture toughness
K_{Iscc}	- K_I for threshold of SCC
FCP	- Fatigue Crack Propagation
CFCP	- Corrosion Fatigue Crack Propagation
SCC	- Stress Corrosion Cracking, sometimes called static-fatigue corrosion-induced crack growth
P	- load on a specimen
R	- load ratio, P_{min}/P_{max}, in fatigue
a	- crack length
$\dot{a}_N, \Delta a/\Delta N$	- increment in crack length in one cycle of fatigue loading
f	- frequency of fatigue loading
τ-Δt	- period of fatigue loading 1/f
t_L, t_H	- time intervals of loading and load-holding of a fatigue waveform
V	- Vacuum Environment
A	- Air
IA	- Inert Argon
FW	- Fresh Water
SW	- Salt Water (3.5% NaCl)
SEA	- Key West Ocean Water
σ, $\bar{\sigma}$, $\dot{\sigma}$	- stress, true stress, stress rate respectively
σ_{YS}	- yield strength at 0.2% offset
σ_{TUS}	- Ultimate Tensile Strength
σ_{CUS}	- Ultimate Compressive Strength
θ	- slope of stress-strain curve or tangent modulus
E	- Young's elastic modulus
ν	- Poisson ratio
m	- stress-relaxation exponent
ε, $\bar{\varepsilon}$, $\dot{\varepsilon}$	- strain, true strain, strain rate respectively
ε_d	- diametral strain
ε_ℓ	- longitudinal strain
ε_p	- plastic (only) strain
$\varepsilon_{1,2}$	- strain pertaining to first excursion (1), or full-cyclic equilibrium (2) strain cycle
S	- testing machine stiffness
C_T	- total compliance of a specimen-machine assemblage

σ_y, ε_y - stress, strain in direction normal to plane of mode I crack

r - distance ahead of crack or singularity point of crack-tip stress field

d_T - a specific value of r, found as a size parameter in the fracture-flow modelling

r_T - radius of a ligament of diameter d_T

Δr_T - radial diminution due to environmental surface attack or annihilation during the load cycle

V_S - rate of surface attack, $\Delta r_T/\tau$

A - cross-sectional area of d_T-ligament

∂A_ν - change in ligament cross-section due to Poisson contraction

∂A_s - change in ligament cross-section due to surface annihilation

$\partial \sigma_\theta$ - change in stress on ligament due to strain-hardening of ligament material

$\partial \sigma_m$ - change in stress on ligament due to stress relaxation of the ligament material

K_G - value of K associated with the strain gradient near the crack tip

K_L - value of K associated with load application in the fatigue cycle

ε_G - gradient strain, proportional to $\frac{d\varepsilon}{dr}$ at $r = d_T$, also proportional to K_G

ε_L - loading strain, at $r = d_T$, due to application of load in fatigue cycle, also proportional to K_L

ε_K or $\Delta\varepsilon_K$ - strain amplitude associated with maximum stress intensity factor or its excursion

$\Delta\bar{\varepsilon}_p = \dot{\bar{\varepsilon}}_p/f$ - plastic strain accruing in one loading cycle due to both crack loading and propagation

G_2 - growth rate factor associated with cyclic (2) stress strain curve

G_1 - growth rate factor associated with first excursion (1) stress strain curve

$G_{2/1}$ - growth rate factor proportional to the corrosion-augmentation of cyclic fatigue crack growth

$f_2(m)$ - coefficient of G_2

$f_1(\Delta r_T)$ - coefficient of G_1 or $G_{2/1}$

$G(N)$ - growth rate factor found by adding varying degrees of $G_{2/1}$ to G_2

Y - strain rate factor proportional to $G(N)$ used to display curves of constant plastic strain rate of the d_T ligament, $\dot{\bar{\varepsilon}}_p/f$

N - geometric series exponent for parametric curves of constant Δr_T in $G(N)$ vs $\Delta\varepsilon_K$ space

M - geometric series exponent for parametric curves of constant $\dot{\bar{\varepsilon}}_p/f$ in Y vs $\Delta\varepsilon_K$ space

CONVERSION FACTORS

1 MNm^{-2} = 1 MPa = 0.145 ksi

1 $MNm^{-3/2}$ = 1 MPa $\cdot$ $m^{1/2}$ = 0.91 ksi $\sqrt{in.}$

1 μm = 39.4 μ in.